

Orientation Dependence of Hardening and
Microstructural Evolution in Ion-irradiated
Tungsten Single Crystal

Eva HASENHUETL

Graduate School of Energy Science

Kyoto University

2017

Content

Chapter 1 – Introduction	5
1.1 Background	6
1.2 Tungsten (W) Application in ITER and DEMO	6
1.3 W Issues in general	7
1.4 References	9
Chapter 2 – Background and Research Status	10
2.1 Research Status concerning Crystal Orientation Dependence of Ion-irradiation Effects in W	11
2.1.1 Threshold Energy	11
2.1.2 Surface Morphology Changes	12
2.1.3 Type of Ion-irradiation Defects within the Material	15
2.1.4 Ion-irradiation Affected Zone within the Material	18
2.1.5 Hardening Behaviour	19
2.2 Research Status concerning Crystal Orientation Dependence of Mechanical Properties in Unirradiated W	20
2.2.1 Nanoindentation Hardness	20
2.2.2 Vickers Hardness	20
2.2.3 Tensile Stress-Strain Behaviour	22
2.3 Objectives	23
2.4 References	24
Chapter 3 – Experimental Methods	26
3.1 Material and Sample Preparation	27
3.1.1 Sample Cutting	27
3.1.2 Polishing of the Sample Surfaces	28
3.2 Ion-irradiation	28
3.3 Hardness Measurement by Nanoindentation Technique	29

3.4	Material Pile-up Height Measurement by Atomic Force Microscopy (AFM)	30
3.5	Microstructural Investigation by Transmission Electron Microscopy (TEM) Observation	30
3.6	References	31

Chapter 4 – Ion-irradiation Effect on Strain Rate Sensitivity of Nanoindentation

	Hardness of W Single Crystal	32
4.1	Introduction	33
4.2	Experimental Method	36
4.2.1	Material and Sample Preparation	36
4.2.2	Ion-irradiation	36
4.2.3.	Nanoindentation Tests	37
4.2.3.1	Standard CSR Test Method	38
4.2.3.2	SRJ Test Method	38
4.2.3.3.	Analytical Method	39
4.2.3.4	Bulk Equivalent LSR Sensitivity and Bulk Equivalent Activation Volume	40
4.3	Results and Discussions	41
4.3.1	Effect of Unloading/Loading in SRJ tests	41
4.3.2	Irradiation Effect on m Value	43
4.3.3	Irradiation Effect on V^*	46
4.3.4	SRS of Bulk Equivalent NI-hardness	47
4.4	Conclusions	50
4.5	Appendix	51
4.6	References	52

Chapter 5 – Evaluation of Ion-irradiation Hardening of Tungsten Single Crystals by

	Nanoindentation Technique Considering Material Pile-up Effect	56
5.1	Introduction	57
5.2	Experimental Method	59
5.2.1	Material and Sample Preparation	59

5.2.2	Ion-irradiation	59
5.2.3	Nanoindentation Tests	60
5.2.4	Pile-up Height Measurement	61
5.3	Analytical Method for Pile-up Corrected Hardness	61
5.3.1	Pile-up Corrected Hardness	61
5.3.2	Ion-irradiation Hardening Evaluation	66
5.4	Results and Discussions	67
5.5	Conclusions	74
5.6	Appendix	75
5.7	References	78
Chapter 6 – Orientation Dependence of Ion-irradiation Hardening in Pure Tungsten		
	Single Crystal	81
6.1	Introduction	82
6.2	Experimental Method	83
6.3	Results and Discussions	84
6.4	Conclusions	89
6.5	References	90
Chapter 7 – Orientation Dependence of Radiation Effect in Ion-irradiated W Single		
	Crystals up to Different Damage Levels	91
7.1	Introduction	92
7.2	Experimental Method	93
7.3	Results and Discussions	94
7.3.1	NI-hardness	94
7.3.1.1	Hardness Profiles	94
7.3.1.2	Bulk Equivalent Hardness	97
7.3.2	Microstructural Examinations	98
7.3.2.1	Lower Displacement Damage (0.1 dpa)	98
7.3.2.2	Higher Displacement Damage (2 dpa)	101
7.3.2.3	Summary of Damage Level Dependence of High Defect Density Zones	105

7.3.3	Orientation Dependence of High Defect Density Zones	106
7.4	Conclusions	106
7.5	References	108
	Chapter 8 – Summary	109
	Publication List	113

Chapter 1:

Introduction

1.1 Background

Electricity is the fastest growing type of end-use energy consumption worldwide ¹⁾. According to the U.S. Energy Information Administration ¹⁾, the world's net energy generation will increase by 69% from 21.6 trillion kWh in 2012 to 36.5 KWh in 2040, with the strongest growth in non-OECD countries, such as China and India ¹⁾. Coal made up 40% of total electricity generation in 2012 ¹⁾, but due to energy policy restrictions for CO₂ emission and/or sustainability issues of the energy source, the contribution of coal to the total electricity generation is expected to shrink in the future ¹⁾. Natural gas and renewable energy sources – 2/3 by hydropower and wind ¹⁾ – accounted each for 22% of the total generation ¹⁾ in 2012 and are expected to increase in the next decades ¹⁾. Electricity generation from nuclear power worldwide was 2.3 trillion in 2012 and it is expected to increase to 3.1 trillion kWh until 2020 ¹⁾. However, society's concerns about energy security have pushed back the activities of research & development of fission energy.

Fusion energy shows great safety advantages over fission energy supply regarding radioactivity concerns and sustainability features of deuterium in nature.

Currently, ITER (International Thermonuclear Experimental Reactor) project in southern France is the biggest ongoing research project. 35 nations - the European Union, Japan, China, India, Korea, Russia and the United States - are collaborating to check the feasibility of fusion as an electricity generation source ²⁾.

Still, neutron activity interactions, heavy thermal loading and hydrogen isotope and helium irradiation on the plasma facing components are among the important issues that have to be investigated to ensure a proper performance of future fusion power plants.

1.2 Tungsten (W) Application in ITER and DEMO

W has a

- ✓ High melting point, 3653 K ³⁾.
- ✓ High sputtering resistance to energetic particles ³⁾.
- ✓ High thermal conductivity $\approx 150 \text{ Wm}^{-1}\text{K}^{-1}$ at room temperature ⁴⁾.
- ✓ Low vapor pressure, $1.3 \times 10^{-7} \text{ Nm}^{-2}$ at the melting point ⁴⁾.

and is therefore chosen as the candidate material for plasma facing components in future fusion reactors, i.e. for first walls and diverter plates.

Figure 1.1 shows the current design version of the diverter in ITER and DEMO reactors using W plates for the plasma facing units ⁵⁾. The three main functions of the diverter will be heat exchange, helium trash extraction and fuel recycle ⁶⁾.

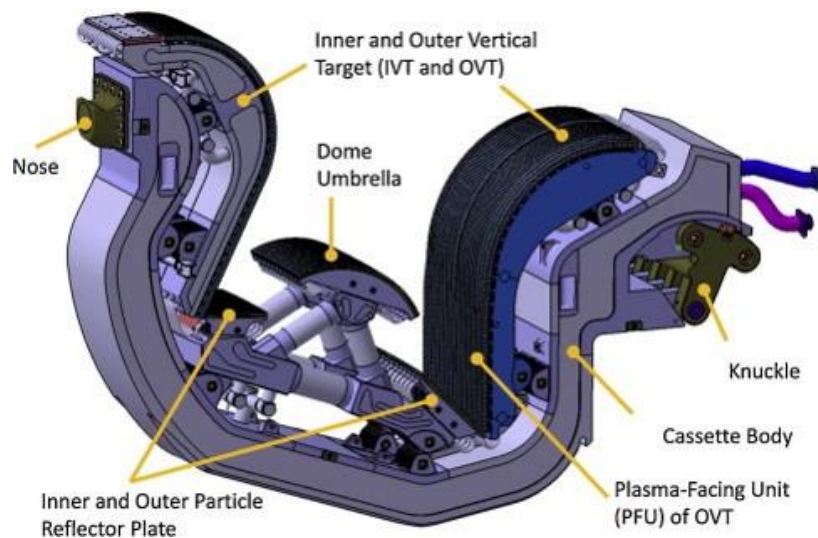


Figure 1.1: Detail of W diverter ⁵⁾.

W as diverter in ITER, see Figure 1.2, will be exposed to a yearly neutron damage level of 0.5 dpa ^{7,8)}, while in DEMO it is 20 dpa ^{7,8)}.

1.3 W Issues in general

Radiation embrittlement is a main concern for W application in fusion power plants, because the burned deuterium and tritium will react to neutrons and helium, where the high energy neutron irradiation will cause displacement damages and the production of transmutation elements (rhenium, osmium, tantalum) and the high energy helium will cause helium implantation in W. All these processes will further on increase the initial brittle

behaviour of W. Since embrittlement is related to hardening, basic study is needed on the irradiation hardening in W. Ion irradiation experiment are an accurate alternative to neutron irradiation experiment to simulate fusion environment in a safe and fast way.

This thesis here copes with the ion-irradiation effects on pure W. As for the exposure to ion-irradiation in W as plasma facing material, defects will be generated that result from the displacement of atoms at different crystal orientations. However, the existing studies on ion-irradiation effects on W mainly focus on polycrystalline W neglecting grain orientation dependence on the results⁹⁻¹³).

1.4 References

- 1) International Energy Outlook 2016, U.S. Energy Information Administration, Office of Energy Analysis, Washington, DC, USA (2016).
[http://www.eia.gov/outlooks/ieo/pdf/0484\(2016\).pdf](http://www.eia.gov/outlooks/ieo/pdf/0484(2016).pdf) (Accessed online on 2017.01.06).
- 2) <https://www.iter.org/proj/inafewlines> ((Accessed online on 2017.02.24).
- 3) A. Hasegawa, M. Fukuda, S. Nagomi and K. Yabuuchi: *Fus. Eng. Des.* **89** (2014) 1568-1572.
- 4) V. Philipps: *J. Nucl. Mater.* **415** (2011) S2-S9.
- 5) T. Hirai, F. Escourbiac, S. Carpentier-Chouchan, A. Fedosov, L. Ferrand, T. Jokinen, V. Komarov, A. Kukushkin, M. Merola, R. Mitteau, R.A. Pitts, W. Shu, M. Sugihara, B. Riccardi, S. Suzuki and R. Villari: *Fus. Eng. Des.* **88** (2013) 1798–1801.
- 6) Z.X. Zhang, Ion-irradiation Hardening and Microstructure Evolution in Tungsten, Dissertation, Graduate School of Energy Science, Kyoto University (2016).
- 7) A.F. Rowcliffe. Tungsten-based materials for divertor applications (Oak Ridge National Laboratory)
http://web.ornl.gov/sci/physical_sciences_directorate/mst/fusionreactor/pdf/Vol.48/5.1_p76-95_Rowcliffe.pdf ((Accessed online on 2017.02.24).
- 8) D.G. Whyte, B. Lipschultz, First Wall Issues: ITER to DEMO, Greenwald Panel, FESAC Meeting, August 8 2007.
- 9) Z.X. Zhang, E. Hasenhuettl, K. Yabuuchi and A. Kimura: *Nucl. Mater. En.* **9** (2016) 539-546.
- 10) D. Armstrong, A. Wilkinson and S.G. Roberts: *Physica Scripta* **2011 (T145)** (2011) 014076.
- 11) D.E.J. Armstrong, P.D. Edmondson and S.G. Roberts: *Applied Physics Letters* **102** (25) (2013).
- 12) D.E.J. Armstrong, X. Yi, E.A. Marquis and S.G. Roberts: *J. Nucl. Mater.* **432** (1-3) (2013) 428-436.
- 13) J.S.K.L. Gibson, S.G. Roberts and D.E.J. Armstrong: *Mater Sci Eng A Struct Mater* **625** (2015) 380-384.

Chapter 2:
Background and Research Status

2.1 Research Status concerning Crystal Orientation Dependence of Ion-irradiation Effects

2.1.1 Threshold Energy

Owing to the crystal structure of W, the displacement threshold energy E_d of W depends on the direction of ion beam to crystal orientation, and various authors ¹⁻³⁾ reported that the minimum E_d is along $\langle 100 \rangle$ orientation.

Maury et al. ¹⁾ carried out 1.4–1.8 MeV electron irradiation on W single crystal and reported that the E_d was minimum in the crystal with the irradiation planes of (100) and (111), where the E_d are 42 eV for the $\langle 100 \rangle$ direction and 44 eV for the $\langle 111 \rangle$ direction. Stuart et al. ²⁾ reported that it is 65.6 eV along $\langle 100 \rangle$ and 100 eV along $\langle 110 \rangle$ orientation. More recently, Xu et al. ³⁾ carried out MD simulation and reported that the E_d along the $\langle 100 \rangle$ direction was 68 eV, which again was found as the orientation with the minimum E_d , as can be seen in Figure 2.1.

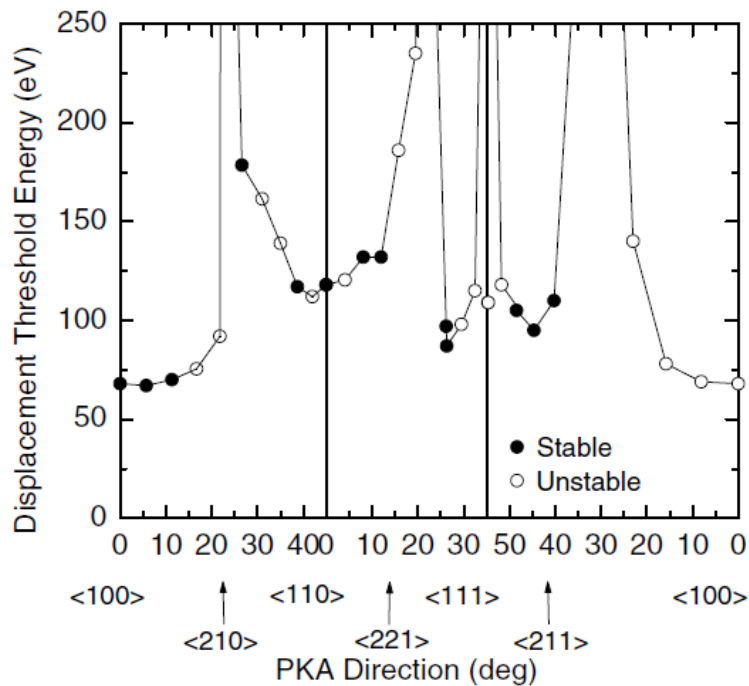


Figure 2.1: E_d as a function of PKA (primary knock atom) direction from Xu et al. ³⁾.

Finally, ASTM standards ⁴⁾ recommend to use an averaged threshold energy of 90eV for calculating damage distributions in W.

2.1.2 Surface Morphology Changes

The differences in surface morphology changes caused by helium plasma irradiation (initial surface temperature 1800 K and maximum helium fluence $7.2 \times 10^{26} \text{ He}^+/\text{m}^2$) between W single crystals of (100) and (110) surface orientations were reported by Kajita et al. ⁵⁾, when the helium fluence was less than 10^{25} m^{-2} ⁵⁾. On the (100) surface, the surface was flatter and protrusions from the bursting of the helium bubbles were formed, whereas the (110) surface showed a rough wavy like structure ⁵⁾, see Figure 2.2. Beyond the fluence of $10^{25} \text{ He}^+/\text{m}^2$, nanostructures grew in both orientations ⁵⁾.

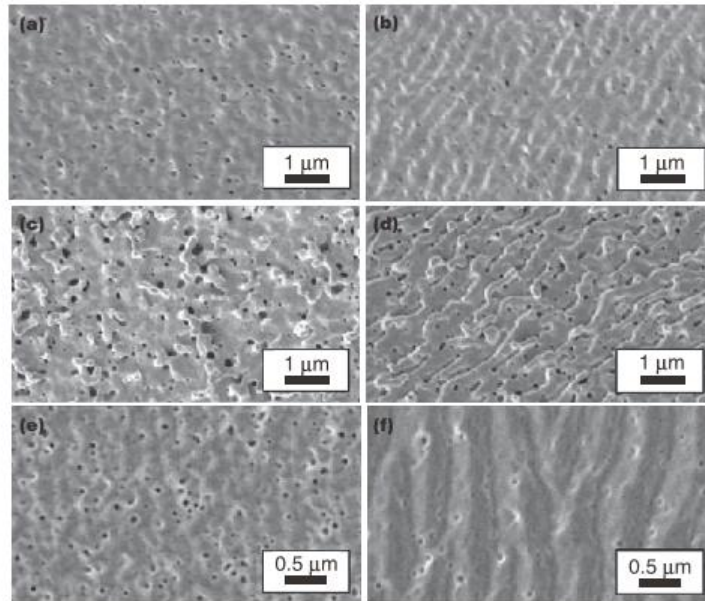


Figure 2.2: SEM micrograph of helium irradiated single crystals by Kajita et al. ⁵⁾. (a), (c), (e) account for W(100) and (b), (d), (f) account for W(110). Irradiation condition of (a), (b): 55eV, 1800 K, fluence $0.6 \times 10^{25} \text{ He}^+/\text{m}^2$; (c), (d): 55eV, 1800 K, $1.8 \times 10^{25} \text{ He}^+/\text{m}^2$; (e), (f): 27eV, 1600 K, $1.5 \times 10^{25} \text{ He}^+/\text{m}^2$.

Low flux helium (50keV , $3.55 \times 10^{18} \text{He}^+/\text{cm}^2$) and hydrogen (35keV , $3.4 \times 10^{19} \text{H}^+/\text{cm}^2$) ion-irradiation on polycrystalline W by Liu et al. ⁶⁾ were carried out to investigate the blistering behavior in grains of different orientations. The blister density was reported the highest on the grain near (111) plane and the smallest near (001) plane. It was also reported that the blistering resistant surface orientation in W was near the (001) plane, as shown in Figure 2.3.

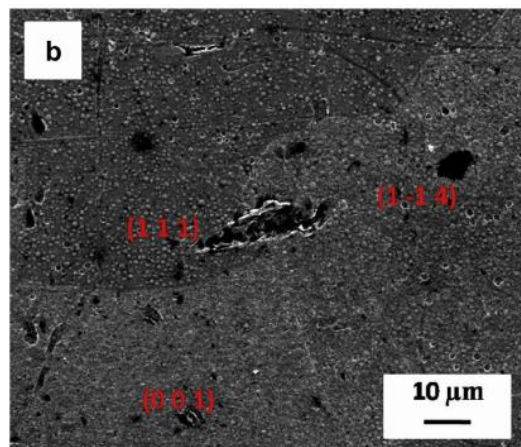


Figure 2.3: Surface morphology changes in W grains close to (111), (001) and (1-14) by Liu et al. ⁶⁾.

In situ SEM and EBSD investigations, see Figure 2.4, of microstructure evolution during Focused Ion Beam (FIB) bombardment of Ga^+ ions (30keV Ga^+ beam) on polycrystalline W surface showed that grains with (001) surface maintained a much smoother surface morphology with less mass removal than the other ⁷⁾, as seen in Figure 2.5. Ran et al. ⁷⁾ attributed this to a relatively high binding energy of surface atoms in (001) and the potential channeling effect in such low index orientation of (001) ⁷⁾.

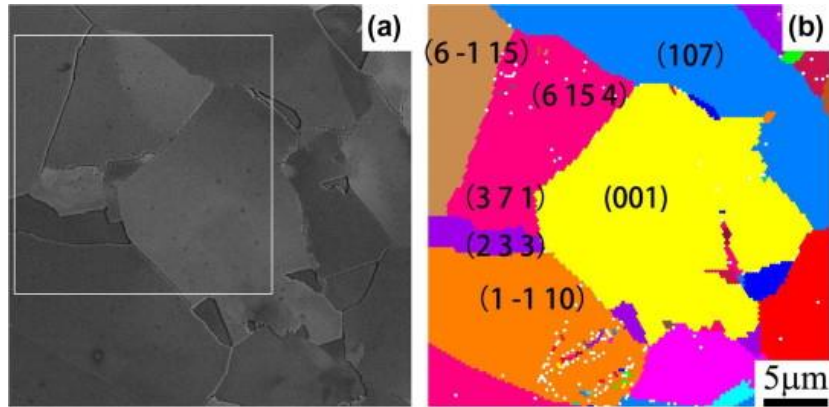


Figure 2.4: (a) SEM image of an electrochemically polished polycrystalline W surface. (b) EBSD orientation map of shortcut area in (a), by Ran et al. ⁷⁾.

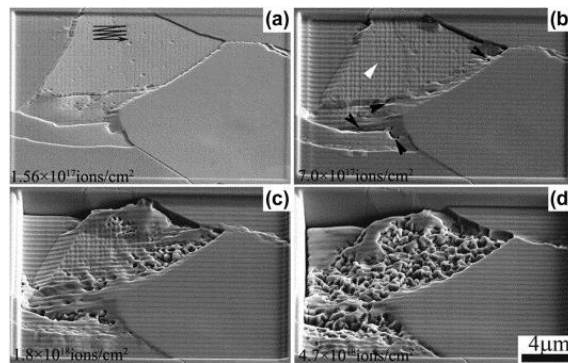


Figure 2.5: In situ SEM observation of polycrystalline W surface shown in Figure 2.6 during Ga⁺ bombardment, by Ran et al. ⁷⁾ (surface shown with 52° tilt).

High heat flux (10.5 MW/m²) irradiation of helium neutral beams (33keV, flux 2×10²¹m⁻²s⁻¹) on rolled W exposing an initial pulse (4.6s) resulting in a partial molting, and then several helium pulses with fluences of 1.2–2.5×10²²/m² at temperatures from 1450 to 2590 °C showed that the molten surface morphology is correlated with the crystal orientation of the resolidified grains ⁸⁾. Figure 2.6 shows the surface morphology of the molten W surface after several helium pulses at 1730°C and helium fluence of 1.4×10²²/m² ⁸⁾. The blistering on the grains were classified to “light” close to (001) plane, “medium” close to (011) plane and “heavy” close to (111) plane. Image (d) in Figure 2.8 shows the FIB cross section of the red line in image (b),

where the thickness of the damaged surface was reported to be 0.18 μm and the blister skin itself of 0.11 μm .

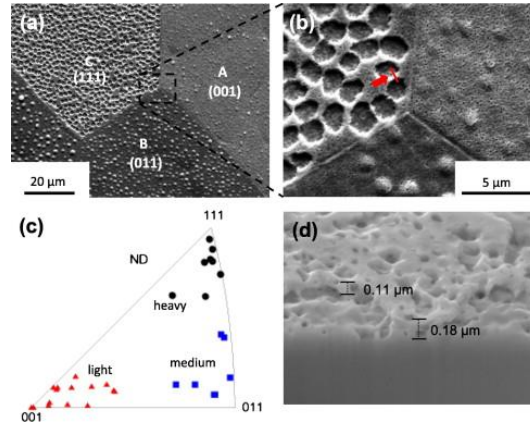


Figure 2.6: Surface morphology of molten tungsten surface after several helium pulses at 1730 °C and helium fluence of $1.4 \times 10^{22}/\text{m}^2$ by Yuan et al. ⁸⁾.

2.1.3 Type of Ion-irradiation Defects within the Material

Systematic TEM studies of self-ion irradiated (2 MeV W^+ ions; 573 K to 1023 K up; 0.4 dpa to 30 dpa and 150 keV W^+ ; 30 K to 1073 K; 0.01 dpa and 1 dpa) pure W, W-5wt.% Re and W-5wt.%Ta alloys by Yi et al. ⁹⁻¹⁰⁾ showed that the dislocation loops interact with each other at a given irradiation temperature and damage level depending on the grain orientation with respect to the ion beam direction. Figure 2.7 and Figure 2.8 shows the microstructure after 1 dpa and 0.4 dpa/1.2 dpa, resp., for irradiated W-5Ta alloy at 773 K and 573 K, resp., in grains of [001], [011] and [111] orientations. Figure 2.9 shows images during *in-situ* TEM study of loop string and loop network formation in [011] oriented grain of a W-5V alloy, which is irradiated at 1073 K. Loop strings were formed at this temperature after 0.4 dpa irradiation in [011] oriented W-5V grain.

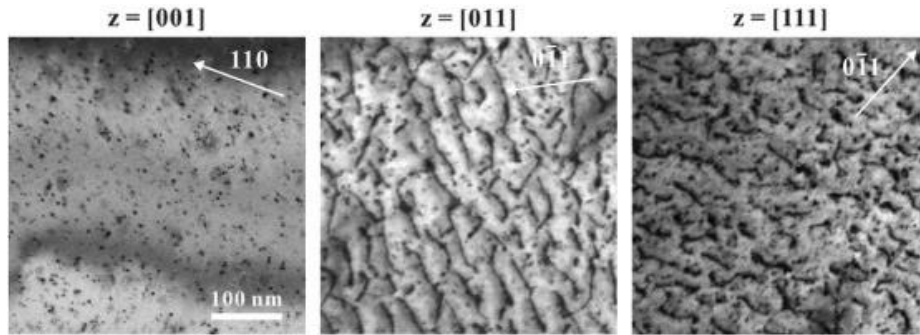


Figure 2.7: Damage microstructures of W-5Ta irradiated at 773 K to 1.0 dpa are compared in [001], [011] and [111] oriented grains by Yi et al. ¹⁰.

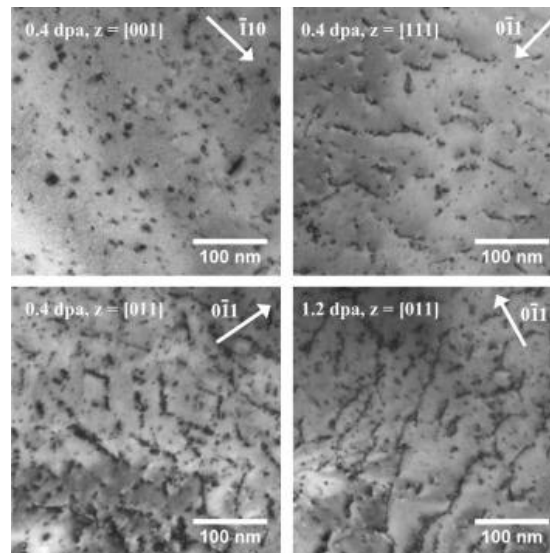


Figure 2.8: Comparison of damage microstructures in W-5Ta, irradiated at 300 °C in $z = [0\ 0\ 1]$, $[0\ 1\ 1]$ and $[1\ 1\ 1]$ orientations by Yi et al. ⁹.

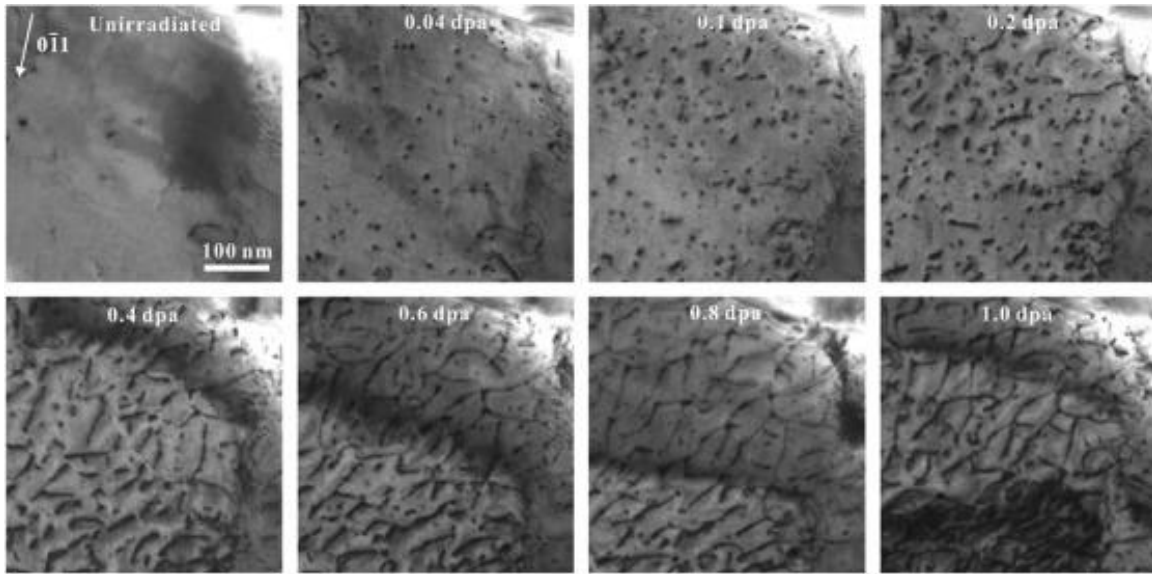


Figure 2.9: In situ TEM study of loop string and network formation in $[011]$ oriented grain of a W-5V alloy, irradiated at 1073 K by Yi et al. ¹⁰⁾.

Yi et al. ⁹⁻¹⁰⁾ reported that for non- $\langle 001 \rangle$ grains, the temperature and damage level necessary to form dislocation strings or rafts is smaller than in $\langle 001 \rangle$ grains. The reason for this phenomenon is that in non $\langle 001 \rangle$ grains, the loops with different Burgers vector variants are lost to the surface with different probabilities and therefore more loops would be retained in the material as in $\langle 001 \rangle$ grains that show equal probabilities ⁹⁻¹⁰⁾, hence the presence of a nearby free surface would favor the formation of loop strings in non- $\langle 001 \rangle$ grains ⁹⁻¹⁰⁾. Therefore Yi et al. ⁹⁻¹⁰⁾ suggested that the TEM investigation of ion-irradiated $\langle 001 \rangle$ grains would be more representative to correlate with neutron irradiated W study considering equivalent dose and temperature.

Figure 2.10 shows the microstructure after self-ion irradiation with different temperature and damage level of a $\langle 001 \rangle$ oriented grain in pure W ⁹⁾. The authors reported ⁹⁾ that loop strings in $\langle 001 \rangle$ were starting to form at 773 K at 1.2 dpa, and with increasing the damage level, the structure became more inhomogeneous. With further increase of damage level, they reported larger loops size and smaller loop number density with the effect being very small so that their conclusion was that the saturation would be around 1.2 dpa ⁹⁾.

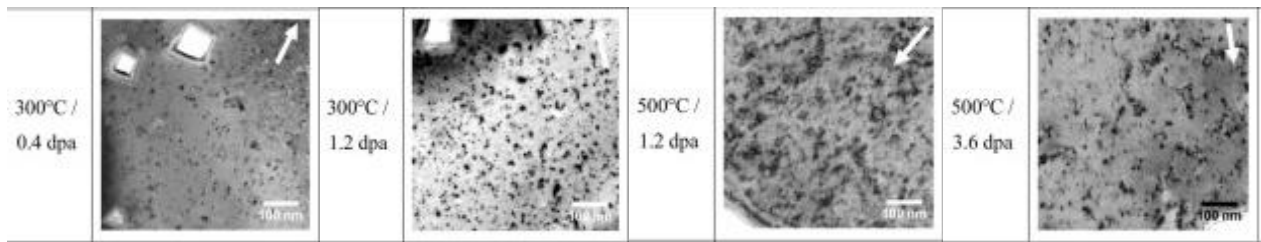


Figure 2.10: Microstructure of $\langle 001 \rangle$ oriented grain in pure W at 573 K and 773 K with increasing damage level by Yi et al. ⁹⁾ (The photo images are picked up and rearranged from the original figure shown in the paper reference ⁹⁾).

2.1.4 Ion-irradiation Affected Zone Size within the Material

Self ion (W^{6+}) irradiation (20 MeV, up to 2.3 dpa and 6.36 dpa at room temperature) on polycrystalline W was carried out by Grzonka et al. ¹¹⁾. TEM observation of the 2.3 dpa sample showed that the irradiation affected damaged depth inside a [110] grain was deeper compared to the adjacent [012] grain. But the difference in damage depth found was very small and they found no orientation dependence in adjacent grains after irradiation up to 6.36 dpa, as can be seen in Figure 2.11. In their opinion ¹¹⁾, channeling and/or the interaction of dislocation with grain boundaries within the area of damage zone could be the reason for the difference in the detected damage depth.

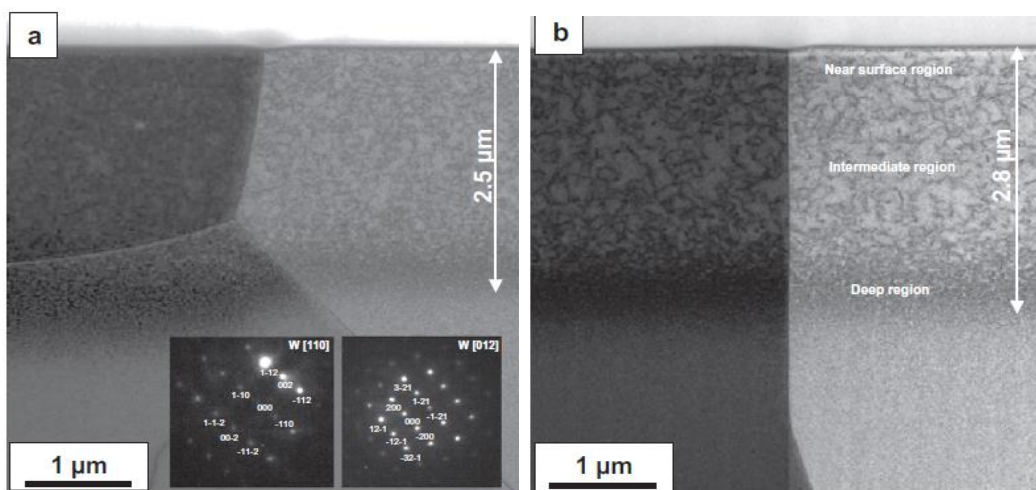


Figure 2.11: Ion-irradiation affected zone in pure polycrystalline W, self-ion irradiated at room temperature up to (a) 2.3 and (b) 6.36 dpa, respectively, by Grzonka et al. ¹¹⁾.

In polycrystalline pure W irradiated (dual ion beam: 6.4 MeV Fe³⁺ and 1 MeV He⁺) up to 2 dpa at temperatures 573 K, 773 K, 973 K and 1273 K by Zhang et al. ¹²⁾, it was found that the ion-irradiation affected zone increased with increasing temperature from 2200 nm, 2300 nm, 2500 nm to 3500 nm depth, respectively, and it was concluded that the reason was due to diffusion of the interstitial atoms and its clusters. The microstructural overview is given in Figure 2.12 ¹²⁾.

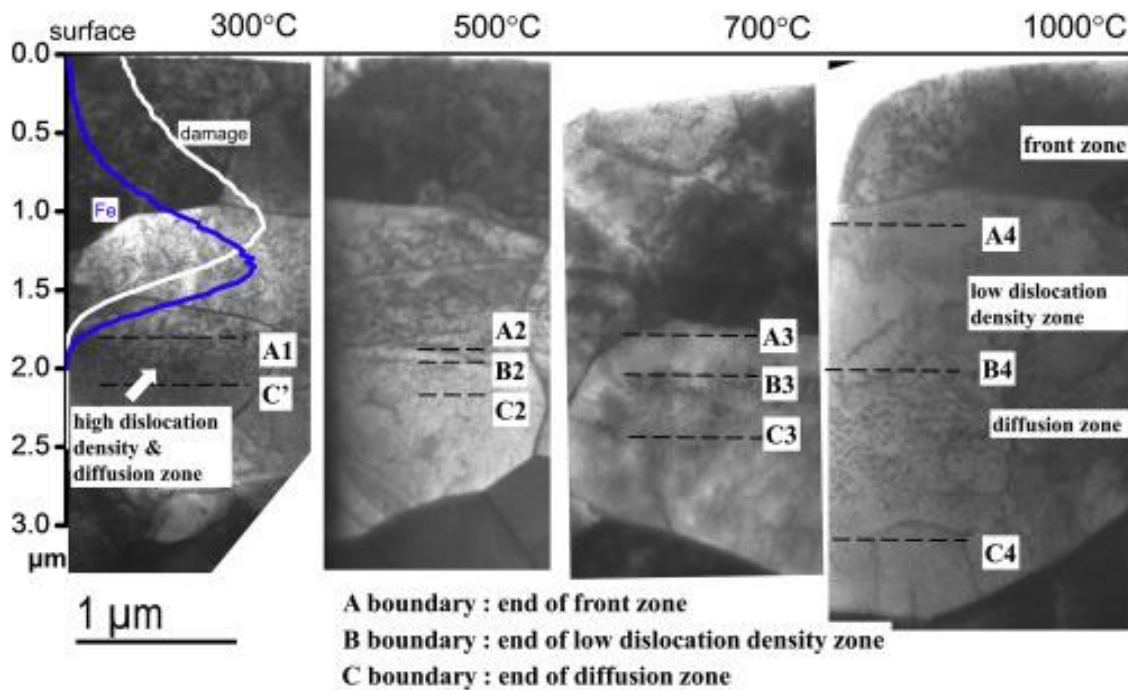


Figure 2.12: Microstructural overview of 2 dpa ion-irradiation damaged layer for different irradiation temperatures in polycrystalline W, by Zhang et al. ¹²⁾.

Zhang et al. ¹²⁾ reported that the position of the defect zones slightly changed in different grains, which they considered be due to channelling effects or focusing effect during irradiation ¹³⁾. However, the overall distribution of each zone was following one trend ¹²⁾.

2.1.5 Hardening Behaviour

Nanoindentation hardness results of deuterium implanted (115 eV, fluence 6×10^{24} D/m² at 373 K) W single crystals of (001), (011) and (111) surface orientation showed no crystal

orientation dependence and no visible effect of irradiation on the hardness as well ¹⁴⁾, as given in Table 2.1 by Yao et al. ^{14,15)}. But based on a statistical analyses, the pop-in load, which is often believed to be the transition load from elastic to plastic state, was found to be crystal orientation dependent with the highest load in (001) W, followed by (110) W and the lowest in (111) W in all the material conditions, as-polished, annealed and D-implanted ^{14,15)}.

Surface orientation	As-polished (GPa)	Annealed (GPa)	D-implanted (GPa)
(100)	4.46 ± 0.22	4.49 ± 0.14	4.44 ± 0.15
(110)	4.41 ± 0.15	4.43 ± 0.12	4.38 ± 0.12
(111)	4.44 ± 0.09	4.47 ± 0.11	4.42 ± 0.21

Table 2.1: Nanoindentation hardness of unirradiated and D-implanted W single crystals of different surface orientations, by Yao et al. ¹⁴⁾.

2.2 Research Status concerning Crystal Orientation Dependence of Mechanical Properties in unirradiated W

2.2.1 Nanoindentation Hardness

As shown above in session 2.1.5, Yao et al. ¹⁴⁾ reported nanoindentation hardness for unirradiated W(100), W(110) and W(111) and mentioned no orientation dependence. However, only a single value was given by the author instead of an entire hardness-depth profile.

2.2.2 Vickers Hardness

Microindentation study using a Vickers indenter on (100), (110) and (111) W single crystals were performed by Stelmashenko et al. ¹⁶⁾. As Figure 2.13 shows, the measured hardness in each orientation depends on the applied load or alternatively on the measured diagonal imprint length. Increasing load decreases the microindentation hardness in all orientations, but in a different way. For small loads (or diagonal lengths of imprint), (100) surface shows the highest hardness, followed by (110) and the smallest hardness is obtained

from the (111) orientation. Above a certain load, there seem to be a turnover in the ranking of hardness between (100), (110) and (111). W(100) then shows the lowest and W(111) shows the highest hardness, with W(110) within these extremes. As shown in Figure 2.13, Stelmashenko et al. ¹⁶⁾ further studied the azimuthal position of the indenter with respect to the local crystal orientation, and concluded that there were differences in the hardness for different azimuthal orientations, possibly due to the different initiated stress distribution below the indent ¹⁶⁾. The authors ¹⁶⁾ also measured the material pile-ups around the Vickers indents and reported that the maximum pile-ups reached 17-20% of indentation depth in W(100), 6-8% in W(110) and 5-7% in W(111), but not critically depended on the azimuthal orientation of the indent. This suggests that the formation of pile-up is mainly driven by the local crystal orientation and not by the stress distribution below the indents ¹⁶⁾. Generally, they concluded that W(100) was the hardest surface among the three investigated surfaces, and that the harder a surface is the higher its trend to pile-up formation will be instead of the trend to increase the plastic field below the indent.

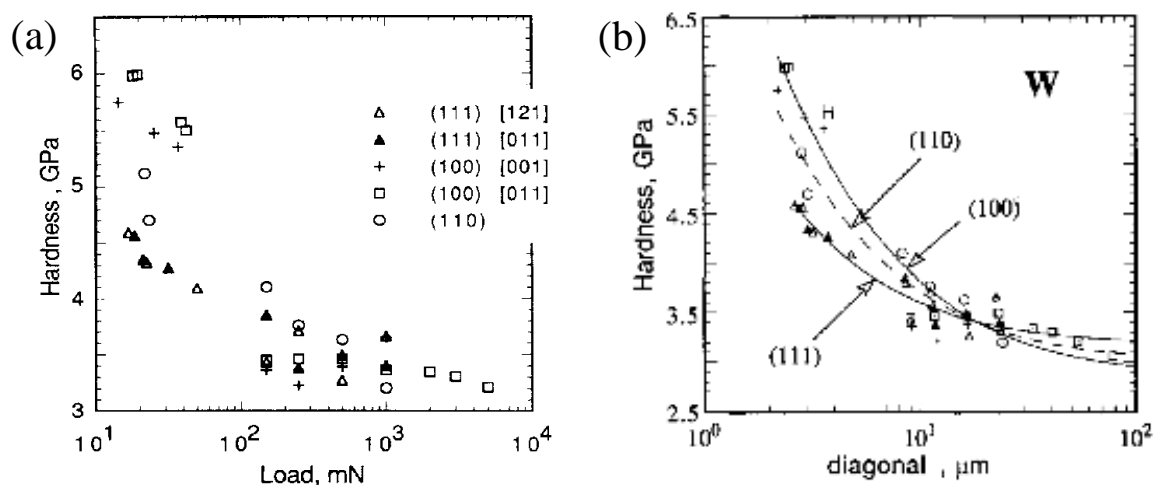


Figure 2.13: Obtained hardness as a function of (a) applied load and (b) measured diagonal imprint length, by Stelmashenko et al. ¹⁶⁾.

2.2.3 Tensile Stress-Strain Behaviour

Tensile tests by Argon et al. ¹⁷⁾ on W single crystals of low index orientations showed that the stress–strain behaviour varies significantly with crystal orientations, see Figure 2.14. [110] showed the highest yield stress, followed by [111] and the smallest in [100].

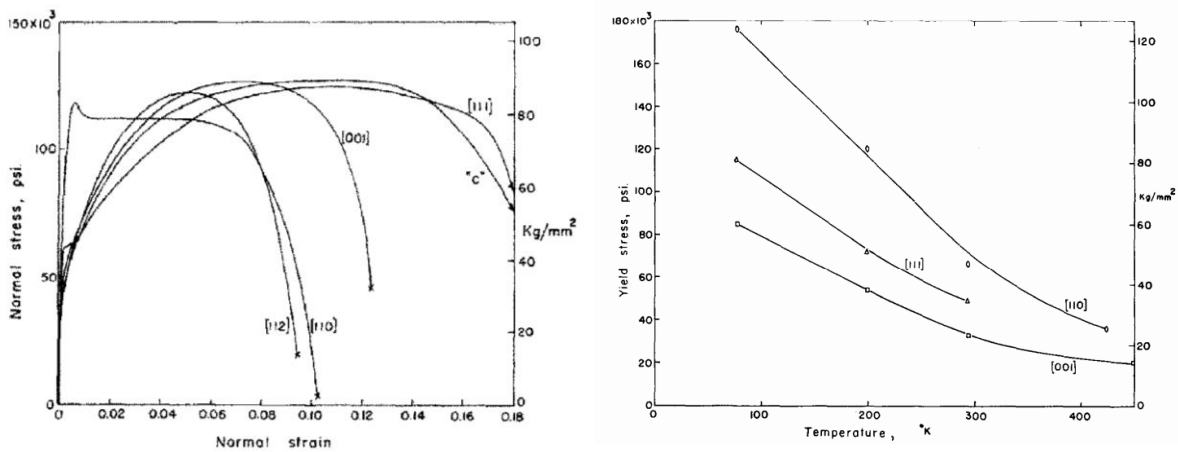


Figure 2.14: Tensile stress-strain behaviour of W single crystals with different crystal orientations, by Argon et al. ¹⁷⁾.

Beardmore et al. ¹⁸⁾ also investigated the tensile properties of W [110], [111] and [100] single crystals for temperatures between 77 K and 295 K and discussed about general crystal orientation dependent work hardening stages that appear within these temperature ranges, as schematically shown in the following Figure 2.15. According to the authors ¹⁸⁾, work hardening stage 1, θ_1 , is related to the process that determines the proportional limit ¹⁸⁾ and work hardening stage 2, θ_2 , is related qualitatively to the number of operative slip vectors ¹⁸⁾. The results of Beardmore et al. ¹⁸⁾ have been summarized in the following Table 2.2.

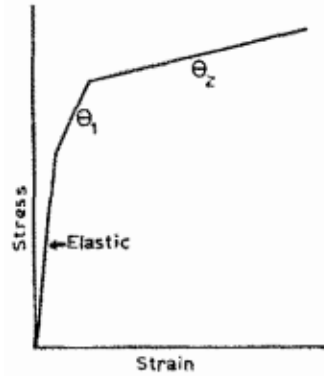


Figure 2.15: Schematic diagram of work hardening stages in the stress-strain curves of W(100), W(11) and W(111), by Beardmore et al. ¹⁸⁾.

Summary of tensile test results on W(100), W(110) and W(111):
$\sigma_y (110) > \sigma_y (111) > \sigma_y (100)$
$\theta_1 (110) > \theta_1 (100) > \theta_1 (111)$
$\theta_2 (100) (4 \text{ slip vectors equally favored}) > \theta_2 (111) (3 \text{ slip vectors}) > \theta_2 (110) (2 \text{ slip vectors})$

Table 2.2: Summary of tensile results for W(100), W(110) and W(111) of Beardmore et al. ¹⁸⁾.

2.3 Objectives

As shown in this chapter, the important questions about crystal orientation dependence of ion-irradiation hardening and ion-irradiation affected zone size are still unresolved.

The objective of this thesis is to investigate the potential effect of crystal orientation on hardening and microstructure evolution in ion-irradiated W without the consideration of grain boundary effects. As a fundamental study, W single crystals of (001) and (011) surface orientations were used and irradiated with 6.4MeV Fe³⁺ ions at 573 K up to 0.1, 1 and 2 dpa, in order to also investigate damage level dependence of ion-irradiation effect in pure W.

2.4 References

- 1) F. Maury, M. Biget, P. Vajda, A. Lucasson and P. Lucasson: Rad. Eff. **38** (1978) 53.
- 2) R.N. Stuart, M.W. Guinan and R.J. Borg: Rad. Eff. **30** (1976) 129-133.
- 3) Q. Xu, T. Yoshiie and H. Huang: Nucl. Instrum. Methods Phys. Res. B **206** (2003) 123-126.
- 4) Standard Practice for Neutron Radiation Damage Simulation by Charge-Particle Irradiation, E521-96, Annual Book of ASTM Standards, **Vol. 12.02**, American Society for Testing and Materials, Philadelphia, 1996, p. 1
- 5) S. Kajita, N. Yoshida, N. Ohno, Y. Hirahata and R. Yoshihara: Phys. Scripta **89** (2) (2014).
- 6) F. Liu, H. Ren, S. Peng and K. Zhu: Nucl. Instrum. Methods Phys. Res. B **333** (2014) 120-123.
- 7) G. Ran, S.Wu, X. Liu, J. Wu, N. Li, X. Zu and L. Wang: Nucl. Instrum. Methods Phys. Res. B **289** (2012) 39-42.
- 8) Y. Yuan, H. Greuner, B. Böswirth, C. Linsmeier, G.N. Luo, B.Q. Fu, H.Y Xu, Z.J. Shen and W. Liu: J. Nucl. Mater. **437** (2013) 297-302.
- 9) X. Yi, M.L. Jenkins, K. Hattar, P.D. Edmondson and S.G. Roberts: Acta Mater. **92** (2015) 163-177.
- 10) X. Yi, M.L. Jenkins, M.A. Kirk, Z. Zhou and S.G. Roberts: Acta Mater. **112** (2016) 105-120.
- 11) J. Grzonka, L. Ciupinski, J. Smalc-Koziorowska, O.V. Ogorodnikova, M. Mayer and K.J. Kurzydowski: Nucl. Instrum. Methods Phys. Res. B **340** (2014) 27-33.
- 12) Z.X. Zhang, K. Yabuuchi and A. Kimura: J. Nucl. Mater. **480** (2016) 207-215.
- 13) G.S. Was, *Fundamentals of Radiation Materials Science: Metals and Alloys*, Springer Science & Business Media (2007)
- 14) W.Z. Yao, P. Wang, A. Manhard, C.E. Krill, III and J.H. You: Mater. Sci. Eng. A **559** (2013) 467-473.
- 15) Y. W, *Crystal Plasticity Study of Single Crystal Tungsten by Indentation Tests*, Dissertation, Faculty of Engineering and Informatics, Ulm University (2012).
- 16) N. Stelmashenko, M. Walls, L. Brown and Y.V. Milman: Acta Metall. et Mater. **41** (10) (1993) 2855-2865.
- 17) A. Argon and S. Maloof: Acta Metall. **14** (11) (1966) 1449-1462.

18) P. Beardmore and D. Hull: *J. Less Common Met.* **9** (1965) 168-180.

Chapter 3:

Experimental Methods

3.1 Material and Sample Preparation

3.1.1 Sample Cutting

The initial material used in this study was a W single crystal with (001) surface orientation. As illustrated in Figure 3.1, EBSD (Electron Backscattered Diffraction Pattern) method using a FE-SEM (Ultra55) facility was used to get $\langle 011 \rangle$ type orientations. The pole figures served the information, along which angle θ the sample has to be cut with the respect to a reference line so that the new cut surface would be of (011). The surface orientation of the new sample was then again confirmed by EBSD method to be (011) and the inverse pole figures of both type of specimens W(001) and W(011) are shown in Figure 3.2. The specimens are denoted as W{001} and W{011} hereinafter.

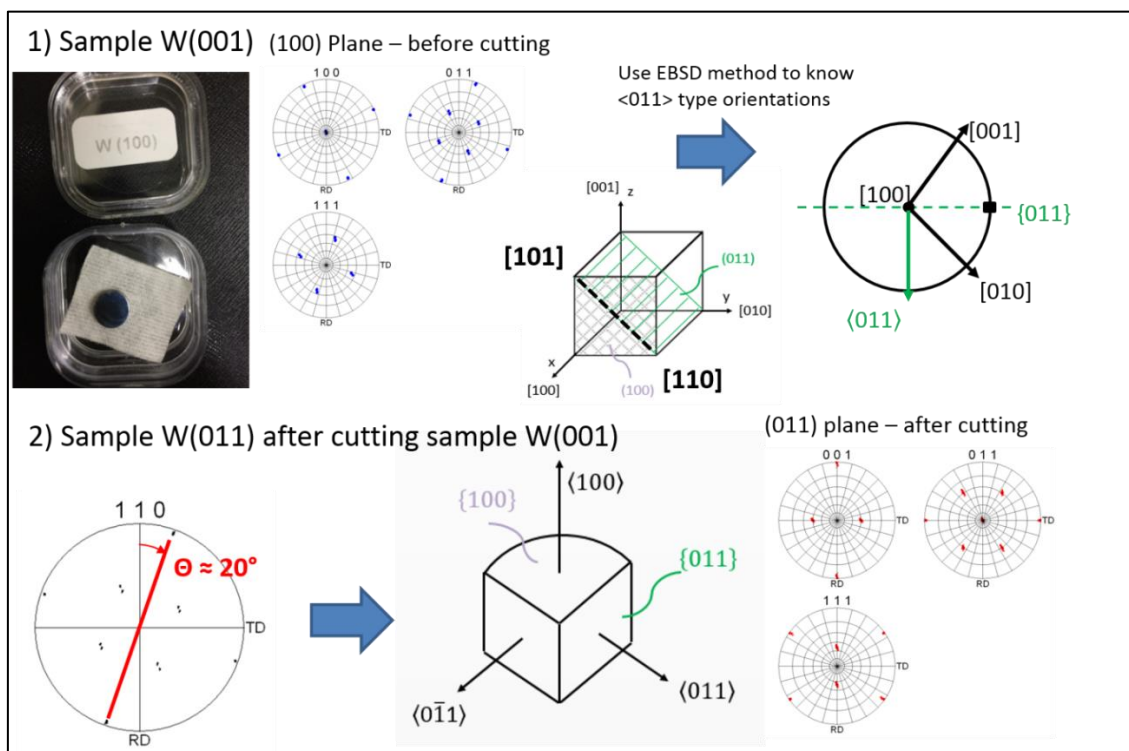


Figure 3.1: Schematic overview of the cutting procedure of W(011) specimens from initial W(001) specimens.

In total, four sample of each surface orientation W{001} and W{011} were used in this study.

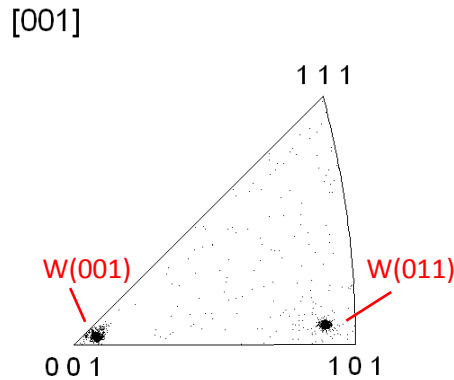


Figure 3.2: Combined inverse pole figures of $W\{001\}$ and $W\{011\}$ specimens.

3.1.2 Polishing of the Sample Surfaces

After cutting, all eight samples, four of each surface orientation, underwent mechanical polishing procedures to remove hardened and oxidized layers on the surface. The specimens were fixed with an acrylic bonder to a glass holder stage and then the samples were manually polished on SiC papers starting with roughness #800 (~5min), then #1200 (~20min), then #2000 (~20min) and finally #4000 (~30min). In each step, the holder with the specimen was polished along two directions that were 90° apart and abrasive paper to next finer step has been changed after all scratches have been removed in this step. After finishing with #4000 sand paper, the surfaces were polished with diamond paste of which the particle size was $0.25\ \mu\text{m}$. Finally, electrochemical polishing (20 V, 5 min., 1%NaOH solution) was performed on all samples.

3.2 Ion-irradiation

Ion-irradiation was performed at DuET, Kyoto University Japan, see Figure 3.3.



Figure 3.3: DuET dual-beam ion-irradiation facility, Kyoto University.

Single beam 6.4 MeV Fe³⁺ ions were used as ion source. The irradiation conditions used in this study are given in Table 3.1 below:

	Temperature [K]	Fe ³⁺ fluence [ions/m ²]	Fe ³⁺ flux [ions/m ² /s]	Nominal damage level [dpa]*
W{001}	573	4.81x10 ¹⁹	1.1x10 ¹⁶	2
	573	2.52x10 ¹⁹	1.05x10 ¹⁶	1
	573	2.53x10 ¹⁸	1.06 x10 ¹⁶	0.1
W{011}	573	4.81x10 ¹⁹	1.1x10 ¹⁶	2
	573	2.52x10 ¹⁹	1.05x10 ¹⁶	1
	573	2.53x10 ¹⁸	1.06 x10 ¹⁶	0.1

*Table 3.1: Summary of irradiation conditions used in this study. *The nominal damage levels were rounded to one decimal place.*

For all damage levels, the simulated target ranges of damage and Fe³⁺ distribution in W by SRIM code software ¹⁾ are given and described in the manuscripts in chapter 4, 5, 6 and 7 of this thesis.

3.3 Hardness Measurement by Nanoindentation Technique

Ion-irradiation causes a thin and inhomogeneous hardened layer within a few microns to the exposed material, which makes nanoindentation technique necessary in order to evaluate the hardness behavior after ion-irradiation. In this study a nanoindenter from Agilent Technologies Inc. Model NanoIndenter G200 with a Berkovich tip was used to characterize the hardness of W{001} and W{011} before and after ion-irradiation to 0.1, 1 and 2 dpa. Different operations methods of the machine – Basic hardness method ²⁾, Constant Strain Rate (CSR) method using Continuously Stiffness Method (CSM) ³⁾ as well as Strain Rate Jump (SRJ) method ^{4,5)} – have been used for different material property characterizations that are described in detail in the manuscripts in chapter 4, 5, 6 and 7 of this thesis.

3.4 Material Pile-up Height Measurement by Atomic Force Microscopy (AFM)

AFM facility of Keysight Technology Inc. has been used to measure maximum material pile-up heights that form on W surface around the remained indents after nanoindentation testing. The method and the results are described in detail in Chapter 5 of this thesis.

3.5 Microstructural Investigation by Transmission Electron Microscopy (TEM) Observation

Microstructure in ion-irradiated W{001} and W{011} of 0.1, 1 and 2 dpa has been characterized by TEM study. The necessary thin foils for TEM observations have been cut from the bulk samples by a Focused Ion Beam (FIB) facility (HITACHI FB2200). Finally, surface of the thin foils of around 240-270 nm thickness have been electrochemically polished (4-6ms in 0.45%NaOH aqueous solution at 20 V at 276-277 K) to remove the damage caused by FIB processes. As can be seen in the TEM images in this thesis, the chosen electro-chemical condition is regarded so successful to remove the damage caused by FIB manufacturing process that defects caused by actual ion-irradiation can be evaluated. Successful electro-chemical condition is also expected by the fact that the amorphous W layer, which should protect the irradiation surface from FIB damage, is preserved. Thus, the irradiation surface can be clearly identified, which is an important subject in this thesis, to discuss about ion-irradiation affected zone size, see chapter 7.

3.6 References

- 1) "INTERACTION OF IONS WITH MATTER" by J.F. Ziegler. <http://www.srim.org/>, (accessed 2016-09-17).
- 2) ISO 14577-1: 2002 Metallic Materials- Instrumented Indentation Test for Hardness and Materials Parameters - Part 1: Test method.
- 3) W. C. Oliver and G. M. Pharr: J. Mater. Res. **7** (1992) 1564-1583.
- 4) V. Maier, K. Durst, J. Mueller, B. Backes, H. W. Höppel, H. W. and M. Göken: J. Mater. Res. **26** (2011) 1421-1430.
- 5) V. Maier, C. Schunk, M. Göken and K. Durst: Phil. Mag. **95** (2015) 1766-1779.

Chapter 4:
**Ion-irradiation Effect on Strain Rate Sensitivity
of Nanoindentation Hardness of W Single
Crystal**

4.1 Introduction

Tungsten (W) is the promising material for plasma facing components in ITER and DEMO fusion reactors¹⁻⁴). During operation, W will be exposed to neutron irradiation which will cause irradiation hardening and embrittlement⁴⁻⁸). Off-normal plasma operation caused by plasma disruption and edge localized mode (ELM)⁹) would degrade the mechanical properties of W suffering so called recrystallization embrittlement through the high heat loading, and the rapid change in thermal stress/strain may cause cracking. Since the strain rate sensitivity (SRS) is large in bcc W, the effect of irradiation on SRS is an important issue to understand material response to off-normal plasma operation that may induce irradiation embrittlement accompanied by hardening. Furthermore, the assessment of the SRS before and after irradiation offers one the important information about the characteristics of irradiation-induced obstacles to dislocation motion.

Fukumoto et al.¹⁰) performed tensile tests of neutron (563K, 0.003 dpa to 0.064 dpa) irradiated vanadium alloys, V-4Cr-4Ti-0.1Si, and the results of tensile testing at room temperature (RT) showed that the SRS was lower and higher in the specimen irradiated to 0.008 dpa and 0.064 dpa, respectively¹⁰). The early works of tensile tests of Wronski et al.¹¹) on neutron (2×10^{22} n/m²; $E_n > 1$ MeV) irradiated molybdenum (Mo) showed that irradiation caused a mitigation of strain rate dependence of yield stress. They interpreted this in terms of an irradiation-induced increase in the effective activation volume for yielding¹¹). Tanaka et al.¹²) conducted tensile tests (223K to 525K; 2.8×10^{-6} s⁻¹ to 2.8×10^{-2} s⁻¹) for neutron irradiated Mo (6.3×10^{21} n/m² to 5×10^{23} n/m²; $E_n > 1$ MeV) and showed that the irradiation decreased the SRS of yield stress, which became more pronounced with increasing neutron fluence. They concluded that the athermal component of the yield stress was increased by neutron irradiation and this trend was more pronounced with increasing neutron fluence¹²). The tensile test results (223K – 373K, 10^{-5} s⁻¹ to 10^{-2} s⁻¹) of Li et al.¹³) of neutron irradiated Mo (~353K, 7.2×10^{-5} dpa

to 0.28 dpa) showed that generally, irradiation mitigated strain rate dependence of the yield stress in comparison to unirradiated Mo. With increasing the damage level, the strain rate dependence of the yield stress was mitigated up to about 0.003dpa. Beyond this damage level, the strain rate dependence of the yield stress was kept nearly constant¹³⁾. No effect on the strain rate dependence of the plastic instability stress was observed¹³⁾. Post-irradiation isochronal annealing (annealing temperature from 300 K to around 850 K; deformation temperature at 290 K) experiments by Aono et al.¹⁴⁾ for neutron irradiated ($T < 363$ K; 1.1×10^{21} n/m² and 1×10^{22} n/m²) high-purity iron single crystals revealed that the change in the SRS depended on the isochronal annealing temperature: the annealing between 300 K and 500 K caused an increase in SRS of yield stress, while between 500 K and 800 K, it led to a decrease in SRS, and above 800 K the SRS seemed to show no change compared to unirradiated condition¹⁴⁾.

S.M. Ohr et al.¹⁵⁾ carried out strain rate change tests and stress relaxation tests (RT, 6.56×10^{-5} s⁻¹ and 6.56×10^{-4} s⁻¹) on unirradiated and neutron (1.2×10^{20} n/m²; $E_n > 1$ MeV) irradiated Ferrovac-E iron and concluded that the irradiation caused no change in activation volume suggesting that irradiation did not induce further short range obstacles to dislocation motion. They also reported an irradiation-induced increase in the athermal stress or long range internal stress by approximately 33 MPa, which accounted for nearly all the increase in the yield stress at RT due to irradiation¹⁵⁾. They further on reported that the effective stress was also increased by irradiation when tested at low temperatures¹⁵⁾. McRickard et al.¹⁶⁾ carried out stress relaxation tests at a low strain rate (< 0.01 s⁻¹) for neutron irradiated (2×10^{22} n/m²; $E_n > 1$ MeV) Ferrovac iron, and came to the same trend with them for activation volume and athermal stress. Early works^{17, 18)} on neutron (539K; 0.5, 4, and 6.5×10^{23} n/m²; $E_n > 1$ MeV) irradiated ASTM A533-B steel showed that for all the testing temperatures, increasing fluence led to an increase in yield stress and to a decrease in strain rate sensitivity.

As for W, early works of Steichen ¹⁹⁾ reported tensile property changes after neutron irradiation (0.5×10^{26} n/m² at 644K and 0.9×10^{26} n/m² at 655K) over a wide range of tensile test temperatures and strain rates (295K to 1200K, 3×10^{-4} s⁻¹ to 1 s⁻¹), summarized by a rate-temperature parameter ²⁰⁾ and set in relation with the yield stress ²⁰⁾. Under these conditions, W showed a pronounced strain rate and temperature dependence. However, no individual strain rate sensitivity values were assessed by the author ¹⁹⁾ for neutron irradiated W.

There is no research on ion-irradiation effects on the strain rate sensitivity of W, although ion irradiation experiments have been considered to be convenient to study radiation effects on materials. Since several MeV of ion-irradiation causes a damaged layer within the range of a few microns, nanoindentation (NI) hardness test method is applied to evaluate the ion-irradiation hardening. In NI, a well-recognized deduction of SRS of NI-hardness is defined ²¹⁾ in analogy to the SRS exponent formulation for uniaxial tensile and compression tests ²²⁾. Maier et al. ²³⁾ conducted a strain rate jump (SRJ) test of NI-hardness to assess the localized strain rate (LSR) sensitivity, where a SRS parameter m was derived by conducting several SRJ set-ups at different indentation depths. It is noticed that SRS is now represented by LSR sensitivity in NI-hardness tests since the deformation area is limited just beneath the indenter. The original method ²³⁾ has been developed for nanocrystalline and ultrafine-grained materials exhibiting no indentation size effect (ISE) ²⁴⁾, which is a phenomenon that NI hardness decreases with indentation depth, but attempts have been made to apply the method to single crystal materials ²⁵⁾ exhibiting strong ISE ²⁴⁾ in order to evaluate the influence of the ISE ²⁴⁾ on the LSR sensitivity measurements ²⁵⁾. The SRJ method was recently applied to ion-irradiated single crystal of Fe-15Cr-20Ni austenitic steel, which had an fcc structure, by Kasada et al. ²⁶⁾. Their results showed that ion-irradiation slightly decreased SRS of NI-hardness and the SRS parameters were similar with those obtained by Sun et al. ²⁷⁾ by means of SRJ tensile test method on ultra-fine grained and coarse grained austenitic Fe-14Cr-16Ni alloy tested at 293K ²⁷⁾.

LSR sensitivity of ion-irradiated bcc metal, which generally had rather higher SRS than fcc metals, is worth to be studied. Furthermore, it is considered that the feasibility check of the validity of SRS measurement by NI-hardness technique for the ion-irradiated materials is necessary for the assessment of correlation potential between ion- and neutron-irradiation effects. Thus, the objective here is to investigate the effect of ion-irradiation on the LSR sensitivity of NI-hardness of W single crystal for understanding characteristics of ion-irradiation induced defects as obstacles to the dislocation motion in W.

4.2 Experimental Method

4.2.1 Material and Sample Preparation

The material used was a pure (99.97 wt%) W single crystal with {001} surface orientation which allowed one to evaluate the SRS without considering the effect of grain boundaries. The exact surface orientation of the specimen was measured by electron back scatter diffraction patterns (EBSD) method. Four W{001} specimens were mechanically polished by SiC abrasive papers. Then the surfaces were polished with diamond paste of which the particle size was 0.25 μm . Finally, electrochemical polishing (20 V, 5 min., 1%NaOH solution) was carried out to remove the deformation layer induced by mechanical polishing.

4.2.2 Ion-irradiation

Three W{001} specimens were irradiated with 6.4 MeV Fe^{3+} ions at 573 K to nominal displacement damages of 0.1, 1 and 2 dpa using a tandetron accelerator in Kyoto University²⁸⁾. The target depth profile of the displacement damage and ion distribution was calculated using the SRIM (the stopping and range of ions in matter) package²⁹⁾ and is given in Figure 4.1, where the nominal dpa is defined as the displacement damage at the depth of 600 nm. The

average threshold energy is chosen as 90 eV according to ASTM standards³⁰⁾ for the SRIM²⁹⁾ calculation.

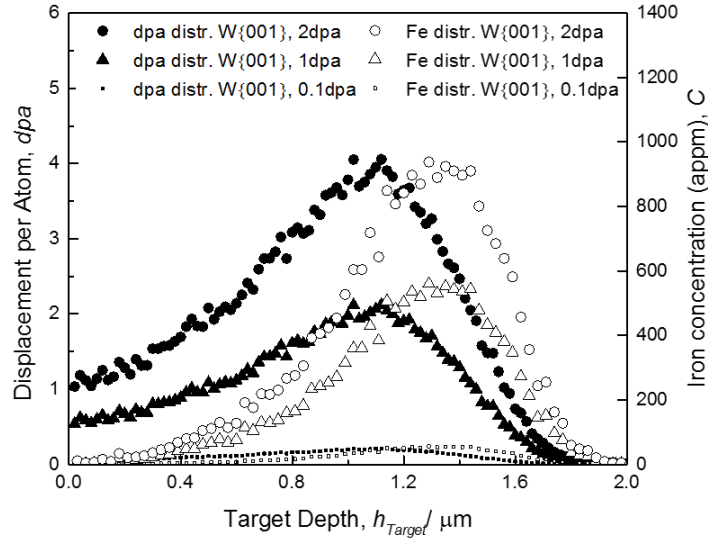


Figure 4.1: The target depth profile of the displacement damage and ion distribution calculated using the SRIM package²⁹⁾ (0.1 dpa, 1 dpa and 2 dpa W{001}).

4.2.3. Nanoindentation Tests

Nanoindentation tests on the unirradiated and ion-irradiated specimens were performed using a NanoIndenter G200 of Agilent Technologies Inc., operated with a Berkovich diamond tip. The azimuthal orientation of the indenter has been set randomly with respect to the local crystal orientation, as Yao³¹⁾ experimentally and numerically pointed out for W single crystals of {001}, {011} and {111} surface orientation, that the azimuthal orientation of the indenter has a negligible effect on the load–displacement curves. Several definitions of the term “strain rate” exist in NI test. According to Lucas et al.³²⁾, indentation strain rate $\dot{\epsilon}$ can be estimated by the equation (4.1) considering the NI-hardness rate $\dot{H} \approx 0$, consequently it is in good approximation to a half of the loading-rate \dot{P} divided by the load P , \dot{P}/P :

$$\dot{\epsilon} = \dot{h}/h = (\dot{P}/P - \dot{H}/H)/2 \approx (\dot{P}/P)/2 \quad (4.1)$$

where \dot{h}/h is the ratio of the indenter displacement velocity \dot{h} and the contact depth h ²¹⁾ and \dot{H}/H is the ratio of NI-hardness increasing rate \dot{H} divided by the NI-hardness H . A directly proportional relationship between \dot{h}/h and \dot{P}/P was also shown by Cheng et al.³³⁾. Since in NI-hardness test, the strain rate is of a very localized area, it is called local strain rate (LSR) hereinafter for the term \dot{P}/P , because in standard constant strain rate (CSR) test method³²⁾ as well as SRJ test method, the ratio \dot{P}/P is stable while the indentation strain rate $\dot{\epsilon}$ that is obtained from \dot{h}/h is rather unstable. In both testing methods, a continuously stiffness measurement (CSM) condition³⁴⁾ was superimposed to the loading path and set to a frequency 45 Hz and an oscillation amplitude 1 nm. The testing temperatures were 299 ± 2 K.

4.2.3.1 Standard CSR Test Method

Standard CSR tests were performed at two different LSR of 0.3 s^{-1} and 0.01 s^{-1} . The LSR sensitivity was estimated from the NI-hardness values at the several depths similar to those of SRJ tests, ranging from 300 to 900 nm as shown in Figure 4.4, by performing two indentation tests at two different LSR up to the maximum indentation depth of 2000 nm. At each LSR, 16 tests were carried out, whereas the 10 test results giving the smallest error bar were used for the analysis. Averaged NI-hardness at each LSR was used to estimate the LSR sensitivity.

4.2.3.2 SRJ Test Method

The SRJ method^{23, 25)} has been applied to obtain LSR sensitivity of NI-hardness at various indentation depths. The indentation depths for initial unloading have been chosen at 8 different indentation depths up to 800 nm. The experimental set-ups are summarized in Table 4.1. Each of these 8 SRJ test set-ups consisted of 4 - 5 testing points and the tests were carried

out with two different combinations of LSR changes: 0.3 s^{-1} and 0.01 s^{-1} or 0.03 s^{-1} and 0.001 s^{-1} .

Set-up	1	2	3	4	5	6	7	8	9	10	11	12	13	14	15	16
0.3-0.01 [s^{-1}]	T	T	T	T	T	T	T	T								
0.03-0.001 [s^{-1}]									T	T	T	T	T	T	T	T
h unload [nm]	250	300	350	450	550	600	650	800	250	300	350	450	550	600	650	800
h load [nm]	350	400	450	550	650	700	750	900	350	400	450	550	650	700	750	900

Table 4.1: The set-ups of SRJ test method, varying in depth of initial unloading and LSR. The difference of indentation depth between unloading and loading jump per set-up was kept constant over all set-ups to 100nm.

4.2.3.3. Analytical Method

The indentation strain rate change, $d\dot{\epsilon}$, at a certain indentation depth causes the change in the NI-hardness dH , giving the LSR sensitivity, m , of NI-hardness at the indentation depth h ^{21, 36}.

$$m = d(\ln H)/d(\ln \dot{\epsilon}) \quad (4.2)$$

Obtaining LSR sensitivity by CSR tests with equation (4.2) requires the results of two independent tests at different $\dot{\epsilon}$ or \dot{P}/P . In the following work, the results and the term LSR are referred to the ratio \dot{P}/P not to $\dot{\epsilon}$, keeping in mind the proportional relationship between them ^{32, 33}). The advantages of this method will be visible in Figure 4.2 later on.

An activation volume V^* ³⁷⁻⁴¹) accounting for the thermally activated deformation mechanism can be assessed as reported in the other works ^{25, 42-45}) from the indentation strain rate change in logarithmic expression $d(\ln \dot{\epsilon})$ and corresponding NI-hardness change dH at a certain indentation depth h ,

$$V^* = 3\sqrt{3}kT(d(\ln \dot{\epsilon}))/dH \quad (4.3)$$

where k is the Boltzmann constant and T the absolute temperature. The factors 3 and $\sqrt{3}$ stand for the constraint factor between hardness and flow stress and for the factor between flow stress and shear stress, respectively.

4.2.3.4 Bulk Equivalent LSR Sensitivity and Bulk Equivalent Activation Volume

Nix and Gao ²⁴⁾ interpreted ISE based on the concept of geometrically necessary dislocation, and they defined a bulk equivalent hardness as the H at $h = \infty$, which indicated that the H was equal to H_0 at infinite depth, in the following equation:

$$H/H_0 = (1 + (h^*/h))^{1/2} \quad (4.4)$$

where H is the NI-hardness at a certain indentation depth h , H_0 is the hardness at the infinite depth and h^* is the so-called characteristic length, which depends on the shape of the indenter, the shear modulus and H_0 ²⁴⁾. In the original work of Nix and Gao ²⁴⁾, h^* is the slope of the H/H_0 versus $1/h$ plot. To obtain the bulk equivalent LSR sensitivity of NI-hardness of the ion-irradiated W{001}, the extended method of Nix and Gao ²⁴⁾ by Kasada et al. ⁴⁶⁾ considering SSE ³⁵⁾ was applied here, where the bulk equivalent NI-hardness of ion irradiated region, $H_{irr\ bulkequ.}$, can be obtained by the least square fitting of the NI-hardness data up to the so called critical indentation depth, h_c ⁴⁶⁾, which is denoted as the indentation depth, below which the underlying substrate has a minor effect on the hardness of the thin film ³⁵⁾. H_0 and $H_{irr\ bulkequ.}$ were obtained for the LSR change, 0.3 s^{-1} - 0.01 s^{-1} by SRJ tests and CSR tests.

The bulk equivalent activation volume has been calculated according to equation (3). In this case, dH stands for the change of the bulk equivalent NI-hardness between two LSR.

4.3 Results and Discussions

4.3.1 Effect of Unloading/Loading in SRJ tests

Figure 4.2 shows an example of unloading and loading SRJ test for unirradiated W{001}, where the NI-hardness changes with the change in the indentation strain rate, $\dot{\epsilon} = \dot{h}/h$, and $LSR = \dot{P}/P$ over the indentation depth. At a reduction of LSR and consequently a reduction of $\dot{\epsilon}$, a transient decrease in NI-hardness, namely relevant unloading, was observed until the NI-hardness reached to the level corresponding to the lower LSR. Generally, compared to LSR, the $\dot{\epsilon}$ fluctuated and delayed in reaching its target values, see the red and blue line in the upper image of Figure 4.2. Moreover, $\dot{\epsilon}$ values were not always in agreement with equation (4.1) in the shallow indentation depth. The upper image of Figure 4.2 shows that $\dot{\epsilon}$ was around 2/3 of LSR, highlighted by the red and blue digits for the upper and lower $\dot{\epsilon}$. However, because the ratio was constant for all tested LSR as well as in theory, the LSR was used as a measure of strain rate as mentioned before. The LSR sensitivity was obtained by both the unloading and loading jump tests for comparison. Note that a set-up of unloading and loading needs about 100 nm of indentation depth, consequently, in this study, two set-ups of each unloading and loading jump were conducted at the same indentation depth to directly compare the results for the same indentation depth, as shown in the bottom of Figure 4.2. The delay in reaching the target indentation strain rate $\dot{\epsilon}$ is much smaller for the loading jump compared to the unloading jump, as can be seen in the both images in Figure 4.2.

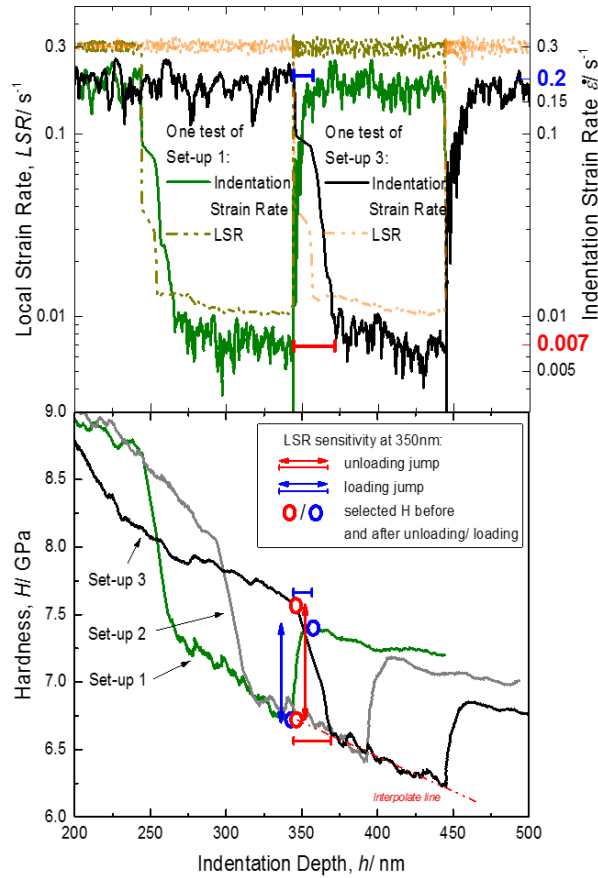


Figure 4.2: SRJ test method (unloading and loading): Correlation between LSR- and indentation strain rate jumps and NI-hardness evolution. Methods to calculate LSR sensitivity by Maier et al. (red lines) and Kasada et al. (blue lines)

Maier et al. ²⁵⁾ evaluated the LSR sensitivity by performing the unloading jump tests with taking account of the indentation depth difference caused by the delay in reaching the target $\dot{\epsilon}$, where the NI-hardness after unloading jump was the interpolated value at the same depth with before unloading, as shown by red lines in the bottom of Figure 4.2. The LSR sensitivity by the loading jump tests was also evaluated by Kasada et al. ²⁶⁾ with the argument that an increase in strain rate would deliver more reliable SRS results, because the indentation

tip may keep more continuous contact with the testing material during loading than during unloading. They defined the NI-hardness after loading jump by the plateau NI-hardness value, see the blue lines in the bottom image of Figure 4.2. In their method ²⁶⁾, however, since the NI-hardness values before and after loading jump are not those at the same indentation depth, it should be treated in analogy to the unloading method ²⁵⁾, although the delay in reaching the target value of indentation strain rate $\dot{\epsilon}$ is very small in the case of loading jump. In this work here, the hardness value that most matches with the position where the target indentation strain rate was reached first time was used, instead of the plateau hardness value. The hardness values before and after the SRJ for unloading and loading jump that have been obtained by the two methods are marked in Figure 4.2 by red and blue dots, respectively.

4.3.2 Irradiation Effect on m Value

The LSR sensitivity, m value, evaluated by SRJ tests of unloading and loading for unirradiated and irradiated W{001} is given in Figure 4.3(a) and Figure 4.3(b), respectively. Both methods, unloading and loading, led to the same conclusion, although the m values obtained by the loading tests are smaller than those by the unloading tests. Generally, the Fe³⁺ irradiation caused a slight decrease in m value and this trend is enhanced by increasing the damage level in both the cases of SRJ tests from 0.3 s⁻¹ to 0.01 s⁻¹ and from 0.03 s⁻¹ to 0.001 s⁻¹. The m values for the higher LSR regime are larger and the effect of decreasing m by irradiation seems to be more evolved in the unloading tests. The SSE ³⁵⁾ of SRS vanished at 800 nm, except for the 2 dpa condition, which is considered to be due to a lack of contribution of irradiated area to the strain rate sensitivity for the specimen irradiated to 0.1 and 1 dpa, but a remaining irradiation effect at around 900 nm in the specimen irradiated to 2 dpa.

The m values obtained for unirradiated W{001} in this study are reasonably above and below the m values obtained by Maier et al. ²⁵⁾ (LSR change from 0.05s⁻¹ to 0.005s⁻¹) for the

higher and lower LSR regime in the current SRJ test, respectively. However, our SRJ unloading results, which are rather scattered, suggest that the ISE²⁴⁾ on the LSR sensitivity cannot be neglected in this study.

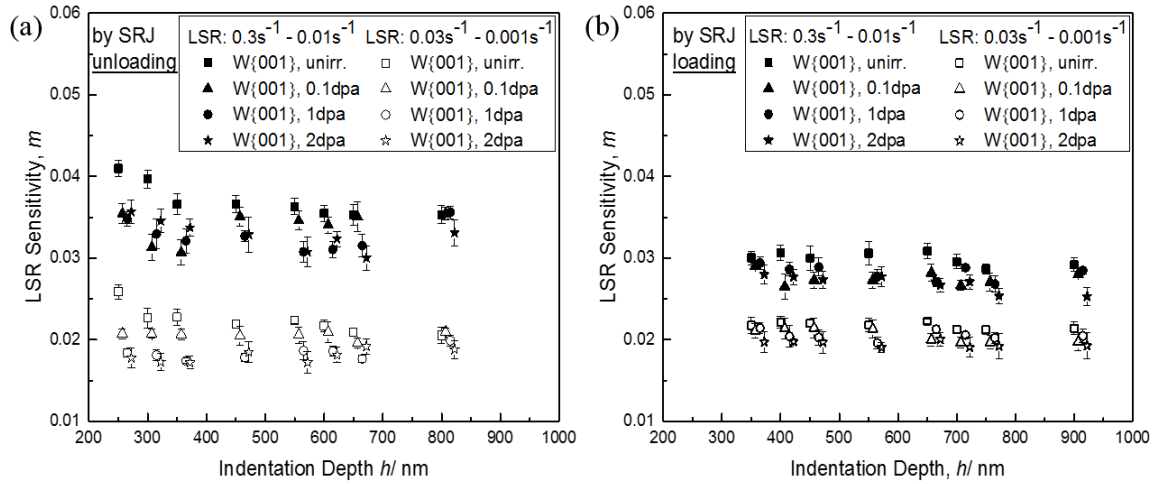


Figure 4.3: Averaged LSR sensitivity m over indentation depth h for unirradiated and ion-irradiated $W\{001\}$ using (a) SRJ unloading test method, (b) SRJ loading test method.

(Overlapped data points are shifted slightly from the actual indentation depth for eye-friendly plotting.)

The obtained m values are ranging from approximately 0.015 to 0.04 for SRJ tests and from approximately 0.0425 to 0.06 for CSR tests, as shown in Figure 4.4 before and after irradiation.

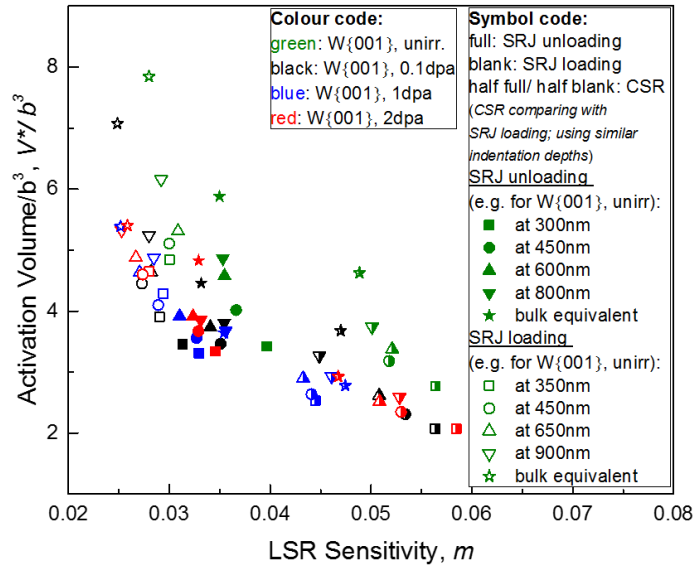


Figure 4.4: Averaged SRS (LSR sensitivity and bulk equivalent LSR sensitivity) vs. averaged activation volume V^* (local activation volume and bulk equivalent activation volume), normalized by unit volume b^3 where b is Burgers vector of W , for unirradiated and ion-irradiated $W\{001\}$ at various indentation depths h .

The absolute m values indicate a strong LSR dependence of NI-hardness, reflecting the high lattice friction in bcc W at RT²⁵⁾ where the deformation is controlled by the thermally activated motion of screw dislocations. The decrease in the LSR sensitivity of NI-hardness by irradiation can be explained in terms of an increase in the athermal stress caused by irradiation-induced obstacles against dislocation motion. Microstructure observations revealed, see chapter 7, that dislocation loops of interstitial type were formed as obstacles to the dislocation motion and the trend of further decrease in m values with the displacement damage suggests the number density of obstacles increase with displacement damage. The estimated m values obtained from the tensile test data (for the tests: SRS between $3 \times 10^{-2} \text{ s}^{-1}$ and $3 \times 10^{-4} \text{ s}^{-1}$ for temperatures 700 K and 922 K) of neutron ($0.5 \times 10^{26} \text{ n/m}^2$ at 644 K and $0.9 \times 10^{26} \text{ n/m}^2$ at 655 K) irradiated W by Steichen

¹⁹⁾ (the neutron fluence corresponds to roughly 1.1dpa ^{47, 48)}) are around 0.035, which agrees with the m values obtained in this research for ion-irradiated W{001} by NI test method. Larger m values in CSR tests than those in SRJ tests might be attributed to the difference in the test method as follows. Since in the NI-hardness measurement, the deformation area is limited to the localized area beneath the indentation, the LSR change could not be immediately reflected on the enough amount of dislocation motion in comparison to tensile test method. Especially an abrupt LSR change during ongoing indentation in loading as well as unloading SRJ tests, the stress relaxation is significant. Stress relaxation causes an apparent reduction of machine stiffness which could reduce the LSR in NI tests and SRJ tests. Therefore, the m values are smaller in SRJ tests than in CSR tests.

4.3.3 Irradiation Effect on V^*

The activation volume, which is normalized by unit volume b^3 where b is the Burgers vector of W with 0.2741 nm, was obtained according to equation (4.3) and the results are shown in Figure 4.5(a) and (b) for unloading and loading jump test method, respectively, indicating that the activation volume seems to be slightly decreased by ion-irradiation. At each indentation depth, the activation volume of the irradiated W{001} is smaller than that of the unirradiated W{001}, and it tended to linearly increase with increasing indentation depth irrespective of irradiation condition or SRJ calculation method. Since the m values are decreased by irradiation, it is considered that the effective stress is reduced while long range athermal stress is increased. It is also considered that the irradiation-induced reduction of activation volume could be interpreted in terms of long range stress field suppressing the kink pair motion caused by the irradiation-induced obstacles. Set-up 10, 11 and 12 in unirradiated W{001} serves higher activation volumes than the trend line, of which the reason could be attributed to the ISE ²⁴⁾ or measurement artifacts in low LSR tests in general. Unfortunately, Maier et al. ²⁵⁾ do not show

comparable data at indentation depths between their data points of 200 nm and 400 nm. At lower LSR, the small NI-hardness changes by SRJ were difficult to estimate, and especially in the shallow indentation depth, the NI-hardness profile varied quite significantly with each individual test. This is reflected in the fluctuation of V^* , but not visible in the LSR sensitivity. Thus, the discussion in this work here is focused on the SRJ tests at higher LSR regime 0.3 s^{-1} to 0.01 s^{-1} .

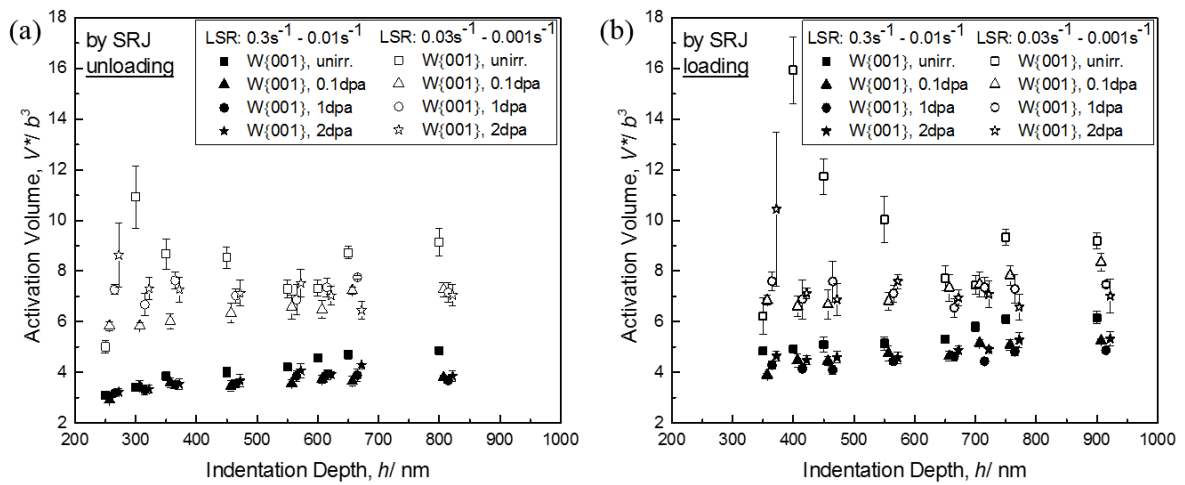


Figure 4.5: Averaged local activation volume V^* normalized by unit volume b^3 where b is Burgers vector of W , over indentation depth for unirradiated and ion-irradiated $W\{001\}$ using (a) SRJ unloading test method, (b) SRJ loading test method. (Overlapped data points are shifted slightly from the actual indentation depth for eye-friendly plotting.)

4.3.4 SRS of Bulk Equivalent NI-hardness

The SRS of bulk equivalent NI-hardness was estimated on the basis of the Nix and Gao model²⁴⁾ applied to the ion-irradiated materials by Kasada et al.⁴⁶⁾. Note that H^2 versus $1/h$ profiles were used to obtain the unknown H_0 and $H_{irr, bulk}$. In Figure 4.6, the Nix and Gao²⁴⁾ plots for tests at two different LSR levels are shown to estimate bulk equivalent NI-hardness in

the case of irradiated W{001} to 0.1 dpa evaluated by SRJ^{23, 25)} test method - unloading and loading - and CSR test method.

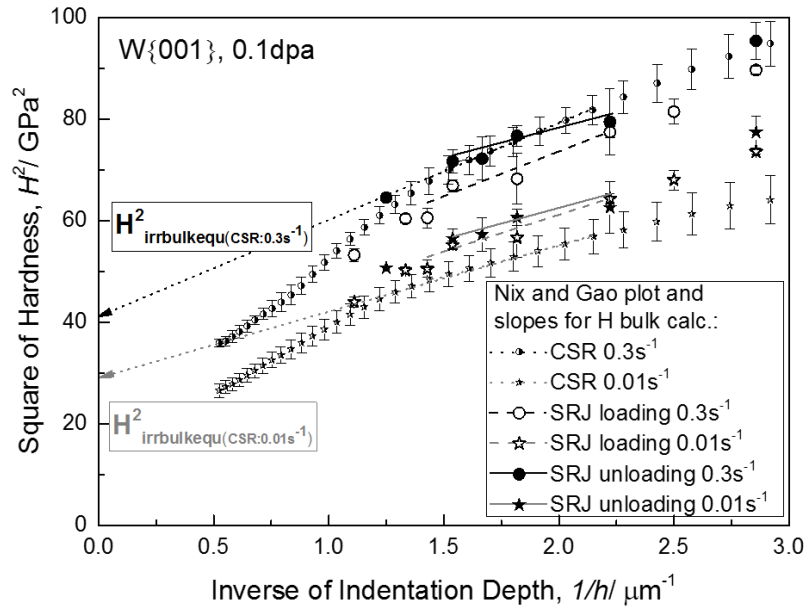


Figure 4.6: Nix and Gao plot for SRJ tests (loading and unloading method) and CSR tests for 0.1 dpa W{001}.

The bulk equivalent NI-hardness values were calculated according to equation (4.4), from which the m values were obtained according to equation (4.2). The obtained bulk equivalent NI-hardness for irradiated W{001} to 0.1 dpa by the SRJ loading/unloading test method at LSR of $0.01s^{-1}$ and $0.3s^{-1}$ is 5.57GPa/6.53GPa and 6.06GPa/7.31GPa, compared to 5.44GPa and 6.39GPa by CSR test method. This results in the m values of 0.025/0.033 by SRJ loading/unloading test method and of 0.047 by CSR test method. The obtained bulk equivalent hardness and obtained bulk equivalent SRS for unirradiated and 0.1dpa irradiated W{001} are summarized in Table 4.2.

Set-up	H at 0.3s ⁻¹ [GPa] Unirr/ 0.1dpa	H at 0.01s ⁻¹ [GPa] Unirr/ 0.1dpa	bulk equivalent SRS m [-] Unirr/ 0.1dpa
SRJ loading	4.87/ 6.06	4.43/ 5.57	0.028/ 0.025
SRJ unloading	5.27/ 7.31	4.67/ 6.53	0.036/ 0.033
CSR	4.9/ 6.39	4.15/ 5.44	0.049/ 0.047

Table 4.2: Summary of bulk equivalent hardness and obtained bulk equivalent SRS for unirradiated/ 0.1 dpa irradiated W{001}.

Generally, the LSR sensitivity as well as bulk equivalent LSR sensitivity results show values of the same order of magnitude compared with the only available SRS data source for tensile tested neutron irradiated W¹⁹⁾.

In the original work on NI-SRJ tests²³⁾ on nanocrystalline nickel, it was reported that by the tests at a LSR of 0.05s⁻¹, the NI-hardness changes were almost the same between CSR tests and SRJ tests. However, decreasing the LSR led to a slight decrease in NI-hardness by SRJ tests, but to a remarkable decrease of NI hardness by CSR tests. This resulted in a higher LSR sensitivity of NI-hardness by CSR tests²³⁾. This could explain the experimental result of this work at the LSR of 0.3 s⁻¹ that the NI-hardness was in good agreement between SRJ unloading tests and CSR tests. However, the NI-hardness after SRJ loading jump did not reach the target value of NI-hardness by CSR tests again. This difference in NI-hardness according to different testing methods can be seen in Figure 4.6.

Figure 4.4 also summarizes the relationship between LSR sensitivity m and activation volume V^* (average values) obtained for each irradiation condition for SRJ loading test method and CSR test method. Although the data is scattered among the plots obtained by the different

methods, the effect of ion-irradiation could be confirmed to reduce both the m value and the V^* . This suggests that the ion-irradiation induced hardening is due to the increase in the obstacles to dislocation motion through the long range interaction with athermal motion of dislocations. As for the ion-irradiation induced obstacles, it is considered that the dislocation loops are the main defect structures, and the detailed microstructure examination study will be shown in chapter 7. Furthermore Figure 4.4 shows that the damage level does not have a significant effect on the LSR sensitivity, which is considered to be due to the fact that the ion-irradiation effects on the LSR sensitivity saturate at a low damage level of 0.1 dpa.

4.4 Conclusions

LSR dependence of NI-hardness was investigated by using CSR test method and SRJ test method for W{001} single crystal specimens before and after 6.4 MeV Fe³⁺ irradiations (nominal damage level of 0.1, 1 and 2 dpa, 573 K) to evaluate the effect of ion-irradiation on the LSR sensitivity of NI-hardness at RT. The obtained main conclusions are as follows:

- 1) Ion-irradiation increased NI-hardness and slightly decreased LSR sensitivity of NI-hardness at all damage levels. The effect was more pronounced with increasing damage level. The m values were large ranging between 0.015 and 0.04 in SRJ tests, and between 0.0425 and 0.06 in CSR tests. This indicates that the deformation of bcc W{001} at RT was controlled by a high lattice friction stress both before and after the ion-irradiation.
- 2) The decrease in LSR sensitivity by ion-irradiation could be attributed to the increase in the athermal stress caused by ion-irradiation induced defect structures, which was reflected to a slight decrease, or even no change, in the activation volume in irradiated W{001}.
- 3) The SSE³⁵⁾ of SRS vanished at 800 nm, except for the 2 dpa condition, which is considered to be due to a lack of contribution of irradiated area to the strain rate sensitivity for the specimen

irradiated to 0.1 and 1 dpa, but a remaining irradiation effect at around 900 nm in the specimen irradiated to 2 dpa.

4) The bulk equivalent LSR sensitivity m and bulk equivalent activation volume V^* obtained from the bulk equivalent hardness showed reasonable values compared with the values of the averaged LSR sensitivity m over the indentation depth h .

4.5 Appendix

List of abbreviations used in the text:

(in alphabetical order)

CSM	Continuously stiffness method
CSR	Constant strain rate
ISE	Indentation size effect
LSR	Local strain rate
SRJ	Strain rate jump
SRS	Strain rate sensitivity
SSE	Softer substrate effect

4.6 References

- 1) K. Ezato; S. Suzuki; Y. Seki; K. Mohri; K. Yokoyama; F. Escourbiac; T. Hirai and V. Kuznetsov: *Fus. Eng. Des.* **98–99** (2015) 1281-1284.
- 2) M. Merola; F. Escourbiac, A. R. Raffray, P. Chappuis, T. Hirai, S. Gicquel and I. B. Agcy: *Fus. Eng. and Des.* **96-97** (2015) 34-41.
- 3) H. Bolt, V. Barabash, W. Krauss, J. Linke, R. Neu, S. Suzuki, N. Yoshida, A. U. Team: *J. Nucl. Mater.* **329** (2004) 66-73.
- 4) A. Hasegawa; M. Fukuda.; T. Tanno and S. Nogami: *Mater. Trans.* **54** (2013) 466-471.
- 5) M. Fukuda, A. Hasegawa, T. Tanno, S. Nogami and H. Kurishita: *J. Nucl. Mater.* **442** (2013) S273-S276.
- 6) V. Barabash, G. Federici, M. Rodig, L. L. Snead and C. H. Wu: *J. Nucl. Mater.* **283** (2000) 138-146.
- 7) V. Barabash, G. Federici, J. Linke and C. H. Wu: *J. Nucl. Mater.* **313** (2003) 42-51.
- 8) M. R. Gilbert, S. L. Dudarev, D. Nguyen-Manh, S. Zheng, L. W. Packer and J. C. Sublet: *J. Nucl. Mater.* **442** (2013) S755-S760.
- 9) A. Hassanein, T. Sizyuk and I. Konkashbaev: *J. Nucl. Mater.* **390–391** (2009) 777-780.
- 10) K.- I. Fukumoto; T. Onitsuka and M. Narui: *Nucl. Mater. En.* (2016) DOI:10.1016/j.nme.2016.03.010.
- 11) A. S. Wronski, G. A. Sargent and A. A. Johnson: In *Flow and Fracture of Metals and Alloys in Nuclear Environments: A Symposium presented at the Sixty-seventh Annual Meeting ASTM*, ASTM special technical publication No. 380, ASTM International: Chicago (1965) pp 69-85.
- 12) M. Tanaka, K. Fukaya and K. Shiraishi: *Trans. Jap. Inst. Metals* **20** (1979) 697-705.13.
- 13) M. Li, M. Eldrup, T. S. Byun, N. Hashimoto, L. L. Snead and S. J. Zinkle: *J. Nucl. Mater.* **376** (2008) 11-28.

- 14) Y. Aono, E. Kuramoto, N. Yoshida; H. Kurishita and H. Kayano: Effets of Radiation on Materials: 16th International Symposium, ASTM STP 1175, A. S. Kumar, D. S. Galles, R. K. Nanstad and E. A. Little, Eds., ASTM: Philadelphia (1994) pp.130-143.
- 15) S. M. Ohr and E. D. Bolling: UC-25-Metals, Ceramics, and Materials (Oak Ridge National Laboratory 1967) pp.13-20.
- 16) S. B. McRickard: Acta Metall. **16** (1968) 969-974.
- 17) J. M. Steichen and J. A. Williams: Heavy Section Steel Technology Report Program Technical Report No.32; HEDL-TME 73-74 (Hanford Engineering Development Laboratory 1973).
- 18) J. M. Steichen and J. A. Williams: J. Nucl. Mater. **57** (1975) 303-311.
- 19) J. M. Steichen: J. Nucl. Mater. **60** (1976) 13-19.
- 20) P. Bennett and G. Sinclair: J. Bas. Eng. **88** (1966) 518-524.
- 21) M. J. Mayo and W. D. Nix: Acta Metall. **36** (1988) 2183-2192.
- 22) E. W. Hart: Acta Metall. **15** (1967) 351-355.
- 23) V. Maier, K. Durst, J. Mueller, B. Backes, H. W. Höppel, H. W. and M. Göken: J. Mater. Res. **26** (2011) 1421-1430.
- 24) W. D. Nix and H. Gao: J. Mech. Phys. Solids **46** (1998) 411-425.
- 25) V. Maier, C. Schunk, M. Göken and K. Durst: Phil. Mag. **95** (2015) 1766-1779.
- 26) R. Kasada, S. Konishi, D. Hamaguchi, M. Ando and H. Tanigawa: Fus. Eng. Des. **109–111**, Part B (2016) 1507-1510.
- 27) C. Sun, J. Ma, Y. Yang, K. T. Hartwig, S. A. Maloy, H. Wang and X. Zhang: Mat. Sci. Eng. A **597** (2014) 415-421.
- 28) A. Kohyama, Y. Katoh, M. Ando and K. Jimbo: Fus. Eng. Des. **51-52** (2000) 789-795.
- 29) "INTERACTION OF IONS WITH MATTER" by J.F. Ziegler <http://www.srim.org/>,

(accessed 2016-09-17).

- 30) ASTM standard E521-98 (2009), Standard Practice for Neutron Radiation Damage Simulation by Charged Particle Irradiation.
- 31) W. Yao: Crystal Plasticity Study of Single Crystal Tungsten by Indentation Tests. Doctoral Thesis, Ulm University, Ulm, 2012 <http://dx.doi.org/10.18725/OPARU-2456>.
- 32) B. Lucas and W. Oliver: Metall. Mater. Trans. A **30** (1999) 601-610.
- 33) Y. T. Cheng and C. M. Cheng: Surf. and Coat. Technol. **133–134** (2000) 417-424.
- 34) W. C. Oliver and G. M. Pharr: J. Mater. Res. **7** (1992) 1564-1583.
- 35) I. Manika and J. Maniks: J. Phys. D-Appl. Phys. **41** (2008) p. 074010.
- 36) N. Moody, A. Strojny, D. Medlin, S. Guthrie and W. Gerberich: Test rate effects on the mechanical behavior of thin aluminum films, MRS Proceedings, (Cambridge Univ Press: 1998) p 281.
- 37) H. Conrad: On the mechanism of yielding and flow in iron (Atomics International. Div. of North American Aviation, Inc., Canoga Park, Calif. 1961) DOI: 10.2172/4064971.
- 38) H. Conrad, L. Hays, G. Schoeck and H. Wiedersich: Acta Metall. **9** (1961) 367-378.
- 39) H. Conrad and W. Hayes: Am. Soc. Metals, Trans. Quart. **56** (1963).
- 40) A. Seeger: *Dislocations and mechanical properties of crystals* (Wiley, New York, 1957) 243.
- 41) G. Gibbs, G.: Physica Status Solidi (b) **10** (1965) 507-512.
- 42) Q. Wei, S. Cheng, K. T. Ramesh and E. Ma: Mat. Sci. Eng. A **381** (2004) 71-79.
- 43) R. J. Asaro and Suresh: Acta Mater. **53** (2005) 3369-3382.
- 44) J. Chen, L. Lu and K. Lu: Scripta Mater. **54** (2006) 1913-1918.
- 45) L. Lu, R. Schwaiger, Z. Shan, M. Dao, K. Lu and S. Suresh: Acta Mater. **53** (2005) 2169-2179.
- 46) R. Kasada, Y. Takayama, K. Yabuuchi and A. Kimura: Fus. Eng. Des. **86** (2011) 2658-

2661.

47) A. Emri, DEO-ER-0313/18 p.63.

48) L.R. Greenwood and F.A. Garner: J. Nucl. Mater. **212-215** (1994) 635-639.

Chapter 5:

Evaluation of Ion-irradiation Hardening of Tungsten Single Crystals by Nanoindentation Technique Considering Material Pile-up Effect

5.1 Introduction

Tungsten (W) is a candidate material for plasma facing components in future fusion power plants¹⁻⁴⁾. To simulate fusion environment for W, ion-irradiation is extensively in use⁵⁻¹⁰⁾. A realistic estimation of the actual irradiation hardening behaviour by ion-irradiation experiments in W is essential in order to apply it as a plasma facing component in fusion power reactors. The nanoindentation (NI) technique is a recognized method to measure hardness in ion-irradiated materials, which show a complex distributed damaged layer of a few microns near the irradiated surface. This inhomogeneous defect distribution is a challenge for giving a realistic and representative estimation of expected irradiation hardening behaviour. Analysing the NI-results is not straight forward even for unirradiated materials, since testing artefacts may occur and overlap with phenomena intrinsic to the material. Such testing artefacts can arise from the NI-system itself, for example by the usage of a non-ideal “blunt” indenter shape¹¹⁾ or by the surface detection technique¹²⁾. Additionally, artefacts may come from insufficient preparation of the testing surface. On the other hand, the indentation size effect (ISE), described by Nix and Gao¹³⁾, i.e. increase in hardness with decreasing depth, appears in the obtained NI-profiles, which is considered to be a behaviour that is inevitable for the NI measurement. Furthermore, the softer substrate effect (SSE)¹⁴⁾, can be observed in the NI- profile of a hard thin film on a soft substrate.

The material pile-up or sink-in heights that arise around the permanent indents in the testing material should also be taken into account because of the definition of NI-hardness which depends on the indentation project area of contact as a function of contact depth. The ratio of elastic modulus E_S to yield stress σ , E_S/σ , as well as the hardening coefficient n of the tested material can predict whether pile-up or sink-in will appear in a material^{15, 16)}. Bolshakov and Pharr¹⁶⁾ reported that in materials with a high E_S/σ ratio or alternatively a ratio of final displacement after complete unloading to maximum depth higher than 0.7, $0.7 > h_f/h_{max}$, Oliver and Pharr method^{11, 15)} does

not give reasonable results since pile-up is of significant size. This infers that W, having a high E_s/σ ratio, will undergo pile-up while NI-testing.

The pile-up corrected hardness for unirradiated (001) W single crystal has been reported by Lee et al.^{17, 18)} who proposed two methods, one by considering a Hertzian loading^{19, 20)} analysis¹⁷⁾ and the other by a determination of the closed contact boundary¹⁸⁾ by an imaging procedure.

Armstrong et al.⁸⁾ reported that for NI-testing on W-5wt% tantalum alloy before and after W ion-irradiation (0.07, 1.2, 13 and 33dpa at 573K) the pile-up formation around the indents was affected by the irradiation. They reported that the unirradiated W showed extensive pile-up whereas for damage levels of 0.07dpa and 1.2dpa the pile-up was drastically suppressed⁸⁾. However, no corrected hardness method was given in the work. Recently, Heintze et al.²¹⁾ proposed the so-called elastic-modulus-based correction (EMC) method to correct NI-hardness for pile-up formation. The EMC method²¹⁾ uses the square function of indentation modulus to elastic modulus to correct NI hardness. Further, the EMC²¹⁾ correction factor involves the reduced elastic modulus which includes the elastic properties of the indenter as well. The EMC method²¹⁾ has been evaluated on unirradiated, self-ion irradiated (2.5dpa and 3.5 dpa at 473K) and neutron irradiated (2.31 dpa at 473K) 9% Cr ferritic/martensitic steel T91. Ultrasonic pulse-echo technique results showed no significant difference between the elastic moduli of unirradiated and neutron-irradiated ferritic/martensitic steel T91. Hence, the EMC method²¹⁾ is based on the assumption that the elastic modulus is independent of irradiation²¹⁾. Beck et al.²²⁾ very recently proposed a method to correct NI-hardness of ion-irradiated (0.24±0.02dpa at 573K) W-1wt%Re alloy. They introduced a correction factor C_{cor} that reflected the difference in the actual elastic modulus between the ion-irradiated damaged layer and unirradiated material which were measured by transient grating laser measurements.

In this work here it is assumed that the EMC method will be more realistic to consider the effect of the elastic properties of the indenter and the detailed reason will be discussed later. Also,

these EMC methods require no thorough measurement of contact areas of remained indenter imprints, although Hardie et al.²³⁾ suggested the possible way to measure the actual area of contact by scanning electron microscopy (SEM).

The number of reports about the pile-up effect on NI-hardness of ion-irradiated metals is limited. But in the case of W with a high E_S/σ ratio, the pile-up effect is inevitable and must be considered for evaluating ion-irradiation hardening effects. Because of the above mentioned features and assumptions of the EMC method²¹⁾ over the other existing methods, in this work here, ion-irradiation hardening of W single crystal is evaluated with consideration of material pile-up effects in order to assess the most feasible analytical method of NI-hardness.

5.2 Experimental Method

5.2.1 Material and Sample Preparation

The material used is a W single crystal with a purity of 99.97 %. The surface orientation of the W single crystal has been confirmed to be (001) by electron backscatter diffraction (EBSD) measurement. A detailed description of the material and sample preparation is shown in the previous chapter, chapter 4.

5.2.2 Ion-irradiation

Three specimens were irradiated using the dual-beam irradiation experiment test facility (DuET) at Kyoto University²⁶⁾. Irradiation with 6.4 MeV Fe³⁺ ions was performed to a nominal displacement damage of 0.1, 1 and 2dpa, respectively, at 573 K. The target depth profiles of the displacement damage and ion distribution have been calculated using the SRIM (the stopping and

range of ions in matter) package ²⁷⁾ and are described in detail in chapter 4. From SRIM code ²⁷⁾ results, irradiation defects are expected to form up to a penetration depth of approximately 2 μm .

5.2.3 Nanoindentation Tests

NI-tests on the unirradiated and ion-irradiated specimens were carried out using a NanoIndenter G200 of Agilent Technologies Inc., operated with a Berkovich diamond tip. Basic hardness tests, according to Oliver and Pharr's method ¹¹⁾, were carried out at various indentation depths h between 300nm and 1700nm at a strain rate target of 0.05s^{-1} , which is determined by the ratio of loading rate to load, \dot{P}/P . The peak load holding time was set to 10s. Five NI-tests were carried out at each indentation depth h , and one representative test at each indentation depth was considered further. The indenter was positioned such that one side of the Berkovich triangle was perpendicular to a $\langle 111 \rangle$ type orientation. NI-tests on each of the specimens were performed in a row to ensure the same azimuthal orientation of the indent with respect to the crystal orientation. The accuracy of the azimuthal indenter orientation has been confirmed by EBSD and can be seen in Figure 5.1 for an indent in the unirradiated specimen.

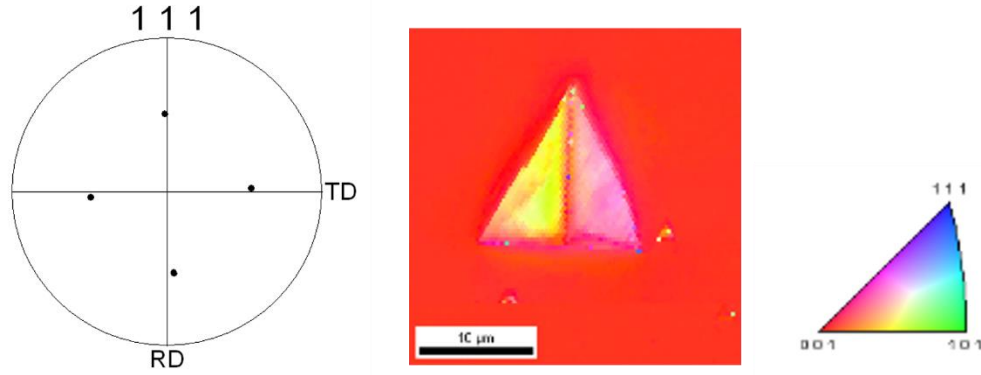


Figure 5.1: Electron backscattered diffraction patterns of unirradiated $W\{001\}$ showing the azimuthal orientation of indent with respect to local crystal orientation.

5.2.4 Pile-up Height Measurement

In addition to a numerical study, the heights of the three evolved pile-ups around the three-sided Berkovich tip was measured by atomic force microscopy (AFM) with scanning in the direction parallel to the $\langle 111 \rangle$ orientation

5.3 Analytical Method for Pile-up Corrected Hardness:

5.3.1 Pile-up Corrected Hardness

According to ISO standards related to NI-testing²⁸⁾, NI-hardness H_{IT} is the mean contact pressure below the indent and is shown by equation (5.1), called the uncorrected NI hardness further on:

$$H_{IT} = F_{max} / A_P^{ISO} \quad (5.1)$$

where F_{max} is the maximum force applied and A_P^{ISO} is the projected contact area according to Oliver and Pharr¹¹⁾. As for the E-modulus of the NI test system, based on Sneddon's equation²⁹⁾, Bulychev, Alekhin, Shorokov and their co-workers³⁰⁻³⁴⁾ presented the following equation (5.2) for a composite modulus E^* (composed of the apparent specimen modulus - the indentation modulus - E_{IT} and indenter modulus, E_I):

$$E^* = \sqrt{\pi} S / (2\beta \sqrt{A_P^{ISO}}) \quad (5.2)$$

where A_P^{ISO} is the projected contact area, S is the stiffness considered to be affected by the contact area and a correction factor β for the elastic recovery upon removal of load, which was set to the value of 1.0 in this work.

As it is shown by equation (5.2), E^* is inversely proportional to the square root of the projected contact area, which becomes relevant later on in chapter. The composite modulus E^* is given by the following equation¹¹⁾:

$$1/E^* = (1 - \nu_s^2)/E_{IT} + (1 - \nu_I^2)/E_I \quad (5.3)$$

where E_I is the elastic modulus of the indenter, and ν_I is the corresponding Poisson's ratio. For a diamond Berkovich tip the values are: $E_I = 1141$ GPa, $\nu_I = 0.07$ ¹¹⁾. E_{IT} is the measured and apparent modulus of the tested material by the G200 testing machine and ν_s is the Poisson's ratio of the tested material (ν_s is 0.28 in the case of W). In Oliver and Pharr's method¹¹⁾, the stiffness S is obtained by the unloading curve of the indentation from the following equation:

$$h_c^{ISO} = h_{max} - \varepsilon(h_{max} - h_r) = h_{max} - \varepsilon F_{max}/S \quad (5.4)$$

where $(h_{max} - h_r)$ is the difference between h_{max} , the maximum depth from the initial surface, and h_r , the intercept of the depth axis with the tangent to the unloading curve. $(h_{max} - h_r)$ is further defined by the maximum force applied F_{max} divided by the stiffness S of the tested specimen. ε is a geometric factor, for Berkovich indenters 0.75. The correlation of the different terms of indentation

depth are shown in Figure 5.2 with $h_{max} = 400\text{nm}$ and h_p being the permanent deformation depth in the tested specimen after load removal.

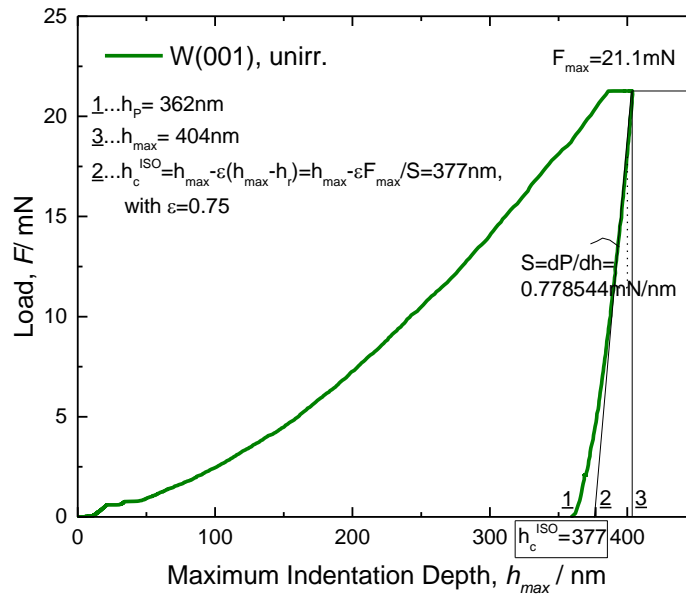


Figure 5.2: An example of an F_{max} vs. h_{max} profile for unirr. W(001) up to approximately 400 nm indentation depth.

Thus, NI hardness H_{IT} and E_{IT} can be obtained from equation (5.1) to (5.4).

From equations (5.1) and (5.2), a correlation between uncorrected hardness H_{IT} and corrected hardness H^{EMC} can be obtained as shown in equation (5.5):

$$H^{EMC} = H_{IT} \times A_P^{ISO} / A_P^{EMC} = H_{IT} \times (E^{EMC*} / E^*)^2 \quad (5.5)$$

Based on the findings by Sneddon ²⁹⁾ as well as later on by other researchers, Bulychev, Alekhin, Shorokov and their co-workers ³⁰⁻³⁴⁾, Heintze et al. ²¹⁾, Beck et al. ²²⁾ and Hardie et al. ²³⁾ recently proposed different methods for pile-up corrected hardness. In equation (5.5), A_P^{EMC} is the true projected area of contact including pile-up and E^{EMC*} is the calculated composite modulus, in analogy to equation (5.3) of the elastic modulus of the indenter E_I and the actual elastic modulus of the material E_S , using $E_I=1141$ GPa, $\nu_I=0.07$ ¹¹⁾ for a diamond tip and $E_S=410$ GPa ¹¹⁾, $\nu_S=0.28$ for W. Therefore it can be said that E_S is associated with the true projected area of contact including pile-up A_P^{EMC} .

Note that the symbols used in this chapter as shown in the “List of Symbols” are somewhat different from those in the original works by S. I. Bulychev ³⁰⁻³⁴⁾, or as in Heintze et al. ²¹⁾, Beck et al. ²²⁾ and Hardie et al. ²³⁾. Heintze et al.’s ²¹⁾ pile-up corrected hardness method, which can be called as the elastic modulus correction (EMC) method, was assessed on unirradiated, neutron irradiated and self-ion-irradiated 9 wt.% Cr f/m steel T91. An advantage of the EMC ²¹⁾ method is that one actually does not have to measure the pile-up height, but can use the latter expression of H^{EMC} in equation (5.5) that only includes the square of the ratio of E^{EMC*} to E^* . Beck et al. ²²⁾ also uses the elastic modulus expression, but they don’t consider the elastic properties of the indenter in the modulus expressions. Further on, based on their ²²⁾ transient grating laser measurement results, they assumed that the elastic modulus of the specimen was changed after ion-irradiation. Hardie et al. ²³⁾ on the other hand recently used the concept of area expression of equation (5.5) to calculate a pile-up corrected hardness for iron ion-irradiated (6.18 dpa at 593 K) Fe-12wt%Cr alloy, $H/A_{actual}/A_{cc}$, which required thorough measurement of the area by scanning electron microscopy (SEM), which is called as the pile-up correction (PUC) method ²³⁾.

In the following, the elastic modulus expression of equation (5.5) will be used and to some extent the concepts of EMC method by Heintze et al. ²¹⁾ to evaluate the pile-up effect on ion-irradiation hardening in pure {001} W single crystal of various radiation damage levels. What this

work here has in common with the EMC ²¹⁾ is that it considers the elastic modulus to be unchanged by irradiation. However, in the case of Heintze et al. ²²⁾ the elastic modulus (219 GPa) and the measured indentation modulus E_{IT} of unirradiated 9 wt.% Cr F/M steel T91 was very stable over indentation depth and similar in magnitude. As will be shown later in Figure 5.3 (a), the situation is different here, that is in W, firstly because the measured indentation modulus E_{IT} of irradiated as well as unirradiated W(001) varies with indentation depth and secondly the magnitude of both irradiated as well as unirradiated W(001) are about 10% to 35% higher than the target elastic modulus E_S in literature ¹¹⁾, 410GPa. Therefore, in this work here both the unirradiated as well as the irradiated W{001} are corrected for pile-up consideration and set the elastic modulus E_S as the target value of the unirradiated W{001}, 410GPa. Also the NI-hardness is corrected for each h_{max} individually, which will be shown later. This is contrary to Heintze et al. ²¹⁾, who used an averaged correction factor C_{EMC} for contact depths between 60 nm and 650 nm.

In addition to the EMC method, the true projected area of contact including pile-up corresponding to the pile-up corrected hardness H^{EMC} was of interest:

$$A_P^{EMC} = F_{max} / H^{EMC} \quad (5.6)$$

Since describing the full shape of this area, A_P^{EMC} , is difficult, as can be seen in Hardie et al. ²³⁾, the focus was laid on a so called representative depth including pile-up, $z_{calc.}^{pile-repr.}$, which is associated with A_P^{EMC} and can be calculated by numerical parameters fit to the Oliver and Pharr method ¹¹⁾.

$$A_P^{EMC} = C_0 z_{calc.}^{pile-repr.2} + C_1 z_{calc.}^{pile-repr.} + C_2 z_{calc.}^{pile-repr.1/2} + C_3 z_{calc.}^{pile-repr.1/4} + C_4 z_{calc.}^{pile-repr.1/8} + C_5 z_{calc.}^{pile-repr.1/16} + C_6 z_{calc.}^{pile-repr.1/32} + C_7 z_{calc.}^{pile-repr.1/64} + C_8 z_{calc.}^{pile-repr.1/128} \quad (5.7)$$

The purpose was to gain an understanding of the order of magnitude of an averaged pile-up height $\bar{z}_{calc.}^{pile-repr.}$:

$$\bar{z}_{calc.}^{pile-repr.} = z_{calc.}^{pile-repr.} - h_c^{ISO}. \quad (5.8)$$

For comparison, the actual highest pile-up height, $\bar{z}_{measured}^{pile-max}$, was measured by AFM with scanning in the direction parallel to the $\langle 111 \rangle$ orientation.

5.3.2 Ion-irradiation Hardening Evaluation

The analysis method of ion-irradiation hardening by NI-hardness measurement is based on the Nix-Gao model ¹³⁾ and Kasada et al. method ³⁵⁾. Nix and Gao developed a model based on the concept of geometrically necessary dislocation ¹³⁾, which is described in the following equation showing the depth dependence of hardness:

$$H/H_0 = \sqrt{1 + (h^*/h)} \quad (5.9)$$

where H is the hardness at a certain indentation depth, h , and H_0 is the hardness at the limit of infinite depth ¹³⁾. h^* is a characteristic length that depends on the indenter shape, H_0 and the shear modulus, but is not a constant for a given material and indenter geometry ¹³⁾. It is a function of the statistically stored density via H_0 ¹³⁾. Ideally, plotting the square of the hardness ratio H/H_0 against the reciprocal of the indentation depth shall create a straight line with the slope being h^* , i.e. with a single value of h^* over testing depth ¹³⁾.

Kasada et al. ³⁵⁾ developed NI-techniques on ion-irradiated Fe-based ferritic alloys ³⁵⁾. They described the depth dependence of hardness by a model that is based on the ISE ¹³⁾ and extended it by a film/substrate system hardness model based on the Softer Substrate Effect ¹⁴⁾ (SSE); the unirradiated region below the irradiated region will be plastically deformed before the indenter itself reaches the unirradiated region. The point of transition is called the critical indentation depth h_{crit} and accounts for the position of the NI-hardness shoulder. With their model ³⁵⁾, the bulk equivalent hardness of the ion irradiated region, $H_{irr}^{bulkequ}$, can be obtained by the least square fitting of the hardness data up to a critical depth h_{crit} . Finally, a single quantitative value to describe irradiation hardening, ΔH , is available as the following equation shows:

$$\Delta H = H_{irr}^{bulkequ} - H_0 \quad (5.10)$$

5.4 Results and Discussions

The bulk equivalent hardness, $H_{irr}^{bulkequ}$, which is the hardness at infinite depth H_0 and the resulting irradiation hardening values, ΔH , are given in Table 5.1.

	Uncorrected results				EMC based method ²¹⁾			
	unirr.	0.1 dpa	1 dpa	2 dpa	unirr.	0.1 dpa	1 dpa	2 dpa
Bulk equivalent NI-hardness (Nix-Gao) $H_{irr}^{bulkequ}$. [GPa]	4.05	5.81	7.47	6.90	3.42	4.10	5.22	5.06
ΔH [GPa]		1.75	3.42	2.85		0.68	1.80	1.64

Table 5.1: Summary of bulk equivalent hardness and irradiation hardening before and after the correction by the EMC method ²¹⁾.

Figure 5.3 summarizes the results of NI-hardness, indentation modulus as well as the Nix and Gao-plot for evaluation of bulk equivalent hardness ³⁵⁾ and hardness at infinite depth ¹³⁾ for uncorrected results of the NI-technique and the EMC ²¹⁾ method. As for the uncorrected results of the NI-technique in Figure 5.3(a) and (b), one can see that the indentation modulus E_{IT} varies with h_{max} from approximately 550 GPa in a shallower depth to approximately 450 GPa in a deeper one, which is always above the elastic modulus E_S of W of approximately 410 GPa given by literature ¹¹⁾. Beck et al. ²²⁾ also reported a significant increase of indentation modulus in the shallow indentation depth up to 350 nm of about 475 GPa for He⁺ implantation (0.24±0.02 dpa at 573 K) in W-1wt%Re alloy and the value was still 420GPa at 2000nm h_{max} . In this work here, it is considered that this gap between E_{IT} and E_S at each h_{max} is caused by pile-up, which will be taken

into account by the EMC²¹⁾ method later on in Figure 5.3 (c), (d). As mentioned before, it is assumed that the elastic modulus is not changed by irradiation, thus E_s is the target value of E_{IT} for both unirradiated and irradiated W(001). In shallow depths the indentation modulus of unirradiated W(001) is generally lower than irradiated W(001) as can be seen in Figure 5.3 (a).

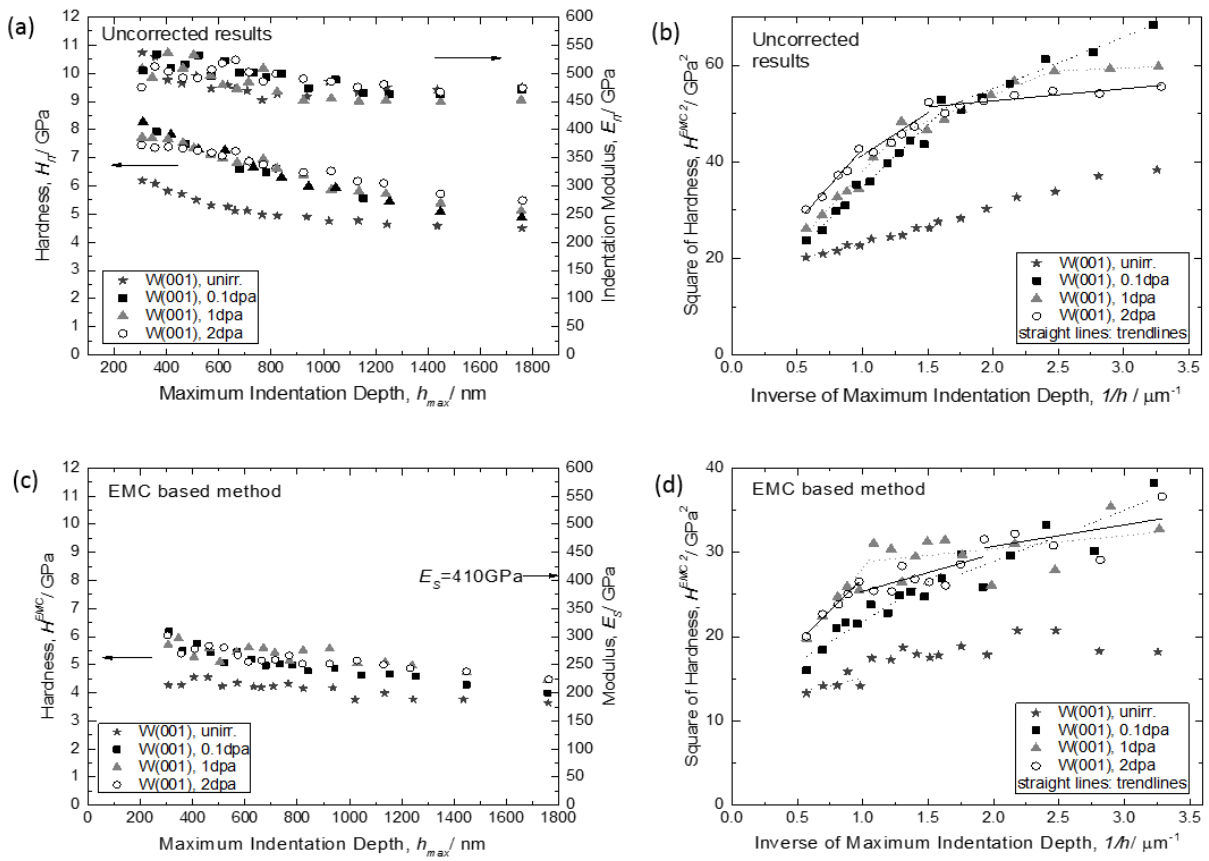


Figure 5.3: (a) uncorrected H_{IT} and E_{IT} and (c) corrected H^{EMC} associated with E_s for unirradiated and irradiated W{001}. Corresponding Nix-Gao¹³⁾ plot for unirradiated and irradiated W{001} of (b) uncorrected and (d) the EMC method²¹⁾.

As for the uncorrected NI-hardness, one can see in Figure 5.3 (a) that the irradiation effect is still significant at 1700 nm maximum indentation depth and increases with damage level. Hardness shoulder points in the $H-h_{max}$ profile became more pronounced in the Nix and Gao ¹³⁾ plots in Figure 5.3 (b). The plots for 0.1 dpa W(001) showed a hardness-shoulder, whereas interestingly those for 1 dpa and 2 dpa W{001} showed two hardness-shoulders, indicating an appearance at deeper h_{max} at higher damage levels. The SSE ¹⁴⁾ seemed to vanish beyond 1000nm as can be seen in Figure 5.3 (b). This led to two stage slopes in the Nix – Gao plot for 0.1 dpa and three stage slopes for 1 and 2 dpa, see Figure 5.3 (b).

Figure 5.3(c), (d) show the H^{EMC} results based on equation (5.5) and the Nix – Gao ¹³⁾ plots for the pile-up corrected hardness method. Comparing Figure 5.3(a) with Figure (c) shows that the NI-profile was roughly shifted by 1 GPa lower as the pile-up corrected hardness method was applied. The hardness-shoulders were slightly shifted and it is unclear from the plots in Figure 5.3 (c), (d) whether the 1 dpa W{001} still has two hardness-shoulders after correction or not, since the shallower one might be shifted to a h_{max} that is smaller than the smallest considered h_{max} of about 300 nm after correction. The NI-profiles were not particularly smooth after the correction due to the square function of the correction method. Again, the SSE ¹⁴⁾ seemed to vanish beyond 1000nm as can be seen in Figure 5.3 (d). As Table 5.1 shows, the irradiation hardening of uncorrected results ranges between 1.75 and 3.42 GPa. In both the uncorrected and corrected results by the EMC method, the 1 dpa W{001} exhibits a larger irradiation hardening than the 2 dpa W{001}. It is considered that this fits with the microstructural findings since the defect density in the shallow depth of a few hundred nm is higher in 1 dpa W{001} compared to 2 dpa W{001}, resulting in a larger irradiation hardening. Table 5.1 indicates that generally, the bulk equivalent hardness values obtained by EMC method were about 70 % of the uncorrected results for irradiated W{001} and about 85 % for unirradiated W{001}, and the irradiation hardening by EMC was approximately 40 %, 50 % and 60 % of uncorrected results for 0.1 dpa, 1 dpa and 2 dpa,

respectively. This shows strong influence of pile-up formation on the NI-hardness of ion-irradiated pure {001}W.

The significant pile-up effect on NI-hardness can also be seen when the variation of the term, $H_{IT}/H^{EMC} = A_P^{EMC} / A_P^{ISO} = (E^*/E^{EMC*})^2$ is plotted over h_{max} following the equation (5.5), see Figure 5.4.

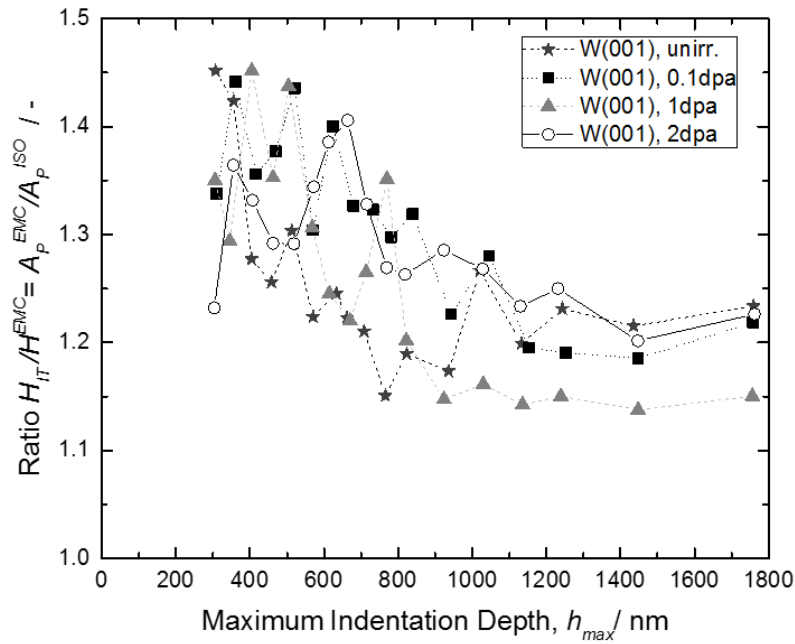


Figure 5.4: Variation of the term $H_{IT}/H^{EMC} = A_P^{EMC} / A_P^{ISO} = (E^*/E^{EMC*})^2$ over h_{max} for unirradiated and irradiated W{001}.

As a reference, the averaged ratio term, C_{EMC} , of Heintze et al. ²¹⁾ is 1.15 ± 0.05 for neutron irradiated T91 and 1.11 and 1.04 for 2.5 dpa and 3.5 dpa ion-irradiated T91, respectively. Recall that they used a single averaged factor C_{EMC} to correct the hardness over the whole h_{max} . However, in this study here they have been calculated individually for every h_{max} and these results show a

high dependence of $H_{IT}/H^{EMC} = A_P^{EMC} / A_P^{ISO} = (E^*/ E^{EMC*})^2$ with h_{max} ranging from 1.45 in shallower h_{max} to 1.15 for deeper h_{max} .

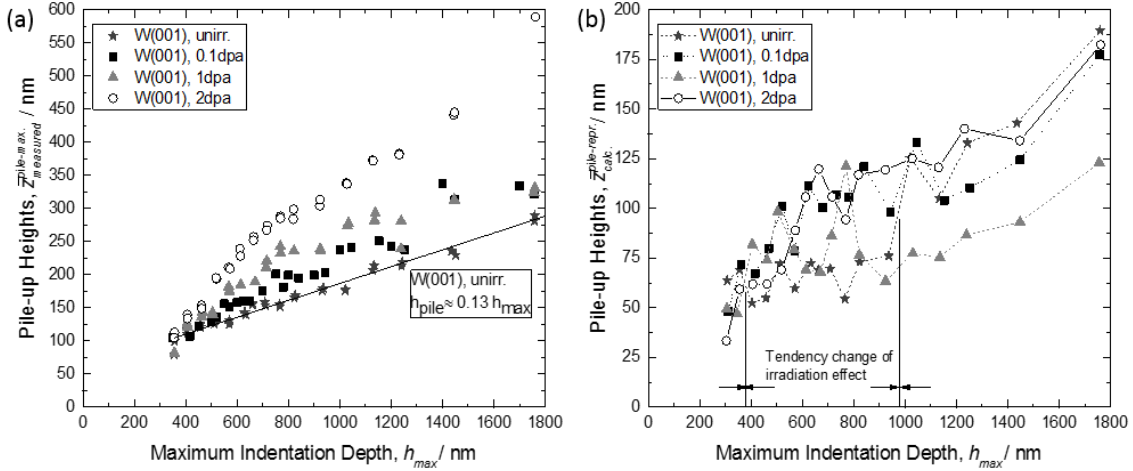


Figure 5.5: (a) Calculated $\bar{z}_{calc.}^{pile-repr.}$ and (b) measured $\bar{z}_{measured}^{pile-max}$ over h_{max} for unirradiated and irradiated W{001}. Note that the 2 dpa W{001} surface was found to be aligned around 5° to the horizontal plane. So we expect actual pile-up measured $\bar{z}_{measured}^{pile-max}$ to be smaller in this specimen.

In Figure 5.5 (a) and 5 (b), $\bar{z}_{measured}^{pile-max}$ and $\bar{z}_{calc.}^{pile-repr.}$ are plotted over h_{max} . The $\bar{z}_{measured}^{pile-max}$ of unirradiated W{001} shows a linear relationship over h_{max} with a slope of 0.13. In Figure 5.5 (a), two results of the measured $\bar{z}_{measured}^{pile-max}$ per indentation depth are shown to point out the small error bar in the AFM analysis. The evolution of $\bar{z}_{measured}^{pile-max}$ of irradiated W{001} is more complex than a linear trend. Generally, irradiation caused an increase of $\bar{z}_{measured}^{pile-max}$ compared to unirradiated W{001} for the same h_{max} and this trend became remarkable with increasing displacement damage. To understand this, one has to look at the 3-dimensional distribution of pile-

up around the indents. As it has been observed in AFM, the volume profile around the indents depended on the irradiation condition. Generally, in the unirradiated specimen, the material pile-up was more broadly distributed and the pile-up height at its maximum was shallower compared to the irradiated specimens. This is in accordance with the work by Hardie et al.²³⁾ on Fe-12wt.%Cr alloy comparing between as-received and self-ion irradiated condition (6.18 dpa at 593 K) using different indenter shapes. For the results using Berkovich tips, their explanation for the higher pile-up heights in the irradiated Fe-12wt.%Cr alloy compared to the unirradiated one was that the plastic zone was suppressed by the ion-irradiated hardened layer, as they showed by TEM observation, and the deformation became more constrained closer to the tip, according to their AFM results. This explanation is reasonable in this case as well.

It should be kept in mind that $\bar{z}_{calc.}^{pile-repr.}$ is an analytical value obtained from A_P^{EMC} that serves as a representative pile-up height, but does not reflect the real pile-up height that is in contact with the indenter. However, the $\bar{z}_{calc.}^{pile-repr.}$ values follow an interesting evolution over h_{max} . As mentioned before, $\bar{z}_{measured}^{pile-max.}$ is higher for irradiated W{001} than for unirradiated W{001} at each h_{max} . This is not the case for $\bar{z}_{calc.}^{pile-repr.}$. Although the data is limited, in h_{max} up to 350 nm, irradiated W{001} shows lower $\bar{z}_{calc.}^{pile-repr.}$ than unirradiated W{001}. Beyond 350 nm up to 1000 nm, there is a turnover of this trend to an increase of $\bar{z}_{calc.}^{pile-repr.}$ by irradiation. Beyond 1000 nm, irradiation again reduces $\bar{z}_{calc.}^{pile-repr.}$ compared to unirradiated W{001}. The turnover at 1000 nm h_{max} may be due to the SSE¹⁴⁾ that vanished at this depth according to Figure 5.3 (d).

Figure 5.6 summarizes the ion-irradiation hardening results, based on the equation (5.10) of this work in comparison with the previously obtained ion-irradiation results by the group⁵⁾ as well as with the neutron-irradiation hardening results by Vickers hardness tests of other researchers^{4, 24, 25)}. The damage levels that are referred to in this figure are averaged damage levels over the projected ion range up to 2000 nm and represent the dpa at a depth of about 600 nm. The bulk-equivalent NI hardness was obtained from the penetration depths from surface to the critical depth

showing no softer substrate effect. Therefore it is considered that such an averaged dpa value is a good representative for connecting H_0 with dpa.

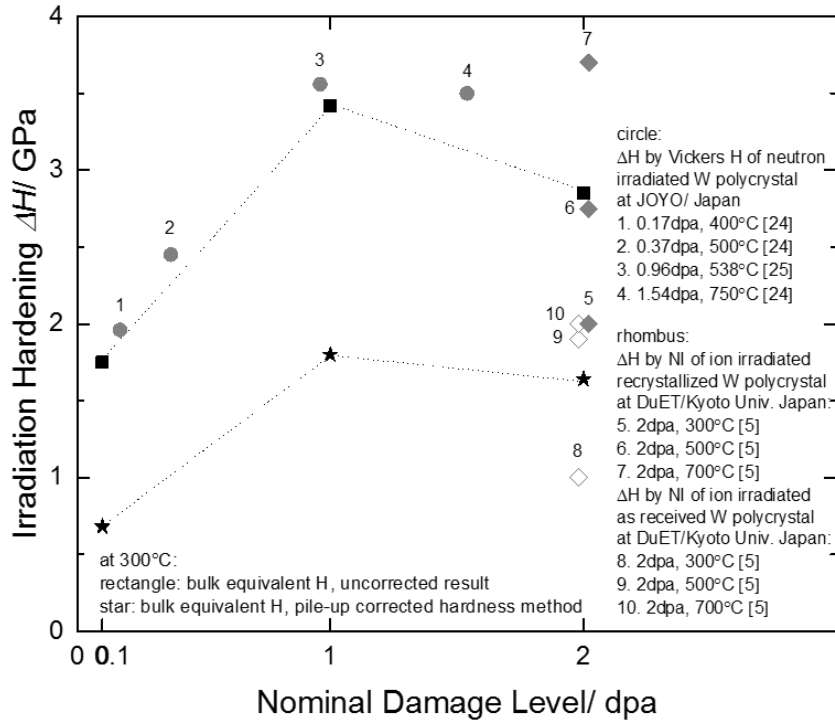


Figure 5.6: Summary of ion-irradiation hardening obtained by NI-hardness measurements in this work and comparison with the previous ion-irradiation results by our group⁵⁾ as well as with the neutron-irradiation hardening results evaluated by Vickers hardness tests by other groups^{4, 24, 25)}.

Zhang et al.⁵⁾ proposed a method to evaluate bulk equivalent hardness of Fe^{3+} irradiated (2 dpa at 573 K, 773 K, 973 K and 1273 K) pure recrystallized and as received W. The method is based on the assumption that the geometrically necessary dislocation density at an indentation

depth is unchanged by ion-irradiation. Their results of ion-irradiation hardening for different irradiation temperatures between 573 K and 973 K are shown in Figure 5.6. By converting this temperature tendency to the results of this work, it appears that the pile-up corrected ion irradiation hardening results based on the EMC method are consistent with the available neutron-irradiation hardening results^{4, 24, 25)} obtained by Vickers hardness tests for higher temperatures, although the displacement rate effect should be considered. Heintze et al.²¹⁾ also reported that the EMC corrected NI hardness of ion-irradiated T91 matched well with the Vickers hardness of the neutron irradiated one²¹⁾, taking account of an irradiation independent elastic modulus of T91.

5.5 Conclusions

NI-hardness measurements on unirradiated and ion-irradiated (0.1 dpa, 1 and 2 dpa at 300 °C) tungsten (W) single crystals of {001} surface orientation were carried out to investigate the ion-irradiation hardening behaviour of pure W with consideration of material pile-up effect using the concepts in the EMC method²¹⁾. The following conclusions can be made:

- 1) The magnitude of material pile-up in W is significant, and therefore should not be neglected in NI-hardness evaluation. The bulk equivalent hardness values obtained by the EMC method were about 70% of the uncorrected results for irradiated W{001} and about 85% for unirradiated W{001}.
- 2) The amount of ion-irradiation hardening estimated by the EMC method was approximately 40 %, 50 % and 60 % of uncorrected ones for specimens irradiated up to 0.1 dpa, 1 dpa and 2 dpa, respectively.
- 3) The measured maximum pile-up height, $\bar{z}_{measured}^{pile-max}$, is higher for irradiated W{001} than for unirradiated W{001} at each h_{max} .

4) An averaged pile-up height associated with the actual area of contact including pile up from EMC hardness, $\bar{Z}_{calc.}^{pile-repr.}$, showed different responses to ion-irradiation depending on h_{max} . In the case of h_{max} up to 350 nm, irradiated W{001} shows a lower $\bar{Z}_{calc.}^{pile-repr.}$ than unirradiated W{001}. Between 350 nm and 1000 nm, there is a turnover of this trend to an increase of $\bar{Z}_{calc.}^{pile-repr.}$ by irradiation. Beyond 1000 nm, irradiation again reduces $\bar{Z}_{calc.}^{pile-repr.}$ compared to unirradiated W{001}.

5.6 Appendix

List of Abbreviations (in alphabetical order)

AFM	Atomic force microscopy.
EBSD	Electron back scatter diffraction.
EMC	Elastic modulus corrected method by Heintze et al. ²¹⁾ .
ISE	Indentation size effect ¹³⁾ .
NI	Nanoindentation.
PUC	Pile-up correction method ²³⁾ .
SEM	Scanning electron microscopy.
SRIM	Stopping range of ions in matter ²⁷⁾ .
SSE	Softer substrate effect ¹⁴⁾ .

List of Symbols (in alphabetical order)

A_P^{EMC}	True projected area of contact including pile-up by EMC method ²¹⁾ .
-------------	---

A_P^{ISO}	Projected contact area according to ISO standards related to NI-testing ²⁸⁾ .
β	Factor accounting for the elastic recovery upon removal of load.
C_{cor}	Correction factor by Beck et al. ²²⁾ .
E^*	Composite modulus of elastic modulus of indenter, E_I , and measured modulus of tested material, E_{IT} .
E^{EMC*}	Composite modulus of the elastic modulus of the indenter, E_I , and the elastic modulus of the material, E_S .
E_I	Elastic modulus of the indenter.
E_{IT}	Measured and apparent modulus of the tested material.
E_S	Elastic modulus of tested specimen.
F_{max}	Maximum force.
H	NI hardness at a certain indentation depth by Nix and Gao ¹³⁾ .
$H/A_{actual}/A_{cc}$	Pile-up corrected hardness using (PUC) method by Hardie et al ²³⁾ .
H_0	Hardness at the limit of infinite depth by Nix and Gao ¹³⁾ .
ΔH	Irradiation hardening.
H^{EMC}	Pile-up height corrected NI hardness based on EMC method ²¹⁾ .
H_{IT}	(Uncorrected) NI hardness according to ISO standards related to NI-testing ²⁸⁾ .
$H_{irr}^{bulkequ}$	Bulk equivalent hardness of irradiated material by Kasada et al ³⁵⁾ .
h^*	Characteristic length ¹³⁾ that depends on the indenter shape, H_0 and the shear modulus for calculating H_0 .

h_c^{ISO}	Contact depth according to ISO standards related to NI-testing ²⁸⁾ .
h_f / h_p	Final displacement after complete unloading according to Bolshakov and Pharr ¹⁶⁾ / Permanent deformation depth in the tested specimen after load removal.
h_{max} / h	Maximum indentation depth from the initial surface by ISO standards related to NI-testing ²⁸⁾ / Indentation depth (maximum) by Nix and Gao ¹³⁾ .
h_r	The intercept of the depth axis with the tangent to the unloading curve.
n	Hardening coefficient.
\dot{P}/P	Ratio of loading rate to load.
S	Contact stiffness considered to be affected by the contact area.
σ	Yield stress.
ν_I	Poisson's ratio of the indenter.
ν_s	Poisson's ratio of the tested material.
$z_{calc.}^{pile-repr.}$	Representative depth including pile-up height, associated with A_P^{EMC} .
$\bar{z}_{calc.}^{pile-repr.}$	Averaged pile-up height, associated with A_P^{EMC} .
$\bar{z}_{measured}^{pile-max}$	Measured pile-up height. Highest pile-up located along a $\langle 111 \rangle$ orientation.

5.7 References

- 1) K. Ezato, S. Suzuki; Y. Seki, K. Mohri, K. Yokoyama, F. Escourbiac, T. Hirai and V. Kuznetsov: *Fus. Eng. Des.* **98-99** (2015) 1281-1284.
- 2) M. Merola, F. Escourbiac, A. R. Raffray, P. Chappuis, T. Hirai, S. Gicquel and I. B. Agcy: *Fus. Eng. Des.* **96-97** (2015) 34-41.
- 3) H. Bolt, V. Barabash, W. Krauss, J. Linke, R. Neu, S. Suzuki, N. Yoshida and A. U. Team: *J. Nucl. Mater.* **329** (2004) 66-73.
- 4) A. Hasegawa, M. Fukuda, T. Tanno and S. Nogami: *Mater. Trans.* **54** (2013) 466-471.
- 5) Z. X. Zhang, E. Hasenhuettl, K. Yabuuchi and A. Kimura: *Nucl. Mater. En.* **9** (2016) 539-546.
- 6) Z. X. Zhang, D. Chen, W. Han and A. Kimura: *Fus. Eng. Des.* **98** (2015) 2103-2107.
- 7) E. Hasenhuettl, R. Kasada, Z. X. Zhang, K. Yabuuchi and A. Kimura: *Mater. Trans.* accepted on 2016.12.28, DOI: 10.2320/matertrans.ML201603.
- 8) D. E. J. Armstrong, A. Wilkinson and S. G. Roberts: *Phys. Scr.* **2011** T145 (2011) 014076.
- 9) D. E. J. Armstrong, P. D. Edmondson and S. G. Roberts: *Appl. Phys. Lett.* **102** (2013) 251901.
- 10) J. S. K. L Gibson, S. G. Roberts and D. E. J. Armstrong: *Mater. Sci. Eng. A* **625** (2015) 380-384.
- 11) W. C. Oliver and G. M. Pharr: *J. Mater. Res.* **7** (1992) 1564-1583.
- 12) A. C. Fischer-Cripps: *Surf. Coat. Technol.* **200** (2006) 4153-4165.
- 13) W. D. Nix and H. Gao: *J. Mechan. Phys. Solids* **46** (1998) 411-425.
- 14) I. Manika and J. Maniks: *J. Phys. D* **41** (2008) p. 074010.
- 15) W. C. Oliver and G. M. Pharr: *J. Mater. Res.* **19** (2004) 3-20.
- 16) A. Bolshakov and G. Pharr: *J. Mater. Res.* **13** (1998) 1049-1058.
- 17) Y.- H. Lee, U. Baek, Y.- I. Kim and S.- H. Nahm: *Mater. Lett.* **61** (2007) 4039-4042.

- 18) Y. Lee, J. Hahn, S. Nahm, J. Jang and D. Kwon: *J. Phys. D* **41** (2008) 074027.
- 19) D. Bahr, D. Kramer and W. Gerberich: *Acta Mater.* **46** (1998) 3605-3617.
- 20) W. Gerberich, J. Nelson, E. Lilleodden, P. Anderson and J. Wyrobek: *Acta Mater.* **44** (1996) 3585-3598.
- 21) C. Heintze, F. Bergner, S. Akhmadaliev and E. Altstadt: *J. Nucl. Mater.* **472** (2016) 196-205.
- 22) C. E. Beck, F. Hofmann, J. K. Eliason, A. A. Maznev, K. A. Nelson and D. E. J. Armstrong: *Scripta Mater.* **128** (2017) 83-86.
- 23) C. D. Hardie, S. G. Roberts, S. G. and A. J. Bushby: *J. Nucl. Mater.* **462** (2015) 391-401.
- 24) T. Tanno, A. Hasegawa, J. C. He, M. Fujiwara, S. Nagomi, M. Satou, T. Shishido and K. Abe: *Mater. Trans.* **48** (2007) 2399-2402.
- 25) T. Tanno, M. Fukuda, S. Nogami and A. Hasegawa: *Mater. Trans.* **52** (2011) 1447-1451.
- 26) A. Kohyama, Y. Katoh, M. Ando and K. Jimbo: *Fus. Eng. Des.* **51-52** (2000) 789-795.
- 27) "INTERACTION OF IONS WITH MATTER" by J.F. Ziegler. <http://www.srim.org/>, (accessed 2016-09-17).
- 28) ISO 14577-1: 2002 Metallic Materials- Instrumented Indentation Test for Hardness and Materials Parameters - Part 1: Test method.
- 29) I. N. Sneddon: *Int. J. Eng. Sci.* **3** (1965) 47-57.
- 30) A. Ternovskii, V. P. Alekhin, M. K. Shorshorov, M. Khrushchev and V. Skvortsov: *Zavodskaya Lab.* **39** (1973) 1242.
- 31) S. I. Bulychev, V. P. Alekhin, M. K. Shorshorov, A. Ternovskii and G. Shnyrev: *Zavodskaya Lab.* **41** (1975) 1137-1140.
- 32) S. I. Bulychev, V. P. Alekhin, M. K. Shorshorov and A. Ternovskii: *Probl. Prochn* **9** (1976) 79-83.
- 33) M. K. Shorshorov; S. I. Bulychev and V. P. Alekhin: *Sov Phys, Dokl.* **26** (1982) 769.
- 34) S. I. Bulychev and V. P. Alekhin: **53** (1987) 1091-1096.

35) R. Kasada, Y. Takayama, K. Yabuuchi and A. Kimura: *Fus. Eng. Des.* **86** (2011) 2658-2661.

Chapter 6:

**Orientation Dependence of Ion-irradiation
Hardening in Pure Tungsten Single Crystal**

6.1 Introduction

Tungsten (W) is regarded as the plasma facing material in fusion power plants. In order to investigate the expected irradiation effects, ion-irradiation is intensively used to study irradiation effects on materials. The existing studies on ion-irradiation effects on W mainly focus on polycrystalline W neglecting grain orientation dependence on the results. Only a few studies consider the crystal orientation in pure W when investigating the ion-irradiation effects, such as in ¹⁻⁵). For example, Liu et al. ⁴) investigated the effect of low flux helium and hydrogen ion irradiation on W polycrystal with large size of grains whose grain orientations were near {011}, {101} and {111} planes on the surface, and found that the helium-induced blistering depends strongly on the grain orientation. The most resistant orientation to surface morphology changes by the irradiations was near {001} plane ⁴).

Generally, the irradiation with several MeV of heavy ions induces the formation of radiation damage structures in the limited zone that is within a few microns from the surface. Grzonka et al. ⁵) carried out self-ion irradiation at room temperature on W polycrystal with an average dose level of 2.3 and 6.36 dpa. They found by TEM observation that the damaged zone inside a [110] grain extended deeper compared to the adjacent [012] grain at 2.3 dpa, while they found no orientation dependence in adjacent grains after irradiation up to 6.36 dpa ⁵). Although they considered that channeling and/or grain boundary effect that is the interaction of dislocation with grain boundaries within the area of damage zone could be the reason for the difference in the detected damage depth ⁵), no clear experimental evidence has been obtained.

It has been reported recently for pure W irradiated to 2 dpa that the distribution of defect structures at 1273 K extended to deeper area than SRIM code calculation result of which the mechanism was attributed for vacancy migration at such a high irradiation temperature ⁶).

The objective here is to investigate the potential effect of crystal orientation on the microstructural change and hardening evolution in ion-irradiated W without considering grain boundary effects.

6.2 Experimental Method

As a starting material, a W single crystal of 99.7% purity was used. From the W single crystal, small specimens with the surface orientations of {001} and {011} were sampled and denoted as W{001} and W{011}, respectively. The exact surface orientation of the specimen was measured by electron backscatter diffraction patterns method. More details on the sample preparation can be found in chapter 4 and chapter 5.

The specimens were irradiated using an accelerator, DuET, at Kyoto University with 6.4 MeV Fe^{3+} ions up to a nominal damage level of 1 dpa at 573 K. The SRIM code ⁷⁾ results are shown in Fig. 6.1. The nominal dpa is defined as the displacement damage occurring at the depth of 600 nm and the threshold energy of W is selected to be 90 eV. As shown in Fig. 6.1, the ion-irradiation induced damaged zone reaches up to 1800 nm.

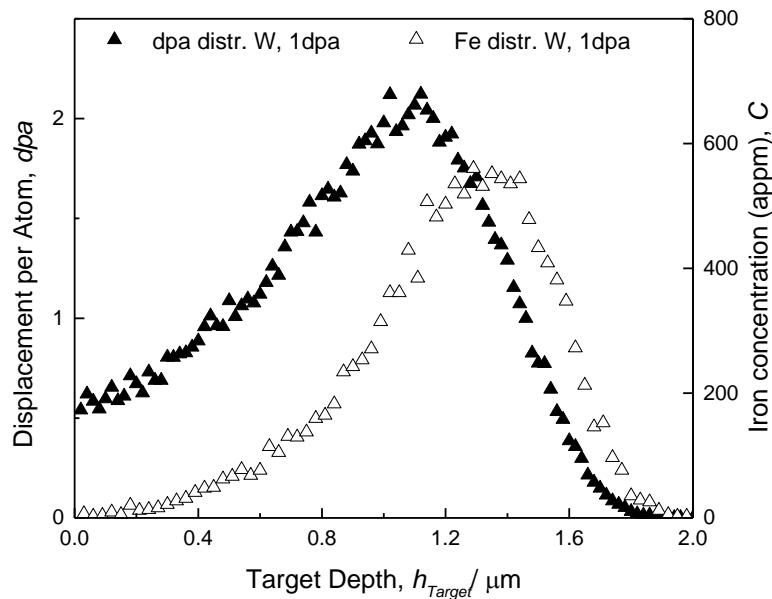


Figure 6.1: Damage and iron distribution in 1 dpa irradiated W.

After preparation of thin foils by focused ion beam apparatus (HITACHI FB2200) and flashing electrolytic polishing, TEM microstructures were examined by JEOL JEM-2010 at 200 kV.

The hardness was measured by a nanoindenter (Agilent Technologies Inc. Model NanoIndenter G200) using a Berkovich tip before and after ion-irradiation. The indenter has been positioned in a way that one edge of the Berkovich triangle was perpendicular to a $\langle 111 \rangle$ orientation. Constant strain rate (CSR) test method including continuous stiffness method (CSM)⁸⁾ was adopted, which allows a continuous detection of hardness H and indentation modulus E_{IT} over indentation depth h and is suitable to obtain a whole $H-h$ profile. The testing conditions were as follows: the maximum contact depth was 2000 nm, the nominal strain rate was 0.05 s^{-1} , the oscillation amplitude was 1 nm and the testing temperature was $(299 \pm 2) \text{ K}$. For each testing condition, 10 tests were carried out within an uncertainty of $\pm 0.2 \text{ GPa}$.

6.3 Results and Discussions

In Fig. 6.2, the TEM microstructures of irradiated a) $W\{001\}$ and b) $W\{011\}$ single crystals are shown. The radiation damaged zone appears to be a bit deeper than the prediction by SRIM code in both orientations. It should be noticed that a slight crystal orientation dependence of the final damaged depth is visible: $W\{001\}$ shows 2400 nm compared to 2200 nm in $W\{011\}$. In both specimens, a double black band structure with a high number density of loop rafts was observed. The upper boundary of the shallower black band is located at around the same depth, 700 nm, in both specimens. The upper and lower boundaries of the two black bands are marked by white lines in Figure 6.2. As for the type of defects, both orientations show dislocation loop clusters, mostly formed to rafts, as the major defect type.

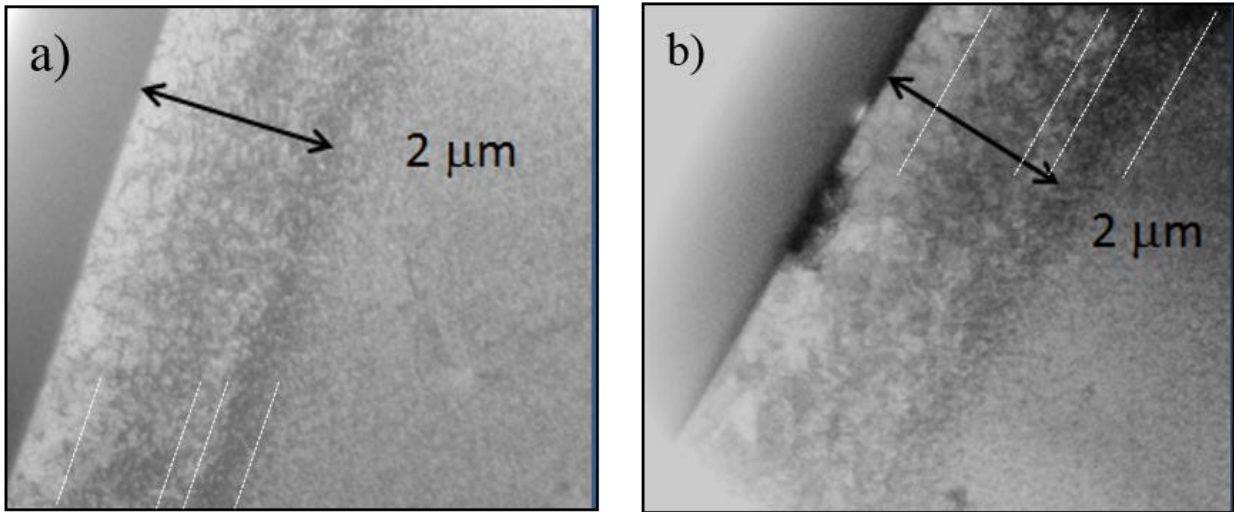


Figure 6.2: TEM microstructural overview of a) $W\{011\}$ and b) $W\{001\}$.

Fig. 6.3 shows the $H-h$ profiles for CSR tests of unirradiated and irradiated specimens, indicating an unexpected significant difference between the profiles of irradiated $W\{001\}$ and $W\{011\}$, in contrast to the results in TEM microstructural observation which showed rather small difference in damage depth. The characteristic hardness shoulders at the depth $h_{crit}^{9,10}$ are observed in both of the profiles. The so called critical indentation depth h_{crit} is larger in the case of $W\{001\}$ than in the case of $W\{011\}$: around 500 nm and 400 nm, respectively. But generally, both orientations show a high irradiation hardening behaviour by 1dpa irradiation at 573 K.

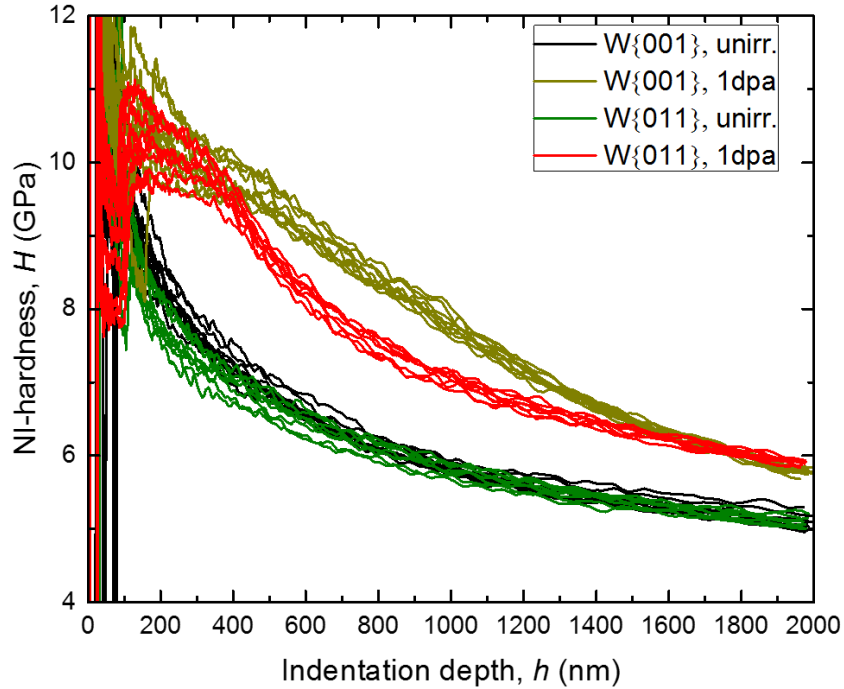


Figure 6.3: NI-hardness – indentation depth ($H - h$) profiles of unirradiated and 1 dpa irradiated $W\{001\}$ and $W\{011\}$.

According to Kasada et al.⁹⁾ for ion-irradiated materials and originally denoted by Manika et al.¹⁰⁾ for film on substrate systems, the hardness shoulder depth, h_{crit} , is defined as the indentation depth where the NI hardness start to reflect the hardness of the unirradiated region below the irradiated one. For example in Fe-1wt.%Cu and Fe-1.4wt.%Mn, Fe^{3+} irradiated up to 1 dpa at 563 K, the hardness shoulder was at around 500 nm and 300nm of indentation depth, respectively⁹⁾. In polycrystalline pure W Fe^{3+} irradiated to 2 dpa at 573 K to 1273 K the hardness shoulder was at around 300-350 nm¹¹⁾. In the previous material pile-up formation study described in chapter 5 including basic hardness testing method according to ISO standards¹²⁾ on unirradiated and irradiated $W\{001\}$, a hardness shoulder for 1 dpa $W\{001\}$ at around 400-500 nm and a

possible existence of a deeper one somewhere between 650-950 nm was observed. The statement was vague because of the used testing procedure of basic hardness method, which serves a rather scattered $H-h$ profile. In this study here, by using CSR testing method, which allows a continuous measurement of hardness over indentation depth by a single indentation, and subsequently by analyzing the $H-h$ profile of irradiated W{001} and irradiated W{011} by Nix and Gao's¹³⁾ interpretation of the depth dependence of hardness, i.e. by a H^2-l/h profile, it can be confirmed that irradiated W{001} shows a second hardness shoulder at an indentation depth of around 1000 nm. The exact reason is still unclear, but may be attributed to the deeper black band.

A double black band structure can be interpreted on the bases of SRIM code calculation results indicating two different depth profiles of lattice damage structures and implanted Fe³⁺ ions. The shallower black bands may consist of lattice damage structures such as self-interstitial loops and/or vacancy clusters, while the deeper one may consists of Fe interstitial loops.

As for the orientation dependence of the NI hardness profile, the mechanism is not clear. Since the TEM microstructure appears to be independent of crystal orientation, it is difficult to explain the orientation dependence in terms of the difference in the damaged depth in each single crystal visible by TEM observation. A possible interpretation of the crystal orientation dependence can be addressed to the 1D motion of very fine interstitial loops which are invisible by TEM but effective for the hardening. The longer distance of the 1D motion of interstitial loops in W{001} than in W{011} is considered to be due to the difference in the geometrical orientation of the direction of the 1D motion along the direction parallel to the Burger's vector, \mathbf{b} , of the loops. According to Arakawa et al.¹⁴⁾, the mobile loops by thermal diffusion are those almost parallel to the surfaces of which the \mathbf{b} is $1/2[1-11]$ and $1/2[11-1]$ when the surfaces of the TEM thin foils were set at almost (011).

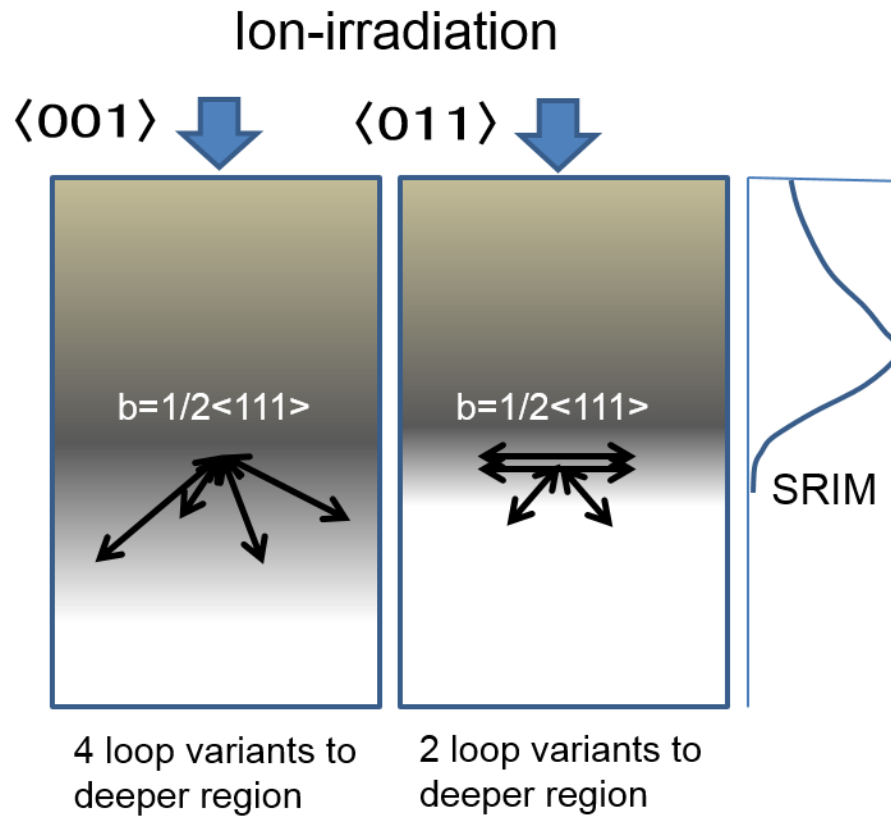


Figure 6.4: A possible interpretation of hardness profiles of $W\{001\}$ and $W\{011\}$. 1D motion (arrows in the figure) of very fine dislocation loops with $b = 1/2 \langle 111 \rangle$ which are invisible by TEM but effective for hardening.

As shown in Fig. 6.4, in the case of ion-irradiation on $W(011)$, the penetration depth of loops beyond SRIM code calculation can't be possible for 2 variants of $1/2 \langle 111 \rangle$. However, in the case of $W\{001\}$, the mobile loops can be 4 variants which have a \mathbf{b} of $1/2[111]$, $1/2[-111]$, $1/2[1-11]$ or $1/2[11-1]$, where the force applied onto these loops along their direction of motion from the surfaces is rather small. Here, the penetration depth of the 1D motion of dislocation loops becomes

deeper than the SRIM code calculation results showing 2 times more dislocation loops in deeper region in W{001} than in W{011}.

6.4 Conclusions

In order to investigate the effect of crystal surface orientation on the irradiation hardening of pure W, single crystals of W{001} and W{011} were irradiated with 6.4 MeV Fe³⁺ ions up to 1 dpa at 573 K. The TEM examinations revealed that there is a small orientation dependence in the radiation damaged structure, showing that 1 dpa W{001} exhibits deeper damaged structure and that both 1 dpa W{001} and 1 dpa W{011} exhibited a double black band structure with high number density of dislocation loop rafts in the black bands. Even though the change in the damaged depth between the different orientations of single crystals was rather small, the ion-irradiation hardening behaviour evaluated by NI technique turned out to be clearly orientation dependent, namely, W{001} showed a deeper NI hardness profile than W{011}.

6.5 References

- 1) X. Yi, M.L. Jenkins, K. Hattar, P.D. Edmondson and S.G. Roberts: *Acta Mater.* **92** (2015) 163-177.
- 2) X. Yi, M.L. Jenkins, M.A. Kirk, Z. Zhou and S.G. Roberts: *Acta Mater.* **112** (2016) 105-120.
- 3) S. Kajita, N. Yoshida, N. Ohno, Y. Hirahata and R. Yoshihara: *Phys. Scripta* **89** (2) (2014).
- 4) F. Liu, H. Ren, S. Peng and K. Zhu: *Nucl. Instrum. Methods Phys. Res. B* **333** (2014) 120-123.
- 5) J. Grzonka, L. Ciupinski, J. Smalc-Koziorowska, O.V. Ogorodnikova, M. Mayer and K.J. Kurzydowski: *Nucl. Instrum. Methods Phys. Res. B* **340** (2014) 27-33.
- 6) Z.X. Zhang, K. Yabuuchi and A. Kimura: *J. Nucl. Mater.* **480** (2016) 207-215.
- 7) "INTERACTION OF IONS WITH MATTER" by J.F. Ziegler. <http://www.srim.org/>, (accessed 2016-09-17).
- 8) W. C. Oliver and G. M. Pharr: *J. Mater. Res.* **7** (1992) 1564-1583.
- 9) R. Kasada, Y. Takayama, K. Yabuuchi and A. Kimura: *Fus. Eng. Des.* **86** (9-11) (2011) 2658-2661.
- 10) I. Manika and J. Maniks: *J. Phys. D-Appl. Phys.* **41** (7) (2008).
- 11) Z. X. Zhang, E. Hasenhuettl, K. Yabuuchi and A. Kimura: *Nucl. Mater. En.* **9** (2016) 539-546.
- 12) ISO 14577-1: 2002 Metallic Materials- Instrumented Indentation Test for Hardness and Materials Parameters - Part 1: Test method.
- 13) W. D. Nix and H. Gao: *J. Mech. Phys. Sol.* **46** (1998) 411-425.
- 14) K. Arakawa, K. Ono, M. Isshiki, K. Mimura, M. Uchikoshi and H. Mori: *Science* **318** (2007) 956-959.

Chapter 7:

**Orientation Dependence of Radiation Effect in
Ion-irradiated W Single Crystals up to Different
Damage Levels**

7.1 Introduction

In the previous study in chapter 6, the ion-irradiation effects on hardening and microstructure of 1 dpa irradiated W single crystals ¹⁾ were discussed, where the TEM examination revealed that there is no significant orientation dependence in the radiation damaged structure, while the depth profile of ion-irradiation hardening evaluated by nanoindentation technique turned out to be clearly orientation dependent.

Grzonka et al. ²⁾ pointed out an important discussion that the ion-irradiation affected zone could depend on the orientation of the irradiated grain with respect to the ion beam direction. Their transmission electron microscopy (TEM) observations showed slight changes in the ion-irradiation affected zone, where the zone depth in a $\langle 110 \rangle$ grain was slightly deeper compared to that of the adjacent $\langle 012 \rangle$ grain for 2.3 dpa self-ion irradiation at room temperature ²⁾. Also, the zone size at a higher irradiation condition of 6.4 dpa showed a slight increase compared to the case at 2.3 dpa, but no grain dependent analyses was given further in their work ²⁾. They considered that channeling and/or the interaction of dislocation with grain boundaries within the area of damage zone could be the reason for the difference in the detected damage depth ²⁾, but no clear experimental evidence was reported.

No clear mechanism was provided in the previous study discussed in chapter 6, where a rather small amount of radiation displacement, 1 dpa, was given, and systematic analysis of the crystal orientation dependence as well as damage level dependence of irradiation effects in W is necessary by using single crystal W irradiated to various dpa levels.

In the study of this chapter, the effect of displacement damage level on the ion-irradiation affected zone evolution in W single crystals are investigated to understand the crystal orientation effect on the ion-irradiation effects on W. Further on, bulk equivalent hardness is obtained for the specimens discussed in the previous chapter – 1 dpa – as well as for the specimens discussed in this chapter – 0.1 dpa and 2 dpa.

7.2 Experimental Method

The initial material was a W single crystal of 99.7% purity. From that material, small samples with the surface orientations of (001) and (011) were cut and denoted as W{001} and W{011}, respectively. The exact surface orientation of the specimens was measured by electron backscatter diffraction patterns method. The specimen preparation procedure is the same as described in chapter 4 and chapter 5.

All samples were irradiated using a tandetron accelerator, DuET, at Kyoto University with 6.4 MeV Fe^{3+} ions up to a nominal damage level of 0.1 and 2 dpa at 573 K. The depth profile of the ion-irradiation induced displacement damage is calculated by SRIM code³⁾. The damage- and iron distributions for the various damage levels are given in Figure 7.1.

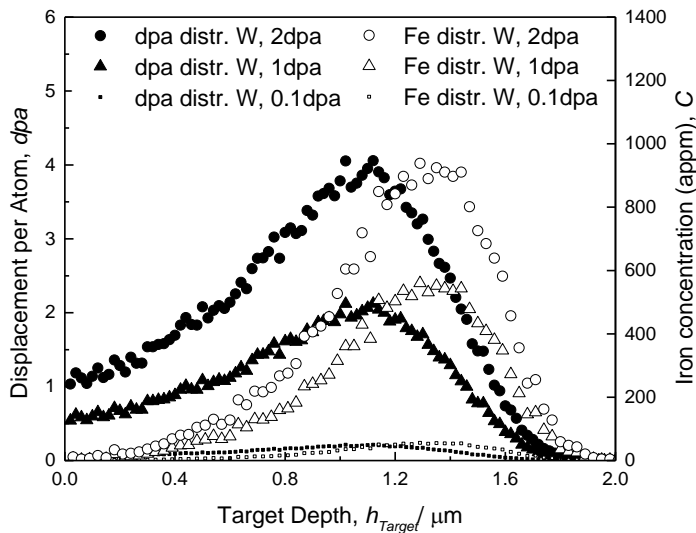


Figure 7.1: Damage and iron distribution in W single crystal of nominal 0.1, 1 and 2 dpa.

The nominal dpa is defined as the displacement damage occurring at the depth of 600 nm and the threshold energy is set to be 90 eV. As shown in Figure 7.1, according to the results of SRIM code,

the ion-irradiation induced damaged zone reaches up to 1800 nm target depth h_{target} and doesn't depend on the damage level.

In the next experimental step, thin foils were cut by focused ion beam facility (HITACHI FB2200) and flashing electrolytic polishing was carried out. TEM microstructure observation was performed with JEOL JEM-2010 at 200 kV.

The hardness of the samples before and after ion-irradiation was measured by nanoindentation (NI) technique (Agilent Technologies Inc. Model NanoIndenter G200) using a Berkovich tip. NI-hardness testing technique was performed in the same testing conditions as described in chapter 6.

7.3 Results and Discussions

7.3.1 NI-hardness

7.3.1.1 Hardness Profiles

Figure 7.2 (a), 7.3 (a) and 7.4 (a) show the $H-h$ profiles for CSR tests of unirradiated and irradiated specimens of different damage levels ranging from 0.1 to 2 dpa. As it has been reported in the previous Chapter 6 for the 1 dpa conditions, the hardness-depth shoulder position $h_{crit}^{4,5}$ – transition point where the unirradiated substrate starts to plastically deform - is orientation dependent with a deeper shoulder in $W\{001\}$ compared to $W\{011\}$, it is now also observed that the hardness shoulder position increases slightly with damage level in both orientations even after the irradiation up to both only 0.1 dpa and a higher of 2 dpa. Generally, it is found that the shape of the NI-hardness profile is characteristic in both orientations and qualitatively unchanged by increasing damage level. Also it can be concluded that the NI hardness is more sensitive to crystal orientation than to the damage level, since the $H-h$ profiles only slightly pronounce by increasing the damage level from 0.1 dpa to 2 dpa.

The shape of the 2 dpa W{011} h - H profile is similar to the h - H profile reported for 2 dpa polycrystalline W irradiated at the same temperature 573 K by Zhang et al. ⁶⁾. Contrary, in 2 dpa W{001}, the much deeper ion-irradiation affected zone is reflected in the h - H profile by a much deeper reaching hardening profile compared to all other h - H profiles. In the unirradiated condition, W{001} shows higher hardness values up to 800 nm indentation depth as W{011} and beyond both h - H profiles follows the same trend.

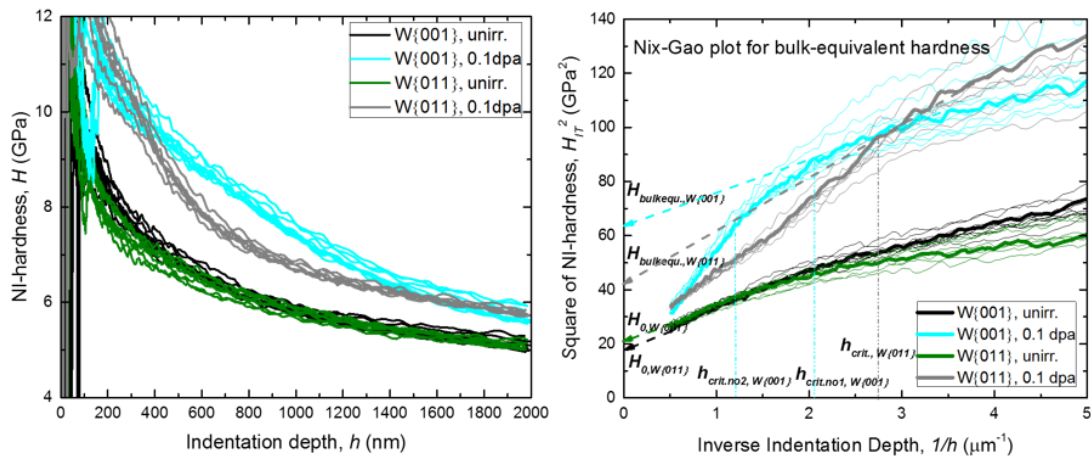


Figure 7.2: (a) H - h profile and (b) H^2 - $1/h$ profile ³⁾ of unirradiated and 0.1 dpa irradiated W{001} and W{011}.

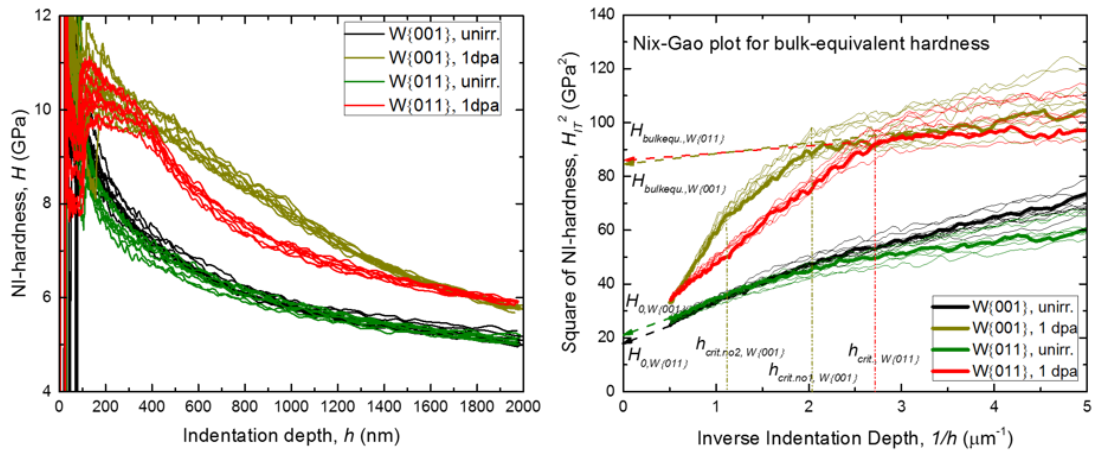


Figure 7.3: (a) H - h profile and (b) H^2 - $1/h$ profile³⁾ of unirradiated and 1dpa irradiated $W\{001\}$ and $W\{011\}$.

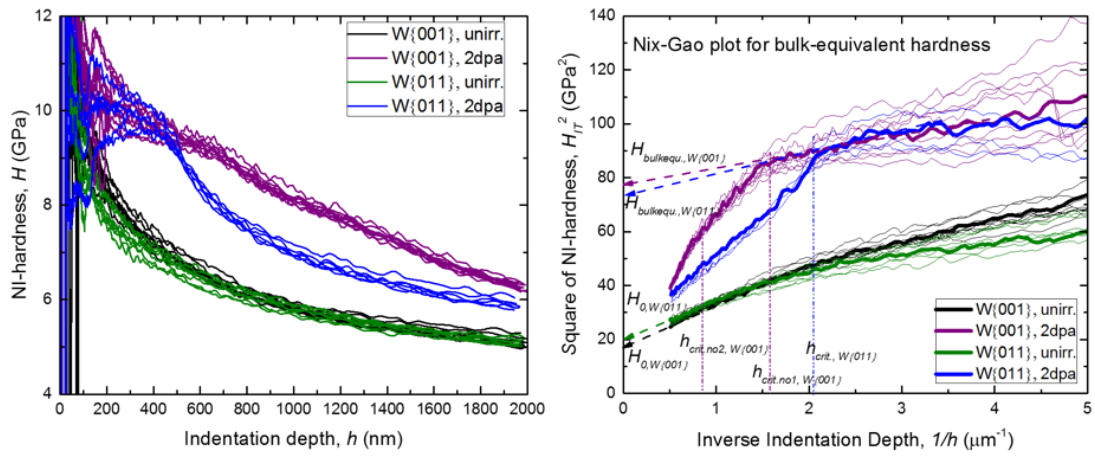


Figure 7.4: (a) H - h profile and (b) H^2 - $1/h$ profile³⁾ of unirradiated and 2dpa irradiated $W\{001\}$ and $W\{011\}$.

7.3.1.2 Bulk Equivalent Hardness

Nix and Gao interpretation ⁷⁾ of the depth dependence of hardness is shown in Figure 7.2 (b), 7.3 (b) and 7.4 (b) to obtain bulk equivalent hardness by following the Nix and Gao method ⁷⁾ as well as Kasada et al. method ⁴⁾. By these H^2-1/h profile, the characteristic hardness shoulders at the so called critical indentation depth h_{crit} ^{4,5)} are observed in both of the profiles. h_{crit} is larger in the case of W{001} than in the case of W{011} for each damage level and h_{crit} increases in both orientations with increasing damage level. Interestingly, 1 dpa and 2 dpa W{001} show an additional hardness shoulder at deeper indentation depth, the shallower around 600 nm and the deeper one around 1000 nm. The reason could be attributed to the two black bands in these irradiation conditions. However, this is not found in the 1 dpa and 2 dpa W{011}, probably because of the fact, that the hardness shoulder is already in such shallow indentation depth that two shoulder points are not distinguishable in the $h-H$ profiles. Also the NI-hardness before the hardness shoulder in 1 dpa W{001} is higher than in 2 dpa W{001}, indicating a higher irradiation defect density in shallow depth in 1 dpa condition, which confirms the trend that the defect formation tendency is to deeper bulk material with increasing damage level. The h_{crit} values together with the irradiation hardening and bulk equivalent hardness values are summarized in Table 6.1.

	W{001}			W{011}				
		0.1 dpa	1 dpa	2 dpa	unirr.	0.1 dpa	1 dpa	2 dpa
$H_{bulkequiv.}$ [GPa]	4.2	8.0	8.7	9.3	4.5	6.6	8.8	9.2
ΔH [GPa]		3.8	4.5	5.1		2.1	4.3	4.7
$h_{crit.no1}$ [nm]		480	480	630		360	380	480
$h_{crit.no2}$ [nm]		830	1000	1300		no	no	no

Table 7.1: Summary of bulk equivalent hardness, irradiation hardening and h_{crit} .

As Figure 7.5 shows, the irradiation hardening obtained by Nix and Gao method ⁷⁾ and Kasada et al. method ⁴⁾ is already high in the 0.1 dpa condition. Only in 0.1 dpa irradiation condition, the irradiation hardening differs between the two different orientations. Saturation of hardening seems to occur already at 1 dpa irradiation condition.

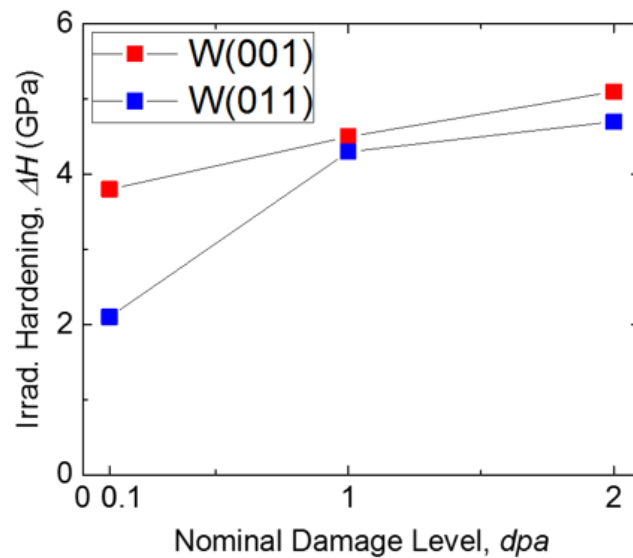


Figure 7.5: Irradiation hardening as a function of nominal damage level.

7.3.2 Microstructural Examinations

7.3.2.1 Lower Displacement Damage (0.1 dpa)

The microstructural overviews of 0.1 dpa W{001} and 0.1 dpa W{011} are shown in Figure 7.6. The irradiation induced damaged zone depth is about 1800 nm which matches well with SRIM code predictions in Figure 7.1. At the displacement damage of 0.1 dpa, the damaged zone depth is independent of crystal orientation. The major defect types in both orientations are dislocation loops, but as shown in Figure 7.7, the dislocation loops in 0.1 dpa W{011} were mostly merged to loop rafts in the entire ion-irradiation affected zone, whereas in 0.1 dpa W{001} most

of the loops were isolated and interacting with line dislocations instead. In both orientations, at the end of the ion-irradiation affected zone, a high defect density band was observed with a width of around 300 nm. Also in both orientations, another high defect density band appeared to be formed just beneath the irradiated surface with a broader width in 0.1 dpa $W\{001\}$ than in 0.1 dpa $W\{011\}$.

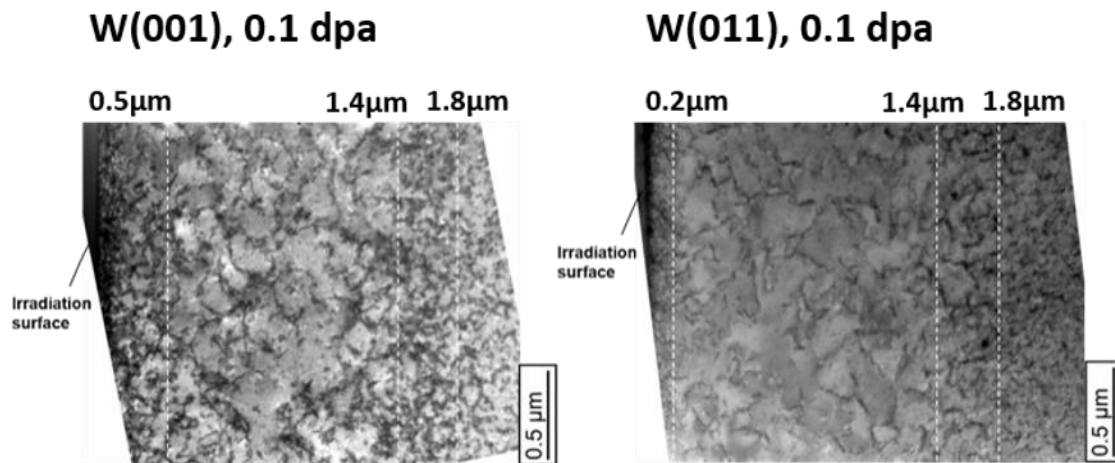


Figure 7.6: Microstructural overview of 0.1 dpa irradiated $W\{001\}$ and $W\{011\}$. The depth of deeper ion-irradiation affected zone is very similar in both orientations.

Yi et al. ^{8,9)} reported that the ion-irradiation induced loop strings and loop rafts in $\langle 001 \rangle$ W grains were only formed when the temperature was above 773 K or the damage level was above 1.2 dpa. In non $\langle 001 \rangle$ W grains, the loop strings were formed already at 573 K in all tested material conditions. Yi et al. ^{8,9)} attributed the grain orientation dependence to the preferential loss of loop variants to the irradiation surface ^{8,9)}, where the probability of loop loss through glide in $\langle 001 \rangle$ grains is equal for all variants of $\frac{1}{2} \langle 111 \rangle$ loops. So in their opinion the presence of the nearby free surface would seem to favour the formation of loop string in non $\langle 001 \rangle$ grains and lower the critical irradiation temperature and irradiation dose limit for formation of loop strings ^{8,9)}.

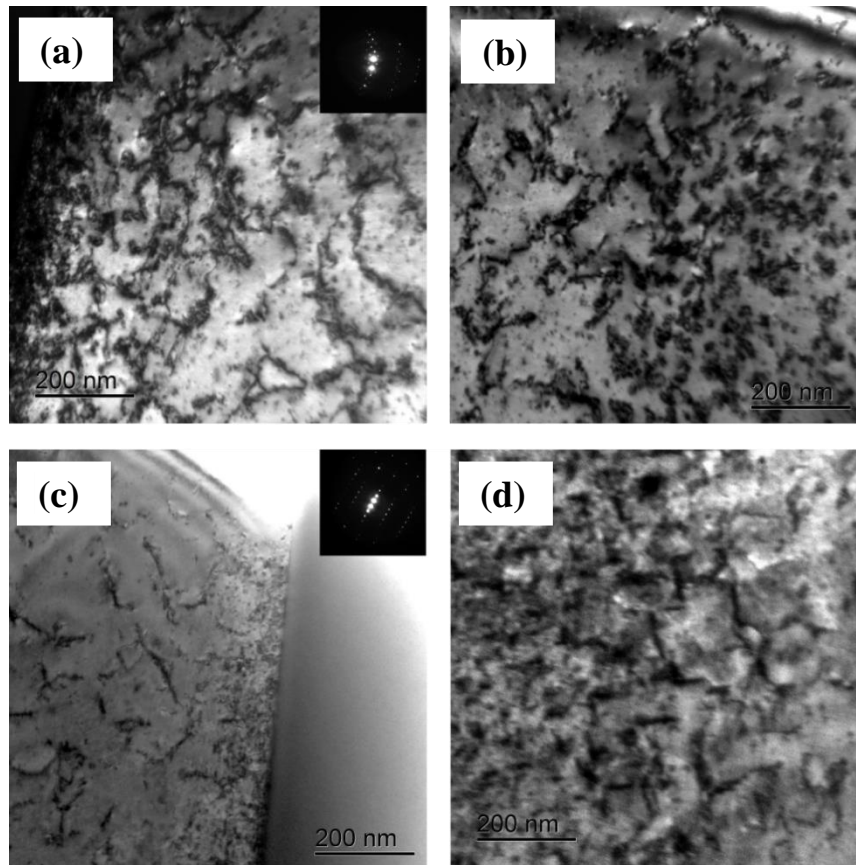


Figure 7.7: Microstructural overview of 0.1 dpa W{001}: (a) Irradiation surface detail; (b) black band detail. Microstructural overview of 0.1 dpa W{011}: (c) Irradiation surface detail; (d) black band detail.

Yi et al.'s^{8,9)} proposed mechanism could explain our orientation dependent defect formation in 0.1 dpa irradiation condition. However, in the case of W{001} specimen of this study, also a high density of line dislocations in the irradiated zone was observed already at 0.1 dpa and 573 K irradiation temperature, see Figure 7.7 (a)-(b).

7.3.2.2 Higher Displacement Damage (2 dpa)

Recall that in the previous TEM study on 1 dpa W{001} and 1 dpa W{011} irradiated at 573 K in Chapter 6, the microstructural overview showed a double black band structure consisting mainly of dislocation loop rafts. Almost no orientation dependence was recognized in the microstructural observation in the case of 1 dpa condition.

Interestingly, a significantly different orientation dependence was found in the case of irradiation up to 2 dpa. This is the most of interesting feature in this study and the microstructural overview is presented in Figure 7.8. The ion-irradiation induced damaged zone in 2 dpa W{001} is remarkably extended to deeper region than that in 2 dpa W{011} indicating strong orientation dependence. The notice is that the damaged zone in 2 dpa W{001} is spreading to 3100 nm depth, which is far beyond the SRIM code calculation results, see Figure 7.1. On the other hand, the zone size in 2 dpa W{011} is similar to the SRIM results indicating that the damaged zone is spreading to only 1900 nm, which is further on similar to 2 dpa irradiated polycrystalline W at the same temperature 573 K ⁶⁾, where the deeper ion-irradiation affected zone reaches up to around 2000 nm ⁶⁾.

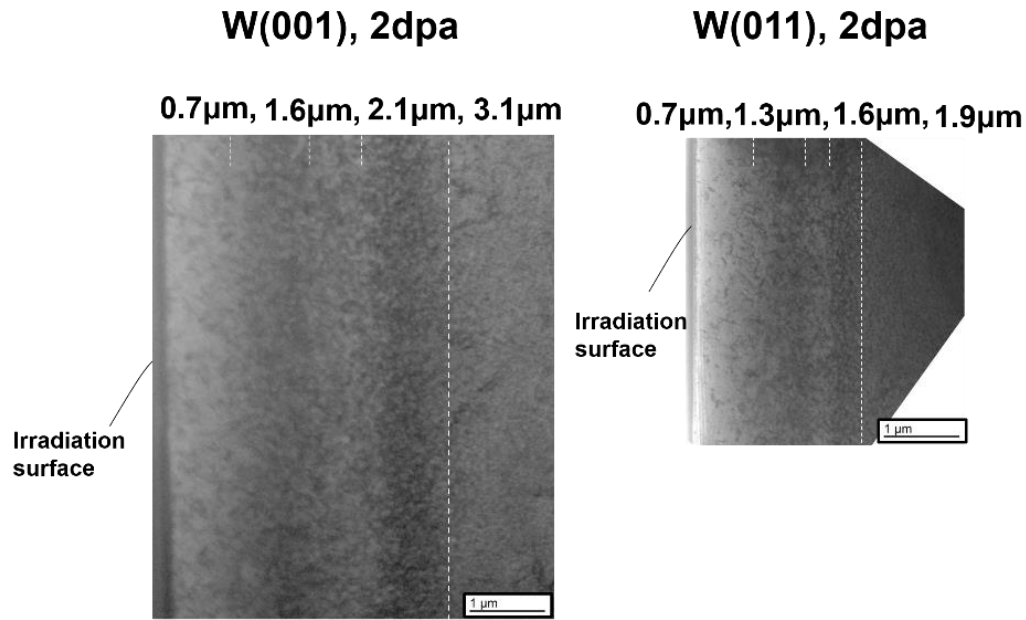


Figure 7.8: Microstructure overview of 2 dpa irradiated $W\{001\}$ and $W\{011\}$. Both orientations show two high defect density bands, mostly consisting of dislocation loop rafts. The position of deeper ion-irradiation affected zone is much deeper in $W\{001\}$.

As clearly shown in Figure 7.8, a double black band structure was also observed in both W single crystals after 2 dpa irradiation, where the black bands mainly consisted of dislocation loop rafts irrespective of the crystal orientation. As shown in Figure 7.9, the detailed microstructural examinations of the deeper high defect density band revealed that in both W single crystals, an ordered network of loop rafts along $\langle 111 \rangle$ is formed and its upper and lower boundary is clearly distinguishable from the lower defect density region, as indicated in Figure 7.10 (a) for 2 dpa $W\{001\}$. Figure 7.10 (b) shows that the black band also consists of more complex agglomerations of dislocation loops, such as disk shaped chains of loops.

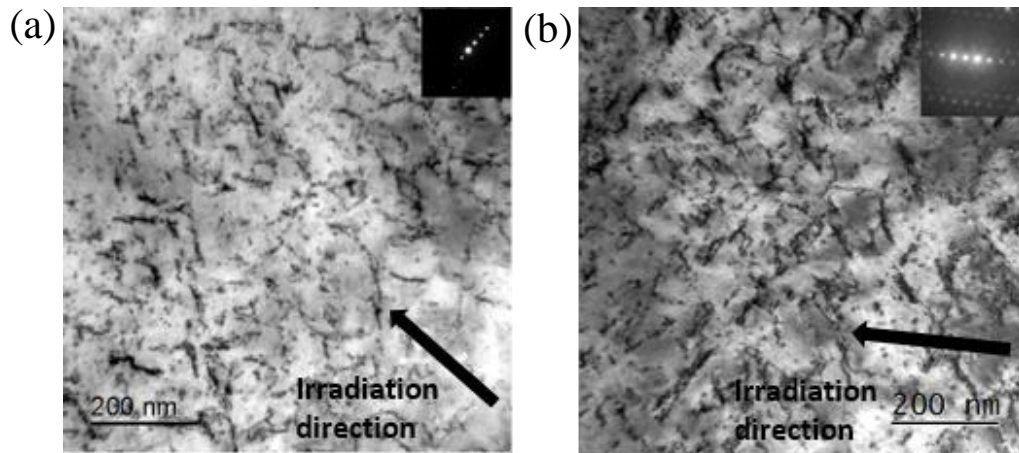


Figure 7.9: Microstructural detail of the deeper black band consisting of an ordered network of loop rafts in (a) 2 dpa $W\{001\}$ and (b) 2 dpa $W\{001\}$.

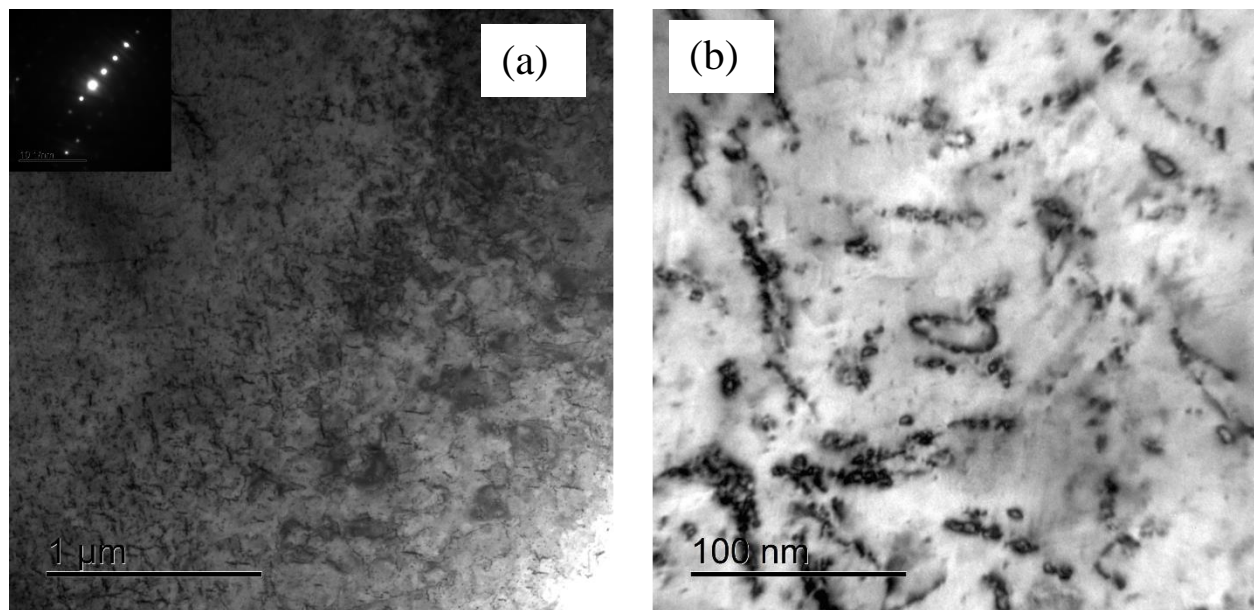


Figure 7.10: (a) Overview of high defect density and intermediate region and (b) disc shape like chains of loop rafts in high defect density region in 2 dpa $W\{001\}$.

Since TEM examinations suggested the occurrence of migration of interstitial dislocation loops that is so called 1D-motion of the dislocation loops, in-situ observation of the 1D-motion of the loop was carried out. The TEM specimen with surface orientation of $\langle 001 \rangle$ was prepared and observed at RT at 200 kV. Figure 7.11 shows a 1-D motion in 2 dpa W{001} by the summary of microstructural images of *in situ* post irradiation TEM observation of a stable loop and a loop that undergoes 1-D motion along $\langle 111 \rangle$, respectively. The right hand figures are the continuous series of photos which were taken at each 0.25 s for a record time of 5s. The top figure indicates that the black dot like structure, namely, interstitial loop, shows a kind of vibration motion of short distance. It is considered that the 1D-motion of rather large size of black dot could be observed in the specimen.

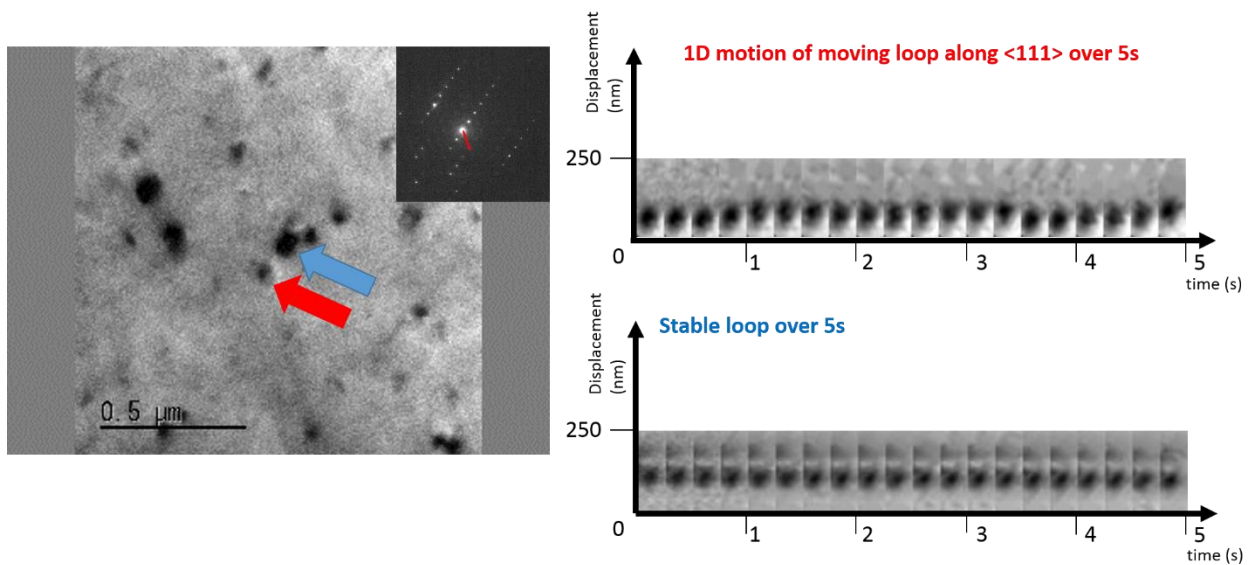


Figure 7.11: *in situ* TEM observation of 1D motion of loop observed in 2 dpa W{001}.

7.3.2.3 Summary of Damage Level Dependence of High Defect Density Zones

Figure 7.12 (a)-(f) summarizes the ion-irradiation affected zone sizes discussed in chapter 6 and chapter 7 and it can be seen that the zone size depends on damage level and orientation.

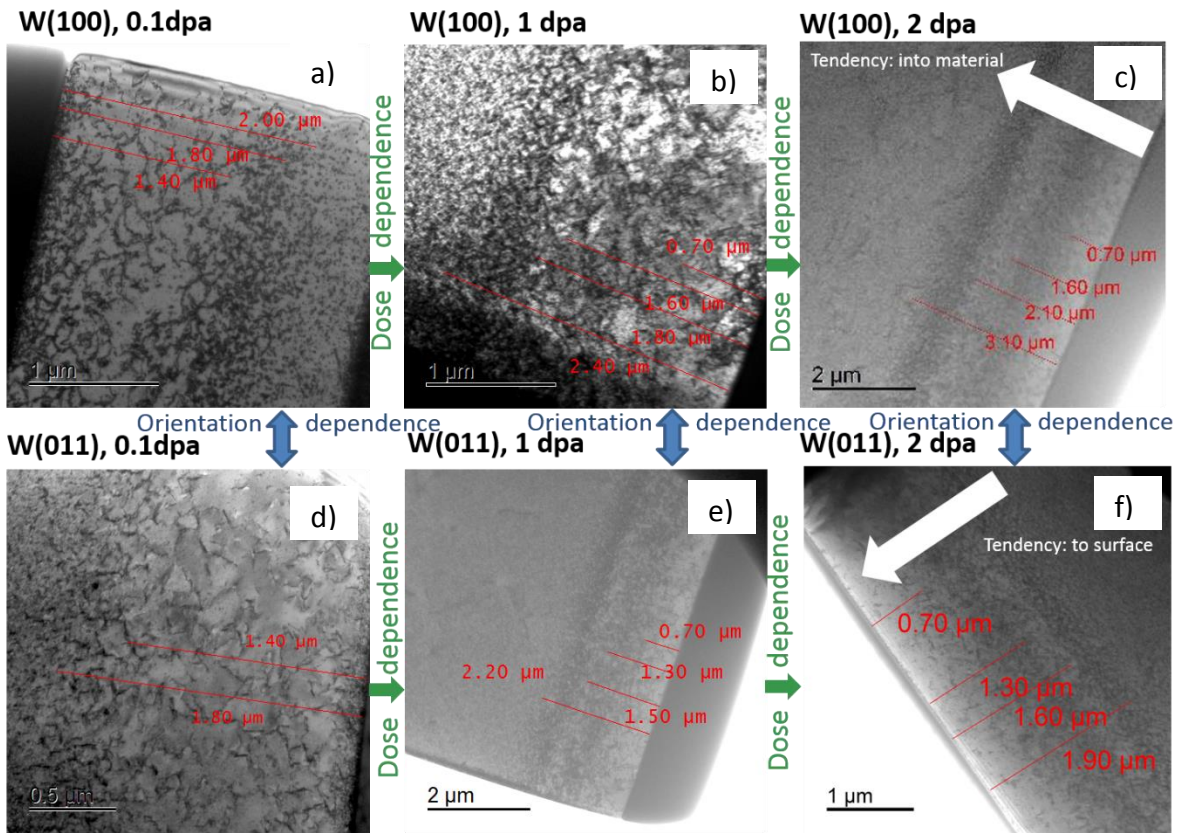


Figure 7.12: Summary of ion-irradiation damaged zone as a function of crystal orientation and damage level.

Interpreting the position and width of the two high defect density bands in 1 dpa and 2 dpa condition of both orientations from Figure (b),(c) and Figure (e),(f) means that the irradiation

defects in $W\{001\}$ tend to be formed deeper in bulk material with increasing damage level and contrary tend to be formed closer to the irradiation surface in $W\{011\}$.

7.3.3 Orientation Dependence of High Defect Density Zones

In the previous study in chapter 6, it was considered that the 1D motion of very fine interstitial loops are invisible by TEM but effective for the irradiation hardening. The longer distance of the 1D motion of interstitial loops in $W\{001\}$ than in $W\{011\}$ is considered to be due to the difference in the geometrical orientation of the direction of the 1D motion along the direction parallel to the Burger's vector, \mathbf{b} , of the loops. Also here in the 2 dpa condition, it is considered that this big difference in ion-irradiation affected zone in 2dpa $W\{001\}$ compared to 2 dpa $W\{011\}$ is caused by 1-D motion of dislocation loops. It is considered that at high dpa, like 2 dpa, the interstitial loops can grow to the enough size to be visible with still high mobility, and the TEM images are now indicating a remarkable difference in the range of the irradiation affected defect zone between the two orientations.

7.4 Conclusions

Pure tungsten (W) single crystals of $\{001\}$ and $\{011\}$ surface orientations were irradiated with 6.4MeV Fe^{3+} ions up to 0.1 and 2 dpa at 573 K. The obtained main results are as follows:

- 1) NI hardness profiles of W single crystal significantly differ between the two orientations with a higher hardening tendency to deeper indentation depth in irradiated $W\{001\}$ for all irradiation conditions.
- 2) Irradiation hardening evaluated by bulk equivalent hardness is already high in 0.1 dpa condition and only shows a significant orientation dependence in 0.1 dpa condition. Saturation of irradiation hardening seems to occur already at 1 dpa irradiation condition.

- 3) TEM examinations revealed that the ion-irradiation affected zone size is deeper in $W\{001\}$ for all dpa levels and highly pronounced in 2 dpa condition. At the irradiation dose of 2 dpa as well as 1 dpa, a double black band structure with high defect density of ordered networks of dislocation loop rafts, while in 0.1 dpa condition, the defect type depends on crystal orientation.
- 4) It is considered that the 1D motion of very fine interstitial loops are invisible by TEM up to 1 dpa irradiation and becomes large enough to be visible at 2 dpa and responsible for irradiation hardening irrespective of the dpa level.

7.5 References

- 1) E. Hasenhuettl, Z.X. Zhang, K. Yabuuchi, P. Song and A. Kimura: Nucl. Instrum. Methods Phys. Res. B, in press, <http://dx.doi.org/10.1016/j.nimb.2017.02.030>.
- 2) J. Grzonka, L. Ciupinski, J. Smalc-Koziorowska, O.V. Ogorodnikova, M. Mayer and K.J. Kurzydowski: Nucl. Instrum. Methods Phys. Res. B **340** (2014) 27-33.
- 3) "INTERACTION OF IONS WITH MATTER" by J.F. Ziegler. <http://www.srim.org/>, (accessed 2016-09-17).
- 4) R. Kasada, Y. Takayama, K. Yabuuchi and A. Kimura: Fus. Eng. Des. **86** (2011) 2658-2661.
- 5) I. Manika and J. Maniks: J. Phys. D **41** (2008) p. 074010.
- 6) Z. X. Zhang, E. Hasenhuettl, K. Yabuuchi and A. Kimura: Nucl. Mater. En. **9** (2016) 539-546.
- 7) W. D. Nix and H. Gao: J. Mechan. Phys. Solids **46** (1998) 411-425.
- 8) X. Yi, M.L. Jenkins, K. Hattar, P.D. Edmondson and S.G. Roberts: Acta Mater. **92** (2015) 163-177.
- 9) X. Yi, M.L. Jenkins, M.A. Kirk, Z. Zhou and S.G. Roberts: Acta Mater. **112** (2016) 105-120.

Chapter 8:

Summary

Pure tungsten (W) single crystals of {001} and {011} surface orientation have been irradiated with 6.4 MeV Fe³⁺ ions up to 0.1, 1 and 2 dpa at 573 K to investigate the hardening and microstructural evolution in W as a function of crystal orientation and damage level. The thesis consists of the eight chapters.

Chapter 1 introduces the background of this research that includes importance of understanding the bases of radiation damage mechanisms in pure W that will be applied to plasma facing component in fusion reactor, and how this research shall contribute to the solutions about unclear ion-irradiation hardening behaviour of pure W.

Chapter 2 summarizes the current research status of crystal orientation dependent ion-irradiation effects in W, including threshold energy, surface morphology changes, type of ion-irradiation defects, ion-irradiation affected zone size and hardening behaviour. It can be concluded that the research in crystal orientation dependent ion-irradiation effects is very limited. On the other hand, the mechanical properties of the unirradiated W seem quite well studied. The research status of crystal orientation dependent mechanical properties in the unirradiated W are also summarized for nanoindentation (NI) hardness, microindentation hardness and tensile stress-strain behaviour. As shown in this chapter, the important questions about crystal orientation dependence of ion-irradiation hardening and ion-irradiation affected zone size are still unresolved. And finally the objective of this thesis, which is to investigate the potential effect of crystal orientation on hardening and microstructure evolution in ion-irradiated W without the consideration of grain boundary effects, is addressed.

Chapter 3 describes the experimental methods used in this research with a focus on the sampling method of W{001} and W{011} single crystal specimen by EBSD method from a starting as-received material of W{001} single crystal and on the ion-irradiation experiments. The specimens were irradiated with 6.4 MeV Fe³⁺ up to 0.1 dpa, 1 dpa and 2 dpa at 573 K, with DuET at Kyoto University. NI hardness tests were carried out to evaluate ion-irradiation hardening.

Chapter 4 discusses about the strain rate sensitivity of NI hardness. Strain rate jump tests were carried out to evaluate strain rate sensitivity of unirradiated and ion-irradiated W{001} of 0.1, 1 and 2 dpa irradiation condition. It was found that for the given irradiation and nanoindentation testing conditions, ion-irradiation increased NI hardness and slightly decreased strain rate sensitivity of the hardness and the activation volume for deformation process. The bulk equivalent strain rate sensitivity was derived and it was concluded that there was a good agreement with the only available data source for tensile tested strain rate sensitivity of neutron irradiated pure W.

Chapter 5 discusses about material pile-up that arise around indents and are usually not taken into account in the NI hardness estimation. So called Elastic Modulus Correction (EMC) method was used for NI hardness measurement. It was found that the bulk equivalent hardness values obtained by this method were about 70% of uncorrected NI results for irradiated W{001} and about 85% for unirradiated W{001}, which shows that the formation of pile-up indeed has a considerable effect on the NI hardness in pure W. The amount of ion-irradiation hardening estimated by the EMC method was approximately 40 %, 50 % and 60 % of without consideration of EMC effect for the samples irradiated up to 0.1 dpa, 1 dpa and 2 dpa, respectively. Interestingly, the EMC method results of ion-irradiation hardening had a better match with irradiation hardening of neutron irradiated pure W obtained by micro-Vickers hardness tester.

Chapter 6 discusses the crystal orientation dependent microstructural and hardness changes in W single crystal. The microstructural and hardness changes by 1 dpa ion-irradiation at 573 K were compared between W{001} and W{011} single crystals. It was recognized that ion-irradiation hardening depth profile showed a clear orientation dependence with a higher and deeper hardening in 1 dpa W{001}. Noticeable is that this was not observable by TEM microstructural examinations, where the ion-irradiation affected zone size was only slightly deeper in 1 dpa W{001} and both orientations showed a double black band with high defect density consisting of mainly dislocation loop rafts.

Chapter 7 focuses on the mechanism of orientation dependence of ion-irradiation hardening of pure W, where several damage levels in both orientations were compared in hardening behaviour and microstructural evolution to discuss the orientation dependence of irradiation effects more systematically. The ion-irradiation affected zone size of pure W single crystals of {001} and {011} surface orientations were evaluated as a function of damage level (0.1, 1 and 2 dpa) and crystal orientation. At the irradiation dose of 2 dpa as well as 1 dpa, a double black band structure was observed. The main defects are ordered networks of dislocation loop rafts. The width and depth of the high defect density bands were orientation and damage level dependent. The NI hardness profiles of all the samples conditions showed that ion-irradiation hardening depended more on crystal orientation than on damage level. The ion-irradiation hardening depth profile in all the damage level of W{001} was deeper than W{011}. A double black band structure can be interpreted on the bases of SRIM code calculation results indicating two different depth profiles of lattice damage structures and implanted Fe³⁺ ions. The shallower black bands may consist of lattice damage structures such as self-interstitial loops and/or vacancy clusters, while the deeper one may consists of Fe interstitial loops.

As for the orientation dependence of the NI hardness profile, a possible interpretation of the crystal orientation dependence can be addressed to the 1D motion of very fine interstitial loops are invisible by TEM up to 1 dpa irradiation and becomes large enough to be visible at 2 dpa and responsible for irradiation hardening irrespective of the dpa level, where the longer distance of the 1D motion of interstitial loops in W{001} than in W{011} is considered to be due to the difference in the geometrical orientation of the direction of the 1D motion along the direction parallel to the Burger's vector, b , of the loops.

Chapter 8 is a summary of thesis.

Publications:

1. Eva Hasenhuettl, Ryuta Kasada, Zhexian Zhang, Kiyohiro Yabuuchi, Akihiko Kimura
Ion-irradiation effect on strain rate sensitivity of nanoindentation hardness of tungsten single crystal
Materials Transactions, regular full length article, in press, DOI: 10.2320/matertrans.ML201603.
2. Eva Hasenhuettl, Zhexian Zhang, Kiyohiro Yabuuchi, Peng Song, Akihiko Kimura
Crystal orientation dependence of ion-irradiation hardening in pure tungsten
Nuclear Instruments and Methods in Physics Research-B, regular full length article, in press, DOI: 10.1016/j.nimb.2017.02.030.
3. Eva Hasenhuettl, Ryuta Kasada, Zhexian Zhang, Kiyohiro Yabuuchi, Yen-Jui Huang, Akihiko Kimura
Evaluation of ion-irradiation hardening of tungsten single crystals by nanoindentation technique considering material pile-up effect
Materials Transactions, regular full length article, accepted.
4. Eva Hasenhuettl, Zhexian Zhang, Kiyohiro Yabuuchi, Akihiko Kimura
Effect of displacement damage level on the ion-irradiation affected zone evolution in W single crystals
Journal of Nuclear Materials, regular full length article, submitted on 2017.03.06.
5. Zhexian Zhang, Eva Hasenhuettl, Kiyohiro Yabuuchi, Akihiko Kimura
Evaluation of helium effect on ion-irradiation hardening in pure tungsten by nano-indentation method
Nuclear Materials and Energy, Volume 9 (2016) 539–546.

Acknowledgements

This work is dedicated to my biggest supporters, my mother Ms Sigrid Hasenhuettel, my grandfather Mr Stefan Plank and my grandmother Ms Rosa Plank.

I want to express my gratitude to my brother Dr. Peter Hasenhuettel for encouraging me all my life.

I thank my life partner Mr Alessandro Merola for his love and support ever since we met.

I thank my closest friends in Austria, Dr. Clemens Krautgasser and Ms Barbara Kern, and in Japan, Dr. Desislava Skerleva, Ms Yumi Matsumoto, Mr Daniel Morrall and Dr. Kyohei Yoshida, for their close friendship during my stay in Japan.

I thank my academic supervisor Prof. Dr. Akihiko Kimura for his endless support for my research project and his patience in the last 3.5 years.

I thank Associate Prof. Dr. Kiyohiro Yabuuchi, Associate Prof. Dr. Ryuta Kasada and Associate Prof. Dr. Sosuke Kondo for their scientific support in my study.

I thank my senpai Dr. Zhexian Zhang for always taking time when there were experimental challenges to solve and for giving me all the helpful scientific input in tungsten and ion-irradiation research.

I thank Ms Yuko Wada for always helping me with administrative works regarding research and daily life concerns.

I thank the current lab members for their kindness and efficient working together in a group.

I gratefully acknowledge the financial support between 1.10.2014 and 30.09.2016 by the Ministry of Education, Sports, Culture, Science and Technology, MEXT, scholarship of the Japanese Government.